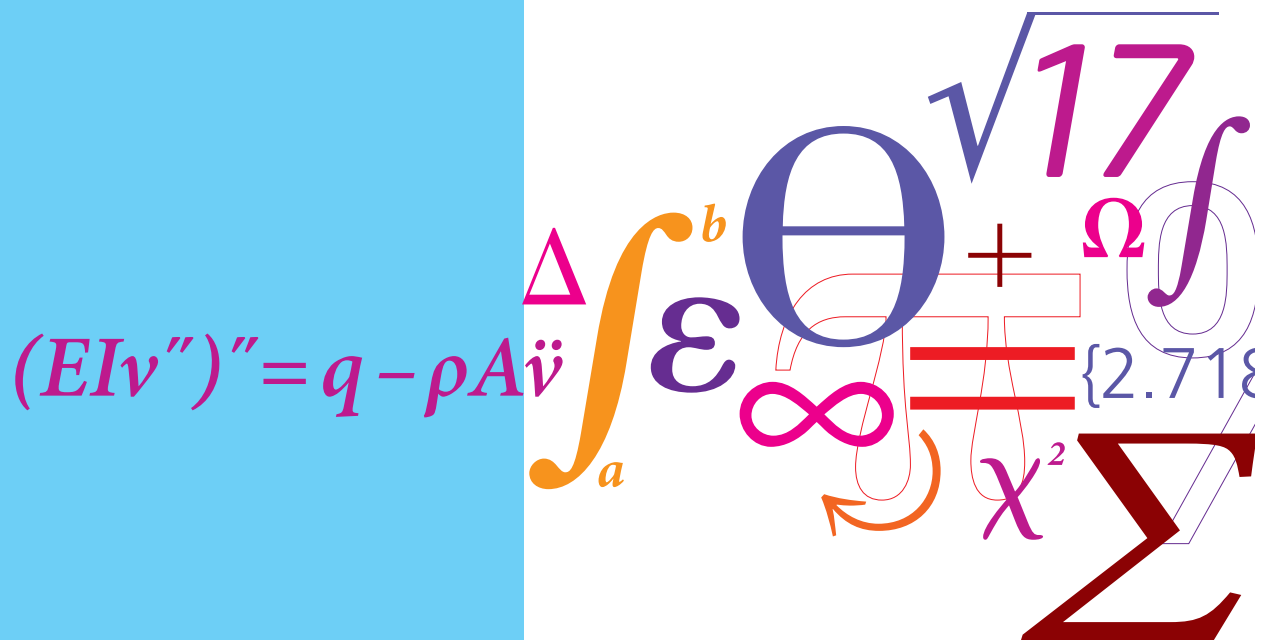


# Damping of wind turbine tower vibrations

PhD Thesis



Mark Laier Brodersen  
 DCAMM Special Report No. S203  
 December 2015



# Damping of wind turbine tower vibrations

Mark Laier Brodersen

TECHNICAL UNIVERSITY OF DENMARK  
DEPARTMENT OF MECHANICAL ENGINEERING  
SECTION OF SOLID MECHANICS  
DECEMBER 2015

*Published in Denmark by  
Technical University of Denmark*

*Copyright © M.L. Brodersen 2015  
All rights reserved*

*Section of Solid Mechanics  
Department of Mechanical Engineering  
Technical University of Denmark  
Nils Koppels Alle, Building 404, DK-2800 Kongens Lyngby,  
Denmark  
Phone +45 4525 1960, Telefax +45 4593 1475  
E-mail: [info@mek.dtu.dk](mailto:info@mek.dtu.dk)  
WWW: <http://www.mek.dtu.dk/>*

*Publication Reference Data*

*M.L. Brodersen*

*Damping of wind turbine tower vibrations*

*Phd Thesis*

*Technical University of Denmark, Section of Solid Mechanics.*

*December, 2015*

*ISBN 978-87-7475-442-8*

*DCAMM Special Report No. S196*

*Keywords: Tower vibrations, offshore wind turbines,  
monopile, vibration control, damping, struc-  
tural dynamics, stroke amplifying brace, viscous  
hybrid damper, active tuned mass damper, real  
time hybrid simulation*

## PREFACE

This thesis is submitted in partial fulfillment of the Danish Ph.D. degree from the Technical University of Denmark. The work has primarily been performed at the Department of Mechanical Engineering at the Technical University of Denmark, in the period March 2012 to December 2015 under the supervision of Associate Professor Jan Høgsberg. The PhD study was financed by the Danish Energy Agency and Vestas Wind Systems A/S under the EUDP project 'Monopile cost reduction and demonstration by joint applied research'. The financial support is gratefully acknowledged.

I would like to express my deepest gratitude to my supervisor Jan Høgsberg for his guidance and support throughout the project.

Part of the work has been carried out at the Intelligent Infrastructure Systems Lab (IISL) at Purdue University. I am grateful to the head of IISL Prof. Shirley Dyke for making the stay possible and for her supervision. I would also like to thank Ph.D. student Gaby Ou for the rewarding collaboration during my stay at the IISL.

Furthermore, I would like to thank my colleagues at the department for fruitful discussions and a pleasant working environment. Thanks also to Jesper Toft Falkenberg for proof reading.

Finally, I would like to thank my wife Lena for her patience and support.

Kongens Lyngby, December 2015

Mark Laier Brodersen

## RESUMÉ

Dæmpning af tårnsvinginger spiller en vigtig rolle for den fremtidige anvendelse af monopælsfundamenter til havvindmøller. Denne afhandling indeholder et sammendrag bestående af fire dele og de vedlagte artikler [P1-P4] vedrørende nye metoder til at dæmpe tårnsvinginger.

Den første del af afhandlingen præsenterer det teoretiske fundament for implementering af dæmpere i vindmøller. Det demonstreres hvorledes dæmpere kan installeres i bunden af tårnet ved hjælp af en amplitude forstærkende mekanisme, hvorved flytningen over dæmperen forstørres og den tilsvarende ønskede dæmperkraft reduceres. Derved forøges potentialet for at installere dæmpere i bunden af tårnet. En kuglelede mekanisme som kan forstørre tårnets bøjningsdeformation forbundet med de to laveste modale sviningsformer præsenteres. Ydermere vises det ved hjælp af numeriske simuleringer hvorledes minimum tre dæmpere er nødvendig i forhold til at indføre lige meget dæmpning til begge de to laveste modale sviningsformer uafhængigt af vindmøllens orientering.

I del to præsenteres et nyt hybrid koncept med en viskos dæmper. Konceptet består af en viskos dæmperenhed i serie med en aktuator og en lastcelle. Aktuatorflytningen reguleres via en tilbagekobling af den integreret dæmper kraft målt af lastcellen. Ved at regulere aktuatorflytningen så den er præcis 180 grader ude af fase med dæmperkraften, kan flytningen over den viskose dæmper enhed forstørres. Ved istedet at indføre et passende filter i tilbagekoblingen af den integreret dæmper kraft kan dæmperen reguleres således at den opnåelige dæmpning forøges.

I tredje del af afhandlingen beskrives et aktiv masse dæmper koncept. Ved at regulere kontrolsignalet til aktuatoren med tilbagekobling fra tårnets flytning og den relative hastighed mellem dæmper massen og tårnet kan den aktive masse dæmper tunes til at indføre effektiv dæmpning af de to laveste modale svingningsformer. For en harmonisk variende belastning opnåes samme reduktion i vindmøllens sviningsamplitude for den aktive masse dæmper som for den passive masse dæmper, men for en kraftigt reduceret dæmper masse. Ydermere demonstreres det hvorledes aktuatorens kontrolkraft kan reduceres.

Slutteligt, præsenteres resultaterne fra en række real-time hybrid simuleringer med hybrid dæmperen. Resultaterne illustrerer hybrid dæmperens evne til at forstørre dæmper flytningen eller den opnåelige dæmpning. Resultaterne viser dog også at lavfrekvent støj i det målte dæmperkraft signal har en tendens til at få aktuatorflytningen til at 'drive' væk fra dets udgangsposition. Når hybrid dæmperen reguleres for at opnå en øget dæmper flytning kan der introduceres en filteret integration, der både reducerer aktuatorens tendens til at 'drive' og samtidig bibeholder den tilførte dæmpning. Når dæmperen istedet reguleres for at opnå øget dæmpning kan der også indføres en filteret integration, hvorved aktuatorens tendens til at 'drive' reduceres, dog reduceres også den tilførte dæmpning.

## ABSTRACT

Damping of wind turbine vibrations by supplemental dampers is a key ingredient for the continuous use of monopiles as support for offshore wind turbines. The present thesis consists of an extended summary with four parts and appended papers [P1-P4] concerning novel strategies for damping of tower dominated vibrations.

The first part of the thesis presents the theoretical framework for implementation of supplemental dampers in wind turbines. It is demonstrated that the feasibility of installing dampers at the bottom of the tower is significantly increased when placing passive or semiactive dampers in a stroke amplifying brace, which amplifies the displacement across the damper and thus reduces the desired level of damper force. For optimal damping of the two lowest tower modes, a novel toggle-brace concept for amplifying the bending deformation of the tower is presented. Numerical examples illustrate that a minimum of three braces in a symmetric circumferential configuration are needed to introduce homogeneous damping in the two lowest vibration modes, independent of the rotor direction.

A novel hybrid viscous damper concept is described in the second part. The hybrid damper consists of a viscous dash-pot in series with an actuator and a load cell. The controllable actuator displacement is regulated by an Integral Force Feedback (IFF) with the measured force from the load cell as sensor input. By controlling the actuator displacement exactly  $180^\circ$  out of phase with the damper force, the displacement across the passive viscous dash-pot is increased, thus improving the feasibility of placing dampers at the root of the wind turbine tower. Furthermore, attainable damping can be increased when introducing a filtered version of the proposed IFF control, and explicit design concepts are presented in the thesis.

An Active Tuned Mass Damper (ATMD) concept is described in the third part of the thesis. By controlling the supplemental actuator force with absolute tower displacement and relative damper velocity as sensor input a stable control scheme is constructed for effective damping by the ATMD of the two critical tower modes. The frequency response performance of the ATMD is equivalent to that of the passive Tuned Mass Damper, but with a reduced damper mass. Furthermore, it is demonstrated that the active control force can be significantly reduced.

Finally, in the last part the performance of the hybrid viscous damper with IFF is validated by a series of real time hybrid simulations (RTHS). The experimental results illustrate the ability of the hybrid damper concept to increase damper stroke or attainable damping. The results also show that the actuator signal is quite sensitive to drift due an offset in the measured damper force. Thus, for the stroke amplifying IFF control a filtered integration is introduced, which almost retains the desired amplification and reduces drift. For the filtered IFF control, aimed at enhancing attainable damping, an augmented filtering similarly reduces drift, but also deteriorates the damping performance.

## PUBLICATIONS

### *Appended papers*

- [P1] Mark L. Brodersen, Jan Høgsberg, Damping of offshore wind turbine tower vibrations by a stroke amplifying brace, *Energy Procedia*, **53**:258–267, 2014.
- [P2] Mark L. Brodersen, Jan Høgsberg, Hybrid damper with stroke amplification for damping of offshore wind turbines, *Wind Energy* (submitted).
- [P3] Mark L. Brodersen, Ann-Sofie Bjørke, Jan Høgsberg, Active Tuned Mass Damper for damping of offshore wind turbine vibrations, *Wind Energy* (submitted).
- [P4] Mark L. Brodersen, Ge Ou, Jan Høgsberg, Shirley J. Dyke, Analysis of hybrid viscous damper by real time hybrid simulations, *Engineering Structures* (submitted).

*Additional contributions*

- [A1] Mark L. Brodersen, Design of stroke amplifying brace concepts for damping of wind turbine tower vibrations, Proceedings of 9th PhD Seminar on Wind Energy in Europe, September 18-20, 2013, Visby, Sweden.
- [A2] Mark L. Brodersen, Jan Høgsberg, Design of stroke amplifying brace concepts for damping of wind turbine tower vibrations, Proceedings of 26th Nordic Seminar on Computational Mechanics, October 23-25, 2013, Oslo, Norway.
- [A3] Jan Høgsberg, Mark L. Brodersen, Hybrid viscous damper with filtered integral force feedback control, *Journal of Vibration and Control* (published online).
- [A4] Jan Høgsberg, Mark L. Brodersen, Steen Krenk, Resonant passive-active vibration absorber with double integrated force feedback control, *Smart Materials and Structures* (submitted).



## CONTENTS

<b>1</b>	<b>Introduction</b>	<b>1</b>
1.1	Monopile supported offshore wind turbines . . . . .	1
1.2	Damping of offshore wind turbines . . . . .	3
1.3	Novel concepts for damping of tower vibrations . . . . .	5
1.4	Outline of thesis . . . . .	6
<b>2</b>	<b>Implementation of supplemental dampers</b>	<b>7</b>
2.1	Equation of motion for wind turbine . . . . .	7
2.2	Stroke amplifying brace concept . . . . .	8
2.3	Optimum tuning . . . . .	11
<b>3</b>	<b>Hybrid viscous damper</b>	<b>15</b>
3.1	Damper concept . . . . .	15
3.2	Filtered Integral Force Feedback . . . . .	16
3.3	Numerical analysis of shear frame . . . . .	18
3.4	Increasing damper stroke . . . . .	20
3.5	Time dependent simulations in HAWC2 . . . . .	21
<b>4</b>	<b>Active Tuned Mass Damper</b>	<b>25</b>
4.1	Equation of motion for ATMD . . . . .	26
4.2	Optimum modal tuning . . . . .	27
4.3	Frequency response analysis in HAWC2 . . . . .	30
<b>5</b>	<b>Real Time Hybrid Simulations</b>	<b>32</b>
5.1	Experimental setup . . . . .	32
5.2	RTHS with shear frame and filtered IFF controller . . . . .	36
5.3	RTHS with offshore wind turbine and IFF controller . . . . .	39
<b>6</b>	<b>Conclusion</b>	<b>43</b>
	<b>Bibliography</b>	<b>44</b>



## 1. INTRODUCTION

Present day design of monopile support structures for offshore wind turbines is driven by the fatigue limit state, due to tower vibrations excited by wind and waves. The forecast for offshore wind is that larger wind turbines will be positioned at even deeper waters than today, and it is expected that this trend will cause the global tower dominated vibrations to become an even more critical issue in the design of monopile supported offshore wind turbines.

### 1.1. Monopile supported offshore wind turbines

Today, monopiles are by far the most commonly used support structure for offshore wind turbines, with a growing share of approximately 80 % of the market at the end of 2014 [15]. Compared to other types of support structures, such as the tripile or suction bucket foundations, the monopile is considered a well developed and proven technology, which is an important asset as companies try to reduce the financing costs associated with offshore wind farms. The main reason for the popularity of the monopile support is however mainly due to its simplicity in terms of fabrication and installation [13]. The installation of a monopile is usually performed by a floating crane, as seen in Fig. 1.1(a), and a large hammer is normally used for driving the monopile into the seabed. Next a transition piece is grouted to the monopile, and the wind turbine tower is subsequently installed on top of the transition piece. However, in very recent installations of monopiles, as seen in Fig. 1.1(b), the transition piece has simply been omitted and the tower is instead bolted directly to the monopile. Offshore wind farms, as depicted in Fig. 1.1(c), are often considered the preferred

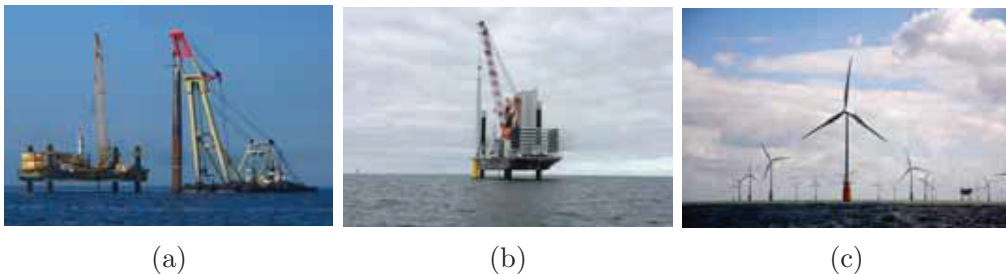


FIGURE 1.1. (a) Monopile (Schiffahrtsinstitut Warnemünde e.V.), (b) tower during installation (vanoord.com) and (c) offshore wind farm with monopile foundations (lorc.dk).

choice over land-based onshore wind turbines, due to the better wind conditions at sea, and because of its smaller local environmental impact on both humans and wildlife. However, the reliable and steady wind at sea comes at a price. For an offshore wind turbine the average price for the support structure constitutes approximately 24 % of the total cost, while it is only 7 % for onshore wind turbines [24]. In order to reduce the percentage of cost associated with the support structure, offshore wind turbines are upscaled to even larger rotor diameters and location at sites with deeper waters and improved wind conditions. This upscaling implies that the monopile support structure must also increase in size, as illustrated in Fig. 1.2 (courtesy of A2SEA A/S).

The dominant tower vibrations of the offshore wind turbines are caused by wind and waves, exciting primarily a combination of the two lowest tower modes: The fore-aft mode, in the direction of the rotor, and the side-side mode, in the direction lateral to the rotor. Especially waves acting on the monopile with a relative angle to the mean wind direction cause relatively large fatigue damage due to the absence of aeroelastic damping in the (side-side) direction lateral to the mean wind [10, 45]. The fore-aft tower mode and the lightly damped side-side mode are illustrated in Fig. 1.3. In the absence of aerodynamic damping, the damping ratio of these two

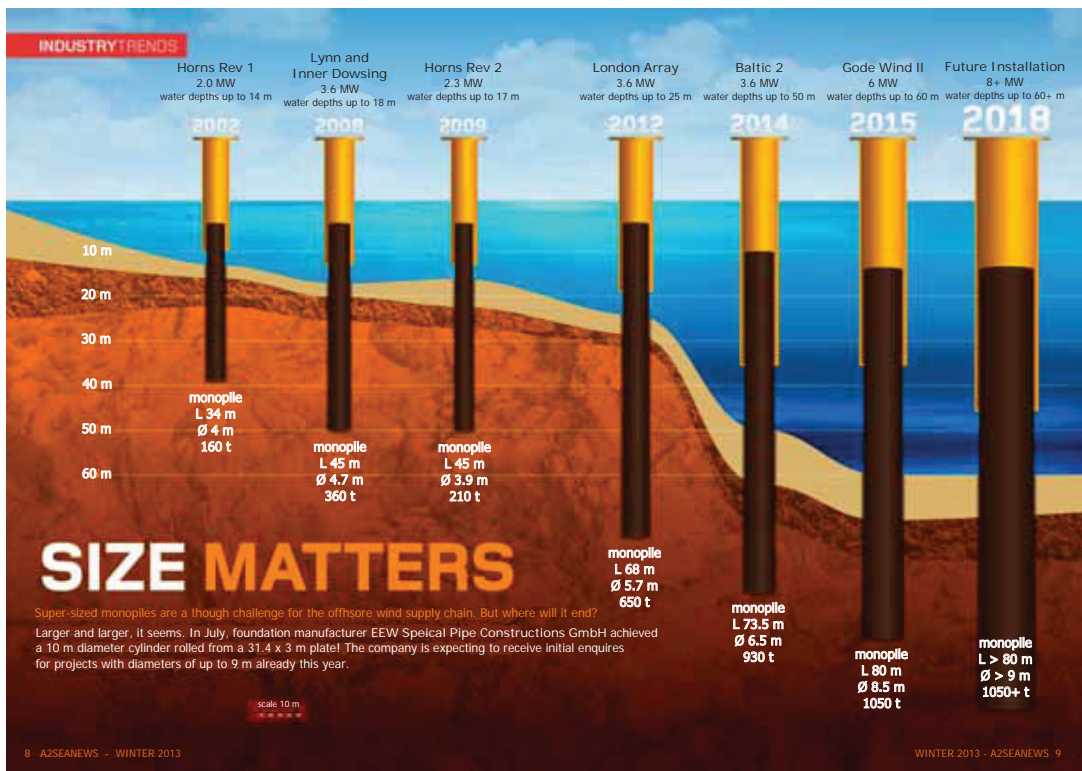


FIGURE 1.2. Development in size of monopile support structures (courtesy of A2SEA A/S).

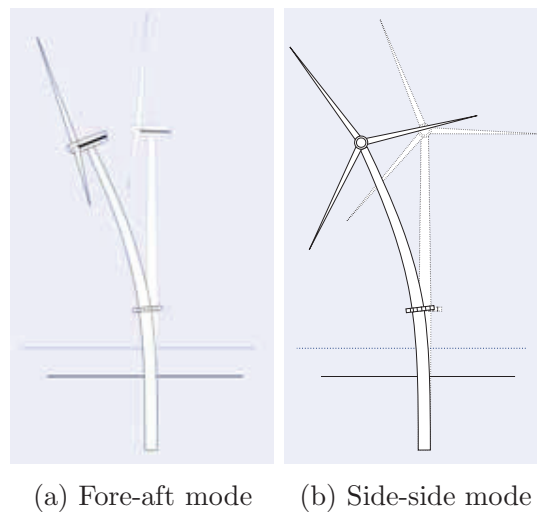


FIGURE 1.3. Two lowest tower modes of a fixed offshore wind turbine: (a) Fore-aft and (b) side-side.

critical tower modes is usually found to be rather small, on the order of 1 % of critical damping [10, 12, 38]. A major drawback of the monopile support, compared to e.g. a lattice type jacket structure, is its sensitivity with respect to wave loading. As larger offshore wind turbines are positioned at deeper waters, the structure will become more slender and the structural frequency of the critical tower modes will decrease and move closer to the primary excitation frequency of the waves, whereby fatigue damage due to wave loading is expected to increase significantly, due to the low inherent damping. Furthermore, as wind turbines become larger, the diameter of the monopile support structure is expected to increase correspondingly, which consequently will further increase wave loading. Thus, in a near future this increased resonant wave loading may render the monopile support unfeasible, compared to other types of support structures.

## 1.2. Damping of offshore wind turbines

A way to reduce the response from resonant wave loading and increase the feasibility of the monopile support structure would be to install supplemental dampers to increase the damping ratio of the two critical tower modes. Use of supplemental dampers is widely recognised as an effective way of reducing the excessive dynamic response of lightly damped flexible structures, and a large variety of dampers are available and used in practice. Comprehensive reviews on the use of dampers for structural control can be found in the papers by Housner et al. [20] and by Soong & Spencer [41]. In the available literature concerning the structural control of wind turbine tower vibrations by supplemental dampers, most of the publications focus on the application of different types of Dynamic Vibration Absorbers (DVAs), such

as the Tuned Mass Damper (TMD) or the Tuned Liquid Column Damper (TLCD). Enevoldsen [14] was one of the first scientists to investigate the performance of a TMD on an onshore wind turbine, demonstrating that the introduction of a TMD in fact changes the failure mode from a fatigue limit state to an extreme limit state, indicating that a TMD primarily is effective with respect to the stationary harmonic or narrow-banded loading, that mainly causes fatigue damage in wind turbines. Later Collins et al. [7] investigated the application of multiple TMDs as well as the application of semi-active and active TMDs for the reduction of tower vibrations due to wind loading. Both passive and active TMDs were found to give a significant reduction in the response amplitudes of the wind turbine tower, although the passive TMDs were found to be quite sensitive to uncertainties in the structural frequency of the wind turbine. Along with the development of the first offshore wind farms a number of papers has focused on the application of DVA concepts for damping of the tower vibrations of fixed offshore wind turbines. In the study by Colwell and Basu [8] the application of a TLCD for damping of the along-wind vibrations of a fixed offshore wind turbine was investigated by assuming correlated wind and wave loads. In a related study Murtagh et al. [29] investigated the damping of along-wind vibrations with a TMD installed instead of a TLCD. In both papers by Basu and co-workers [8, 29] the influence of including the rotations of the blades was investigated, and found to be negligible for the performance of the damper. More recently, attention has focused on how to address the absence of aerodynamic damping in the side-side direction, when significant wind-wave misalignment occurs. This includes the work by Stewart and Lackner [44], who numerically demonstrated the beneficial effect of a TMD in reducing the tower base moment, and in particular the side-to-side moment. Finally, in a recent paper by Rodriguez et al. [36] a novel strategy of installing dampers at the bottom of the wind turbine tower by means of a stroke amplifying brace was introduced. The brace design was however based on the tower deforming primarily in shear and therefore not optimised towards the critical tower modes of a wind turbine, in which the tower deforms primarily because of bending. Information in the literature regarding the present status for implementation of tower dampers in offshore wind turbines is limited. However, to the authors knowledge, most offshore wind turbines are today installed with a type of passive DVA in the tower, where in particular two concepts are favored: A pendulum submerged in sufficiently viscous fluid and a type of liquid damper, as also stated in the paper by Tarp-Johansen et al. [45]. Both concepts have the advantage that they are independent of the yaw rotation of the nacelle, and they are furthermore robust and easy to install and maintain.

A passive DVA is a well known concept within damping and control of flexible structures, where it has been used mainly in high-rise buildings for reduction of excessive vibrations during earthquakes or due to wind loading [40, 46]. A DVA is very effective when primarily one mode or a few closely positioned modes are excited, where it is capable of delivering significantly better damping performance

compared to a non-resonant damper concept. Though, in order for a DVA to be effective, it needs to be installed, where the amplitude of the critical tower mode is largest, which for the wind turbine is at the top of the tower or in the nacelle. Effective damping by a DVA is furthermore associated with large damper mass, which constitutes a major limitation, since additional mass is highly undesirable at the top of the wind turbine. As the wind turbines of the future will be more slender with larger vibrational mass, the auxiliary mass of the attached DVA must also become larger. Another practical concern is the limited space at the top of the tower. For a pendulum damper for example, the eigenfrequency is determined solely by the length of the pendulum arm. As the frequency needs to be lowered the arm should be longer, which might constitute a problem with respect to the limited space inside the tower and thus its use in offshore wind turbines.

### 1.3. Novel concepts for damping of tower vibrations

The objective of the present thesis is to investigate alternatives to the passive DVA for damping of tower vibrations in fixed offshore wind turbines with the explicit goal to increase the damping and thus indirectly to extend the feasibility of the monopile support to deeper waters and larger wind turbines. Both passive and hybrid (active) methods are considered with the aim to develop damper solutions that can provide sufficient damping to the critical tower modes without adding significant mass at the top of the wind turbine. The approach is based on a retrofit design, whereby the damper solutions are expected to fit within the current design-standard for fixed offshore wind turbines. The thesis consists of an extended summary covering the main aspects of the theory, numerical as well as experimental results, followed by four journal papers denoted [P1] to [P4], which cover the presented material in greater detail.

In the paper [P1] a novel stroke amplifying brace for installation of passive and semi-active dampers at the bottom of a wind turbine tower is presented. Dampers installed to act on the relative displacement need to be installed where the deformation of the tower is largest, which for the two lowest tower modes is at the bottom of the tower. The deformation at the bottom of the tower is however limited, and in order to make it feasible to install passive or semi active dampers, the deformation of the tower should be amplified to a large displacement over the damper. The simple stroke amplifying brace introduced in [P1] is designed to amplify the bending deformation at the bottom of a wind turbine tower, through the use of a toggle mechanism, whereby installation of dampers could be realised without active means.

The paper [P2] seeks to install supplemental dampers at the bottom of the tower by means of a novel viscous hybrid damper. The hybrid damper, consisting of a viscous dash-pot in series with an actuator and a load cell, is combined with an integral force feedback (IFF) controller for regulating the actuator displacement in

the hybrid damper. By operating the actuator velocity with a phase angle of  $\pi$  relative to the measured damper force, the displacement over the viscous dash-pot can be increased compared to the passive case, without deteriorating the damper performance of the viscous dash-pot. This active control strategy could therefore increase the feasibility of installing dampers at the bottom of the tower. If instead the actuator displacement is regulated using a filtered IFF controller, attainable damping can be increased compared to the pure viscous case.

An Active Tuned Mass Damper (ATMD) is a Tuned Mass Damper (TMD) where the spring and damper is supplemented by an active actuator. The scope of [P3] is to develop a controller which regulates the applied actuator force, so that the ATMD performance is similar to the passive TMD, but with a reduced size of the auxiliary damper mass. A robust control strategy that involves feedback of the tower displacement and the damper mass velocity is proposed, and a tuning procedure based on the critical (side-side) vibration mode is presented.

Finally, in the paper [P4] the viscous hybrid damper is analysed by the use of real time hybrid simulations (RTHS). The hybrid damper is tested with two different controllers: A filtered IFF controller for enhanced damper performance as introduced in [A3] and an IFF controller for increased damper stroke introduced in [P2]. In the experimental substructure of [P4] a Magnetorheological (MR) damper is regulated by a Bang-Bang controller, emulating the viscous dash-pot in the hybrid damper, while the numerical substructure consists of either a shear frame model or a simplified wind turbine model. The experimental results from the RTHS validate the behavior and performance of the viscous hybrid damper, although the results are sensitive with respect to the accuracy of the force tracking by the Bang-Bang controller.

#### 1.4. Outline of thesis

The extended summary of the present thesis is organised as follows. In chapter 2 the theoretical framework for installing supplemental dampers in the wind turbine used in both [P1] and [P2] is summarised, and the stroke amplifying brace introduced in [P1] is described in detail. Next the viscous hybrid damper concept and the two IFF controllers from [P2] and [P4] are described in chapter 3, while the ATMD and the associated control strategy is presented in the subsequent chapter 4. Finally, in chapter 5 the experimental results from the RTHS in [P4] are summarised, while concluding remarks are provided in chapter 6.

## 2. EFFECTIVE IMPLEMENTATION OF SUPPLEMENTAL PASSIVE DAMPERS IN A WIND TURBINE TOWER

Effective control of wind turbine tower vibrations by supplemental dampers requires a placement of the dampers that provides sufficient observability and controllability. A passive damper is by definition collocated, whereby the two terms of observability and controllability are equivalent and in the following represented by the single term: *Modal connectivity*. In the two critical tower vibration modes the wind turbine tower is deformed primarily due to bending, whereby the largest deformation associated with curvature occurs at the bottom of the tower, while the largest absolute displacement is observed at the top of the tower, see Fig. 1.3. For a Dynamic Vibration Absorber (DVA) with an auxiliary mass the largest modal connectivity is associated with a placement at the tower top, where the absolute displacement amplitude attains its maximum. In the case of dampers installed to act on the relative displacement between two points of attachment on the wind turbine, the maximum modal connectivity is obtained at the bottom of the tower, where the curvature due to bending is largest. Unfortunately, the stroke across dampers installed at the bottom of the tower is often very small, which limits the feasibility of installing dampers to act on the relative displacement of the tower.

In the paper [P1] it is demonstrated how the feasibility of installing passive viscous dampers at the bottom of the tower can be increased significantly, compared to the case where the dampers are attached directly to the tower wall, by installation in a so-called stroke amplifying brace. As demonstrated in [P1] an increase in damper stroke implies a reduction in the optimal damper force, whereby the feasibility is even further improved because smaller dampers are needed. In the following the design of supplemental dampers is presented with particular emphasis on the installation in a stroke amplifying brace placed at the bottom of the wind turbine tower.

### 2.1. Equation of motion for wind turbine

The two lowest critical tower modes of an offshore wind turbine are to a large extent independent of the rotation of the blades [17]. Assuming a linear spring model for the interaction between monopile and the soil in the seabed, the dynamics associated with the two basic tower modes can be relatively well represented by a simple linear

beam model. A further simplification can be made by lumping the mass and inertia of the nacelle at the top of the tower. The discretised equations of motion for the structural degrees of freedom (dof) in  $\mathbf{u}$  of the wind turbine at standstill are then represented as

$$\mathbf{M}\ddot{\mathbf{u}} + \mathbf{C}\dot{\mathbf{u}} + \mathbf{K}\mathbf{u} = \mathbf{f} + \mathbf{f}_e, \quad (2.1)$$

where the dot denotes the time derivative.  $\mathbf{M}$  is the mass matrix,  $\mathbf{K}$  is the stiffness matrix,  $\mathbf{C}$  represents structural damping,  $\mathbf{f}$  is the nodal load vector from the supplemental dampers and  $\mathbf{f}_e$  is the generalised force vector associated with the external loading due to wind and waves. The stiffness matrix consists of two parts: The constitutive elastic stiffness matrix  $\mathbf{K}_c$  representing the structure and the stiffness matrix  $\mathbf{K}_s$  from the elastic foundation representing the interaction with the soil.

To compare different installations of supplemental dampers, a model of a 5 MW reference offshore wind turbine from the Offshore Code Comparison Collaboration (OC3) study [22] is used for the numerical simulations of an offshore wind turbine. The size of the reference turbine is representative of wind turbines being installed in offshore wind farms today, and the results presented in this thesis will thus illustrate the influence of installing the presented damper concepts in current offshore wind turbines. The specific reference turbine is a slightly modified version of a 5 MW reference wind turbine by NREL [23], which is positioned at 20 m water depth measured from seabed to Mean Sea Level (MSL). A summary of the structural properties of the turbine can be seen in Table 2.1.

## 2.2. Stroke amplifying brace concept

Stroke amplifying braces offer the ability to amplify the relative displacement of the structure to a larger displacement across the damper itself, thereby not only increasing the damper stroke but also decreasing the optimal force amplitude exerted by the damper. Different designs based on a toggle-mechanism, including the lower,

TABLE 2.1. Structural properties of the OC3 reference wind turbine [22].

Description	Value
Hub height [m]	90
Tower-top height above MSL [m]	87.6
Tower-base height above MSL [m]	10
Water depth from MSL [m]	20
Penetration depth of monopile [m]	36
Tower mass [ton]	237
Mass of Nacelle+Rotor+Blades [ton]	351
Overall integrated mass [ton]	1216



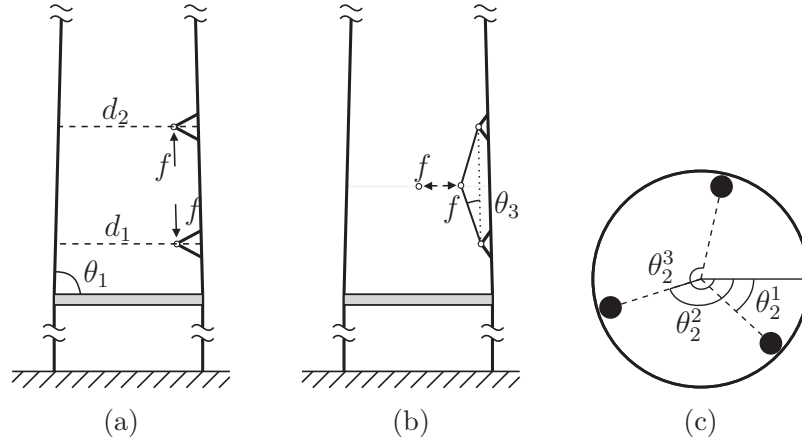


FIGURE 2.2. Illustration of damper force for installation in (a) a curvature brace and (b) a curvature-toggle brace. (c) Illustration of angle  $\theta_2$

the tower centerline. The lowest number of dampers that can provide a symmetric layout is three. However, in a practical implementation a larger number of dampers would most likely be used, as this reduces both the size of each damper and the corresponding force transferred locally to the tower wall from each damper. The three damper brace configuration in Fig. 2.2(c), with  $\Delta\theta_2 = 120^\circ$  between adjacent dampers, is used in the numerical simulations presented later in the thesis.

### 2.2.2. Connectivity vector

The force vector  $\mathbf{f}_k$  representing the  $k$ 'th supplemental damper is conveniently described by the corresponding connectivity vector  $\mathbf{w}_k$  and the local damper force  $f_k$ . The resulting force vector  $\mathbf{f}$  in eq. (2.1) from a set of dampers in a full configuration is then described by the sum over all individual dampers

$$\mathbf{f} = \sum_{k=1}^r \mathbf{w}_k f_k, \quad (2.2)$$

where  $r$  denotes the total number of dampers. Since the damper is collocated the displacement of the  $k$ 'th damper is readily determined as

$$u_k = \mathbf{w}_k^T \mathbf{u}. \quad (2.3)$$

The connectivity vector  $\mathbf{w}_k$  describes the connection of the  $k$ 'th damper to the wind turbine, and it has the same dimension as the number of dofs in the structural model. It contains only zeros except at the dofs of the three adjacent nodes  $n$ ,  $n+1$  and  $n+2$  associated with the attachment of the dampers. Thus, the connectivity vector of the  $k$ 'th damper can be written as

$$\mathbf{w}_k = [0 \quad \dots \quad 0 \quad \mathbf{w}_{k,n}^T \quad \mathbf{w}_{k,n+1}^T \quad \mathbf{w}_{k,n+2}^T \quad 0 \quad \dots \quad 0]^T, \quad (2.4)$$

where the three nodal connectivity vectors  $\mathbf{w}_{k,n}$ ,  $\mathbf{w}_{k,n+1}$  and  $\mathbf{w}_{k,n+2}$  are associated with nodes  $n$ ,  $n + 1$  and  $n + 2$  of the beam model, respectively.

The vectors are conveniently constructed by computing the nodal load vector that consistently imposes the damper forces on the three tower nodes  $n$ ,  $n + 1$  and  $n + 2$ . For the curvature brace in Fig. 2.1(a) the damper imposes no force on the intermediate node  $n + 1$ , whereby  $\mathbf{w}_{k,n+1} = \mathbf{0}$ , while the nodal connectivity vectors for the lower node  $n$  and the upper nodes  $n + 2$  are determined as

$$\mathbf{w}_{k,n} = \begin{bmatrix} \cos(\theta_2^k) \cos(\theta_1) \\ \sin(\theta_2^k) \cos(\theta_1) \\ -\sin(\theta_1) \\ -\frac{1}{2}d_1 \sin(\theta_2^k) \sin(\theta_1) \\ \frac{1}{2}d_1 \cos(\theta_2^k) \sin(\theta_1) \\ 0 \end{bmatrix}, \quad \mathbf{w}_{k,n+2} = \begin{bmatrix} -\cos(\theta_2^k) \cos(\theta_1) \\ -\sin(\theta_2^k) \cos(\theta_1) \\ \sin(\theta_1) \\ \frac{1}{2}d_2 \sin(\theta_2^k) \sin(\theta_1) \\ -\frac{1}{2}d_2 \cos(\theta_2^k) \sin(\theta_1) \\ 0 \end{bmatrix}. \quad (2.5)$$

Thus, the geometry of the bracing system is fully contained in the connectivity vector, whereby  $u_k = \mathbf{w}_k^T \mathbf{u}$  represents the local deformation of the damper inside the brace. For the curvature toggle-brace the expressions are conveniently simplified by assuming  $\cos \theta_3 \simeq 1$ , implying that  $\theta_3 \ll 1$ . The nodal connectivity vectors of the two end nodes  $n$  and  $n + 2$  are

$$\mathbf{w}_{k,n} = \begin{bmatrix} \frac{1}{2} \cos \theta_2^k \left( \frac{\cos \theta_1}{\sin \theta_3} + \sin \theta_1 \right) \\ \frac{1}{2} \sin \theta_2^k \left( \frac{\cos \theta_1}{\sin \theta_3} + \sin \theta_1 \right) \\ -\frac{1}{2} \left( \frac{\sin \theta_1}{\sin \theta_3} - \cos \theta_1 \right) \\ -\frac{1}{4}d_1 \sin \theta_2^k \left( \frac{\sin \theta_1}{\sin \theta_3} - \cos \theta_1 \right) \\ \frac{1}{4}d_1 \cos \theta_2^k \left( \frac{\sin \theta_1}{\sin \theta_3} - \cos \theta_1 \right) \\ 0 \end{bmatrix}, \quad \mathbf{w}_{k,n+2} = \begin{bmatrix} -\frac{1}{2} \cos \theta_2^k \left( \frac{\cos \theta_1}{\sin \theta_3} - \sin \theta_1 \right) \\ -\frac{1}{2} \sin \theta_2^k \left( \frac{\cos \theta_1}{\sin \theta_3} - \sin \theta_1 \right) \\ \frac{1}{2} \left( \frac{\sin \theta_1}{\sin \theta_3} + \cos \theta_1 \right) \\ \frac{1}{4}d_2 \sin \theta_2^k \left( \frac{\sin \theta_1}{\sin \theta_3} + \cos \theta_1 \right) \\ -\frac{1}{4}d_2 \cos \theta_2^k \left( \frac{\sin \theta_1}{\sin \theta_3} + \cos \theta_1 \right) \\ 0 \end{bmatrix}, \quad (2.6)$$

while for the intermediate node  $n + 1$  of the curvature toggle-brace it becomes

$$\mathbf{w}_{k,n+1}^T = \left[ -\cos \theta_2^k \sin \theta_1, -\sin \theta_2^k \sin \theta_1, -\cos \theta_1, 0, 0, 0 \right]. \quad (2.7)$$

### 2.3. Optimum tuning

Optimum tuning of the supplemental dampers follows the work by Main & Krenk [28] concerning tuning of viscous dampers on flexible structures. In the frequency domain the transfer relation of the  $k$ 'te damper between damper force and damper

motion can be expressed as

$$\frac{\bar{f}_k}{\bar{u}_k} = i\omega c H(\omega), \quad (2.8)$$

where the bars denote the modal amplitude and  $\omega$  is the assumed vibration frequency. The parameter  $c$  is a common viscous damping coefficient applied for all dampers in the circumferential configuration, while  $H(\omega)$  represents the desired filtering with  $H = 1$  recovering the pure viscous dash-pot in [P1]. By the introduction of  $H(\omega)$  the damper model could represent the hybrid viscous damper introduced in the following chapter and in [P2,P4]. As demonstrated by Main & Krenk [28] the damped mode associated with implementation of supplemental viscous dampers can be estimated from a two-component representation. The structural motion is therefore expressed as a linear combination of the undamped mode shape  $\mathbf{u}_0$  determined from the undamped eigenvalue problem

$$(\mathbf{K} - \omega_0^2 \mathbf{M}) \mathbf{u}_0 = \mathbf{0}, \quad (2.9)$$

with natural frequency  $\omega_0$ , and the corresponding undamped mode shape vector  $\mathbf{u}_\infty$  associated with fully rigid viscous dampers governed by the modified eigenvalue problem

$$(\mathbf{K} - \omega_\infty^2 \mathbf{M}) \mathbf{u}_\infty = \mathbf{r}, \quad (2.10)$$

with real-valued natural frequency  $\omega_\infty$ . In (2.10) the force vector  $\mathbf{r}$  contains the reaction forces from the rigid dampers on the structure. The two-component format predicts that the complex eigenfrequency associated with the damped mode follows a semi-circular trajectory in the complex plane from the undamped eigenfrequency  $\omega_0$  to the undamped eigenfrequency  $\omega_\infty$ , whereby maximum attainable damping  $\zeta_{max}$  is determined by the change in frequency  $\Delta\omega_\infty = \omega_\infty - \omega_0$  obtained by locking the viscous damper links. An approximate expression for the modal damping ratio can therefore be given as [28]

$$\zeta_{max} = \frac{\Delta\omega_\infty}{\omega_0 + \omega_\infty}. \quad (2.11)$$

Optimum tuning is obtained for the viscous coefficient  $c_{opt}$  which yields maximum attainable damping  $\zeta_{max}$ . Following the procedure outlined in [28] and assuming that the same damping parameter is used for all dampers in the present configuration, the optimum damping parameter for the supplemental dampers is obtained by the relation [19]

$$c_{opt} = \frac{\omega_\infty^2 - \omega_0^2}{\omega \gamma^2} \frac{1}{|H|}, \quad (2.12)$$

where the parameter

$$\gamma^2 = \sum_{k=1}^r (\mathbf{w}_k^T \mathbf{u}_0)^2 \quad (2.13)$$

represents the modal connectivity as the sum of squares of the modal amplitudes across the individual damper connections when the undamped mode shape vector is scaled so that  $\mathbf{u}_0^T \mathbf{M} \mathbf{u}_0 = 1$ . Thus,  $\gamma$  represents the total modal displacement over the dampers installed in the wind turbine, and larger  $\gamma$  leads to a smaller value for  $c_{opt}$ . For the pure viscous damper with  $H = 1$  the optimum damping parameter is effectively estimated as

$$c_{opt} = \frac{\omega_\infty^2 - \omega_0^2}{\omega \gamma^2} \simeq \frac{2 \Delta\omega_\infty}{\gamma^2}, \quad (2.14)$$

where the approximation  $(\omega_\infty^2 - \omega_0^2)/\omega \simeq 2 \Delta\omega_\infty$  has been used to reach the latter explicit approximative expression. Thereby, the optimum viscous damper parameter  $c_{opt}$  is given as a ratio of the change in frequency by locking the dampers divided by the modal participation factor  $\gamma^2$ . In order for implementation of supplemental dampers to be effective, damping should be independent of the orientation of the rotor, implying that  $c_{opt}$  should be the same for the two critical tower modes.

### 2.3.1. Brace installation at the bottom of the tower

Values for  $\gamma$  as function of the first damper position relative to the side-side direction given by  $\theta_2^1$  are shown in Fig. 2.3. The results are for three dampers installed on the tower wall at the bottom of the tower with the upper point attached 4 m above the tower bottom as illustrated in Fig. 2.1. For the curvature toggle brace a value of  $\theta_3 = 5^\circ$  is used. The  $\gamma$  values are scaled by the modal tower top displacement  $u_{0,top}$  and shown in Fig. 2.3(a) for the side-side mode and in Fig. 2.3(b) for the fore-aft vibration mode. The parameter  $\gamma$  is seen to be almost identical for the two tower modes and also independent of the orientation of the rotor. Furthermore, it is found that for the OC3 reference wind turbine the change in frequency by locking the dampers is approximately the same for the two modes and for the two brace designs. Thus, a common value for the viscous coefficient  $c$  is found to be nearly

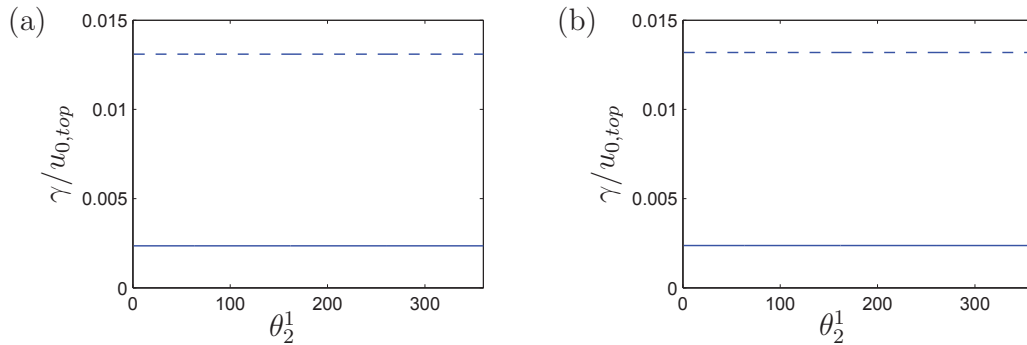


FIGURE 2.3.  $\gamma$  with respect to the (a) side-side and (b) fore-aft mode for dampers in curvature braces (—) and in curvature-toggle braces (---) scaled by the modal tower top displacement  $u_{0,top}$ . Three dampers are installed in a symmetric configuration at the bottom of the tower.

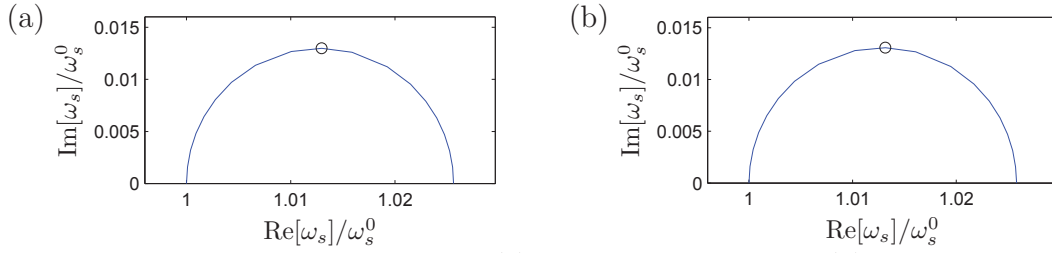


FIGURE 2.4. Root locus with respect to (a) the side-side mode and (b) the fore-aft mode for three toggle braces installed at the bottom of the tower.

optimal for all dampers installed in the same brace in a symmetric configuration in the tower. To demonstrate the attainable damping by installing the three curvature toggle braces at the bottom of the tower a root locus analysis is conducted for increasing viscous coefficient  $c$ . The root loci are shown in Fig. 2.4(a) for the side-side mode and in Fig. 2.4(b) for the fore-aft mode. As expected, attainable damping is seen to be almost identical for the two modes. The black circle represents the complex natural frequencies associated with the viscous coefficient determined by eq. (2.14) with corresponding damping ratio  $\zeta_{ss,max} = 0.0128$  for the side-side mode and  $\zeta_{fa,max} = 0.0129$  for the fore-aft mode.

Figure 2.3 also shows that the difference in  $\gamma$  for dampers installed in curvature braces (—) and curvature-toggle braces (---) is quite significant, which implies that the optimum viscous damping parameter  $c_{opt}$  in eq. (2.14) should be more than two orders of magnitude larger for the curvature brace compared to the curvature toggle-brace (factor of 112) to realise the desired damper force on the structure. Furthermore, the damper force  $f_k$  for a damper installed in a curvature brace will be approximately 10 times larger than the force from a damper installed in a curvature-toggle, which demonstrates how stroke amplifying braces can be used to increase the feasibility of installing dampers at the bottom of a wind turbine tower.

### 3. HYBRID VISCOUS DAMPER

The displacement and attainable damping of passive dampers, as discussed in the previous chapter in terms of the viscous dash-pot, both depend on the position of the damper in the structure [37]. Furthermore, it is difficult to ensure optimal efficiency of passive dampers at any time, since one tuning scenario may not necessarily be optimal for different types of loading conditions [42]. Active control is generally more versatile and may be adjusted adaptively according to system variations. However, it also requires an external power source, which makes it more costly to operate and prone to power loss [20]. More importantly, active systems may furthermore become unstable, whereby the main structure may lose its structural integrity. In between passive and active control, a so-called hybrid damper format is a device where the properties of passive damping and active control may be merged into a favorable combined system, where some of the limitations associated with passive or active control systems may be overcome [43].

The hybrid viscous damper introduced in [A3] is a novel damper concept for active control of large structures, where an active actuator is combined with a passive viscous dash-pot. In the following chapter it is demonstrated how the hybrid damper can be controlled using force feedback either to enhance damping as described in the papers [A3,P4] or to increase damper stroke across the viscous dash-pot, thereby increasing the feasibility of installing dampers at the bottom of a the wind turbine tower, as described in the papers [P2,P4].

#### 3.1. Damper concept

The hybrid viscous damper consists of a dash-pot with viscous coefficient  $c$  in series with an actuator with piston motion  $q$ , and a load cell measuring the damper force  $f$ , as illustrated in Fig. 3.1(a). The displacement of the hybrid damper is denoted by  $u$ , whereby the damper force is given by the time domain equation

$$f = c(\dot{u} - \dot{q}). \quad (3.1)$$

The damper force signal  $f$  is fed back to track the desired actuator velocity  $\dot{q}$  in accordance with a particular control strategy, which determines the overall performance of the hybrid viscous damper.

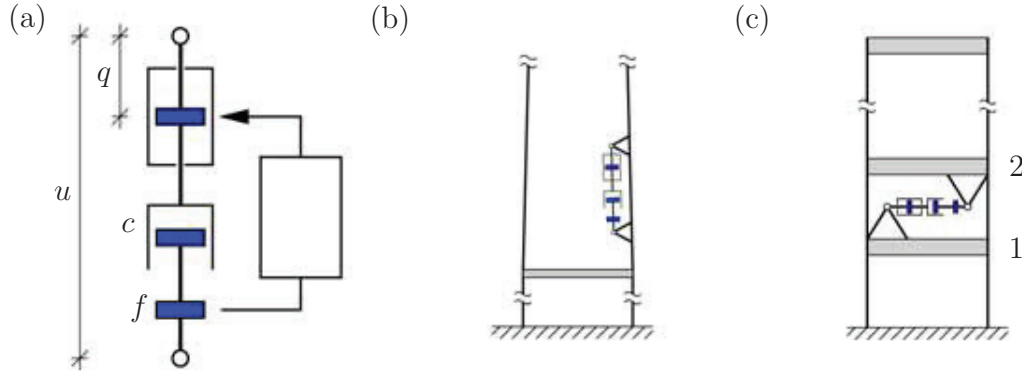


FIGURE 3.1. (a) Hybrid viscous damper and (b) its installation in the lower section of a wind turbine tower or (c) between the first and second floor of a shear frame structure.

### 3.2. Filtered Integral Force Feedback

The actuator displacement  $q$  is controlled according to an Integral Force Feedback (IFF) scheme, inspired by the work by Preumont and co-workers concerning piezoelectric stack actuators [34] and tendon control [33]. In the present format a second order term is added to the classic control equation, resulting in a filtered IFF equation,

$$\dot{q} + \tau\ddot{q} = -gf, \quad (3.2)$$

with control gain  $g$  and filter time scale  $\tau \geq 0$ . For vanishing control gain ( $g = 0$ ) the control effort vanishes, while  $\tau = 0$  recovers the classic IFF control [33, 34] with performance equivalent to pure passive viscous damping. Combining eq. (3.1) and eq. (3.2) in the frequency domain provides the frequency dependent transfer relation between damper force and damper motion as in eq. (2.8), with the normalised transfer function  $H(\omega)$  now given by

$$H(\omega) = \frac{(1 + i\omega\tau)}{1 - \nu + i\omega\tau}, \quad (3.3)$$

where  $\nu = cg$  is the non-dimensional control gain. The frequency dependent function  $H(\omega)$  describes the modification of the damper force transfer relation for the hybrid viscous damper compared to the pure viscous damper associated with  $H(\omega) = 1$ . The real and the imaginary part of  $H(\omega)$  are given as

$$\text{Re}[H(\omega)] = \frac{1 - \nu + (\omega\tau)^2}{(1 - \nu)^2 + (\omega\tau)^2}, \quad \text{Im}[H(\omega)] = \frac{-\nu\omega\tau}{(1 - \nu)^2 + (\omega\tau)^2}, \quad (3.4)$$

from where it is seen that the condition  $\nu < 1$  corresponds to  $\text{Re}[H(\omega)] > 0$ , which secures  $\text{Im}[\bar{f}/\bar{u}] > 0$  and thus energy dissipation.

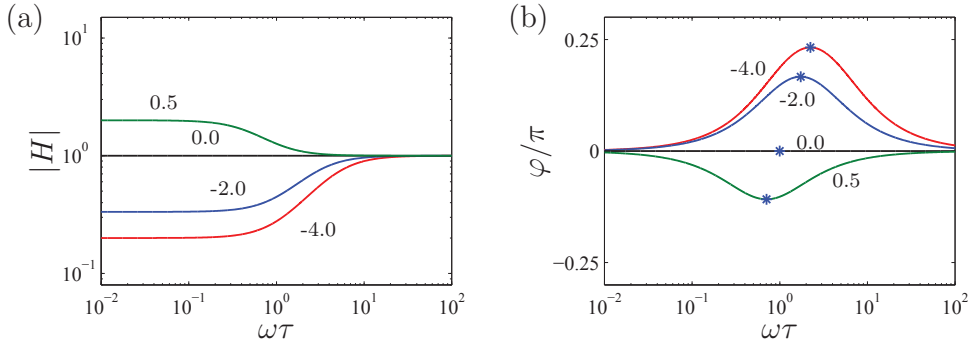


FIGURE 3.2. (a) Magnitude and (b) phase angle of the transfer function  $H(\omega)$  for  $\nu = 0.5$  (—),  $0.0$  (—),  $-2.0$  (—) and  $-4.0$  (—).

### 3.2.1. Increasing attainable damping

The performance of the hybrid damper is conveniently investigated by analysing the amplitude  $|H(\omega)|$  and phase angle  $\varphi$  of the transfer function. The amplitude  $|H(\omega)|$ , determined as

$$\left| \frac{\bar{u} - \bar{q}}{\bar{u}} \right| = |H(\omega)| = \sqrt{\frac{(1 + (\omega\tau)^2)}{(1 - \nu)^2 + (\omega\tau)^2}}, \quad (3.5)$$

also represents the amplification of the damper displacement across the viscous dash-pot, relative to the pure viscous case. The phase angle  $\varphi$  is determined from the relation

$$\tan(\varphi) = \frac{\text{Im}[H(\omega)]}{\text{Re}[H(\omega)]} = \frac{-\nu(\omega\tau)}{1 - \nu + (\omega\tau)^2}, \quad (3.6)$$

and describes the phase difference between the damper force  $f$  and the corresponding damper velocity  $\dot{u}$ , whereby  $\varphi = 0$  represents the passive viscous case where the damper force and the damper velocity are fully in phase.

The amplitude  $|H(\omega)|$  and phase angle  $\varphi$  are plotted in Fig. 3.2 for increasing values of the non-dimensional frequency  $\omega\tau$ . The individual curves in the figure represent the various non-dimensional gain values:  $\nu = 0.5$  (—),  $0.0$  (—),  $-2.0$  (—) and  $-4.0$  (—). As seen in Fig. 3.2(a) the amplitude decreases for increasing magnitude of  $\nu < 0$  compared to the passive case with  $\nu = 0$ , while it correspondingly increases in the positive gain interval  $0 < \nu < 1$ . From Fig. 3.2(b) the phase angle is seen to be positive  $\varphi > 0$  for  $\nu < 0$ , which means that the damper force  $f$  acts ahead of the damper velocity  $\dot{u}$  for negative gain values. Compared to the pure viscous case with  $\nu = 0$ , this phase lead results in increased attainable damping and thus improved damper performance [18, 19].

The phase lead is seen to have a maximum, marked by an asterisk in Fig. 3.2(b), at the non-dimensional angular frequency

$$\omega\tau = \sqrt{1 - \nu}, \quad (3.7)$$

and since optimum damping is associated with maximum phase lead the filter time scale should therefore be chosen as

$$\tau = \frac{\sqrt{1 - \nu}}{\omega_s}, \quad (3.8)$$

where  $\omega_s$  is the natural frequency of the targeted vibration form of the flexible structure. A drawback of the filtered IFF format in eq. (3.2) is that it leads to a pole at  $\omega = 0$  in the feedback relation, which may cause drift in the actuator displacement signal. If this drift becomes too large it may lead to saturation of the actuator signal and thus reduced performance. To limit this drift an additional filtering of the actuator velocity controlled by the corner frequency  $\omega_q$  can be introduced, whereby the control equation is extended to a full second order equation as

$$\tau \ddot{q} + (1 + \omega_q \tau) \dot{q} + \omega_q q = -gf. \quad (3.9)$$

In this relation the corner frequency  $\omega_q$  acts as a synthetic spring, introducing a restoring force towards the equilibrium state.

### 3.3. Numerical analysis of shear frame

To illustrate the damping performance of the hybrid viscous damper a numerical analysis is performed on a model of a 10-storey shear frame structure equivalent to the model used in [28] and [A3]. In the analysis the hybrid damper is installed between the first and second floor, as depicted in Fig. 3.1. The equations of motion for the structural degrees of freedom of the shear frame are described by the linear equations as in eq. (2.1), with the connection of the hybrid damper to the shear frame given by the connectivity vector

$$\mathbf{w} = [-1, 1, 0, \dots, 0]^T. \quad (3.10)$$

Further details about the shear frame model can be found in [A3]. For the hybrid damper the non-dimensional gains of  $\nu = 0.0$ ,  $-2.0$  and  $-4.0$  are applied, while the filter time scale is  $\tau = \sqrt{1 - \nu}/\omega_s^0$  according to eq. (3.8), where  $\omega_s^0$  in this case is the undamped natural frequency of the first vibration form of the shear frame. Structural damping is set to zero  $\mathbf{C} = \mathbf{0}$  in the present analysis, whereby the reported damping level in the model is entirely due to the presence of the hybrid damper.

#### 3.3.1. Root locus analysis

Initially, to demonstrate the performance of the hybrid damper a root locus analysis is conducted with respect to an increasing viscous coefficient  $c$  and thus with fixed values of both  $\nu$  and  $\tau$ , as discussed previously. Figure 3.3 shows the three root loci for the first vibration mode of the shear frame corresponding to  $\nu = 0.0$ ,  $-2.0$

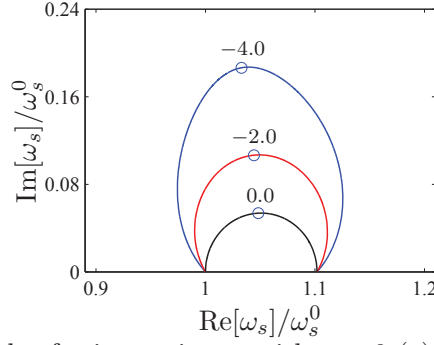


FIGURE 3.3. Root locus plot for increasing  $c$ , with  $\nu = 0$  (—),  $-2.0$  (—) and  $-4.0$  (—) and  $\tau = \sqrt{1 - \nu}/\omega_s^0$ .

and  $-4.0$ . The plot is scaled by the undamped first natural frequency of the shear frame  $\omega_s^0$ . From the root loci it is seen that improved damping performance is obtained for  $\nu < 0$ . The modal damping ratio  $\zeta = \text{Im}[\omega_s]/|\omega_s|$  is determined as the relative imaginary part of the associated complex-valued natural frequency  $\omega_s$ , and the optimal viscous coefficient with respect to the maximum modal damping ratio for each value of  $\nu$  is determined by a simple numerical search procedure. The circles in Fig. 3.3 represent the complex natural frequencies associated with these optimal viscous coefficients. For  $\nu = -4.0$  the maximum damping ratio is determined as  $\zeta_4 = 0.178$ , which is approximately three times larger than  $\zeta_0 = 0.051$  for  $\nu = 0.0$ , while for  $\nu = -2.0$  the maximum damping ratio is  $\zeta_2 = 0.102$ .

### 3.3.2. Transient analysis with ramp load

The root locus analysis presented in the previous section represents the idealised case of free vibrations, without any modal interaction due to external forcing. Now, a simple response analysis is conducted to illustrate the ability of the hybrid viscous damper to mitigate transient vibrations. At the top floor the frame is therefore loaded by a linearly increasing force, which is removed instantaneously after two vibration periods. In this way also higher vibration modes of the structure are activated and the results therefore also illustrate the influence from modal energy spill-over.

The displacement of the top floor is shown Fig. 3.4, where the curves are normalised by the static top-floor deflection corresponding to the load level  $p_0$  after two vibration periods. The damping ratios of the structure are estimated from the corresponding logarithmic decrement between the first and fourth maximum and minimum of the free response, and the exponentially decaying curves relative to the first maximum and minimum are plotted as dashed curves in Fig. 3.4. The decay curves represent the free vibration amplitudes fairly well and the average damping ratios are estimated as  $\zeta_0 = 0.053$ ,  $\zeta_2 = 0.093$  and  $\zeta_4 = 0.124$  for  $\nu = 0.0$ ,  $-2.0$  and  $-4.0$ , respectively. For the negative gain values ( $\nu < 0$ ) the estimated damping ratios from the transient response are somewhat lower than the corresponding

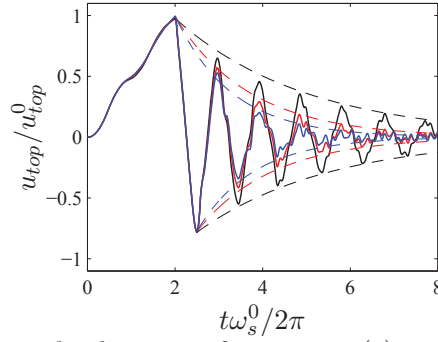


FIGURE 3.4. Top floor displacement for  $\nu = 0.0$  (—),  $-2.0$  (---) and  $-4.0$  (---).

estimates from the root loci in the previous section, which is probably due to the significant modal interaction introduced by the filtered force feedback. However, when compared with the pure viscous case  $\nu = 0$  the hybrid viscous damper with filtered force feedback and  $\nu < 0$  still introduces a significant increase in attainable damping.

#### 3.4. Increasing damper stroke

When setting the filter time scale to zero  $\tau = 0$  in the control equation (3.2), the pure IFF equation is recovered,

$$\dot{q} = -gf, \quad (3.11)$$

whereby the normalised transfer function  $H(\omega)$  between the damper force and the damper motion is given by the (frequency independent) constant

$$H(\omega) = \frac{1}{1 - \nu}, \quad (3.12)$$

where  $\nu < 1$  again represents the stability condition. As in eq. (3.5) the amplification of the damper stroke, relative to the pure viscous case represented by  $q = 0$ , is governed by the amplitude of  $H(\omega)$ , which can be written as

$$|H(\omega)| = \left| \frac{\bar{u} - \bar{q}}{\bar{u}} \right| = \left| \frac{1}{1 - \nu} \right|. \quad (3.13)$$

For non-dimensional gain values in the interval  $0 < \nu < 1$  the relative deformation of the viscous dash-pot is amplified, whereby the hybrid control format can be used to improve the feasibility of installing viscous dampers at locations in a flexible structure where the deformation magnitude is inherently small. Optimum tuning is given by eq. (2.12), where  $0 < \nu < 1$  is seen to reduce the value of the optimum damping coefficient  $c_{opt}$ .

### 3.4.1. Filtered integration

As for the filtered IFF control equation (3.2) the pure IFF equation in eq. (3.11) is prone to drift in the actuator displacement. To reduce drift a full second order filter with corner frequency  $\omega_f$  and filter time scale  $\tau_f$  is therefore proposed, whereby a modified integral force feedback equation is given as

$$\omega_f q + \dot{q} + \tau_f \ddot{q} = -gf. \quad (3.14)$$

This second order filter leads to a modified relation for the transfer function in eq. (3.12), which reduces drift, but also leads to reduced amplification and a phase difference between the damper force and damper velocity. The latter may deteriorate the damper performance of the hybrid damper. The performance of the unfiltered IFF scheme can however be retained at the structural frequency of the critical vibration mode  $\omega_s$ , by simply choosing the filter parameters  $\omega_f$  and  $\tau_f$  according to

$$\omega_f = \tau_f \omega_s^2. \quad (3.15)$$

With the above relation between the filter parameters, the magnitude and phase of the transfer function  $H(\omega)$  is retained exactly at the structural frequency  $\omega_s$ .

## 3.5. Time dependent simulations in HAWC2

To illustrate the potential of installing hybrid viscous dampers in a wind turbine tower to damp tower vibrations, a series of numerical simulations of the OC3 wind turbine is conducted in HAWC2<sup>1</sup> (Horizontal Axis Wind turbine simulation 2nd generation) [26]. Compared to the model used in [22], soil damping is tuned so that the overall damping ratio of the two lowest tower modes without aerodynamic damping is approximately  $\zeta_{struc} \approx 0.0115$ , while as in [22] a steady uniform wind field with a mean wind speed of 8 m/s is applied to include aerodynamic damping. The hybrid dampers are installed at the bottom of the tower using curvature braces as in section 2.3.1, and effectively implemented in the HAWC2 model using an external dynamic link library (dll), as explained in [16] for an advanced dynamic gear model.

### 3.5.1. Transient analysis with wave load

Initially, to illustrate the ability of the hybrid viscous damper to damp tower vibrations a transient decay analysis is conducted. The wind turbine is loaded by a wave train of three large waves applied at an angle of 45° to the rotor direction in order to excite both the fore-aft mode ( $y$ -direction) as well as the side-side mode ( $x$ -direction). Simulations are conducted for three cases: (a) without dampers, (b) with three passive viscous dash-pots and (c) with three hybrid dampers installed

---

<sup>1</sup> HAWC2 is an aeroelastic code developed at DTU Wind Energy intended for calculating wind turbine response in the time domain. The code has been used in numerous research projects and industrial applications [1].

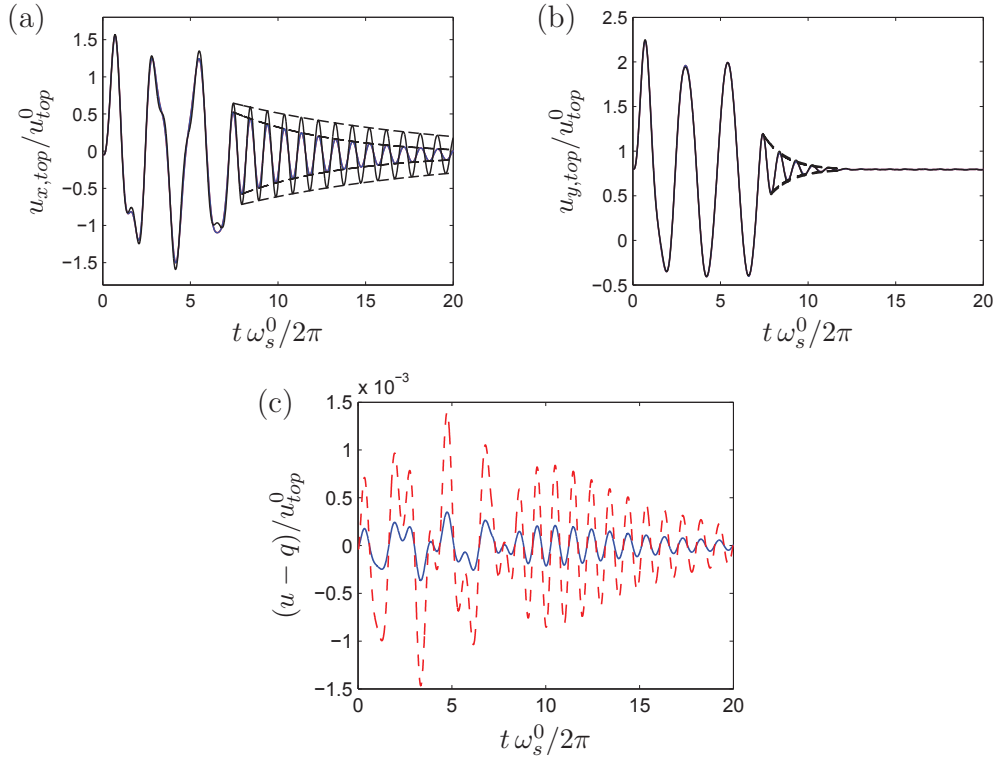


FIGURE 3.5. Tower top displacement in  $x$ -direction (a) and  $y$ -direction (b), and (c) displacement over the viscous dash-pot for  $\nu = 0$  (—) and for  $\nu = 0.75$  (---) with  $\omega_f = \tau_f\omega_s^2 = \omega_s/8$ , and without dampers (—).

inside the tower. For the hybrid dampers the gain parameter  $\nu = 0.75$  and the filter parameters  $\omega_f = \tau_f\omega_s^2 = \omega_s/8$  have been used.

As seen in Fig. 3.5(a,b) vibrations in the  $y$ -direction are damped significantly faster than the corresponding vibrations in the  $x$ -direction, due to the additional aerodynamic damping in the rotor direction. Without dampers the effective damping ratio for the fore-aft vibrations is estimated from the vibration decay by the logarithmic decrement method to  $\zeta_{fa,0} = 0.1123$ , while this value increases to  $\zeta_{fa} = 0.1267$  in the case with hybrid or viscous dampers, both significantly higher than at standstill. For the side-side vibrations the damping ratio is estimated to  $\zeta_{ss,0} = 0.0122$  for the case without supplemental dampers, while it increases to  $\zeta_{ss} = 0.0264$  with dampers. The small increase for the case without dampers compared to the case at standstill could be due to modal interaction with the fore-aft mode, which has a significantly larger modal damping ratio.

Based on the computed damping ratios the additional damping from the supplemental dampers is determined as  $\Delta\zeta_{fa} = 0.0144$  for the fore-aft vibrations and  $\Delta\zeta_{ss} = 0.0142$  for the side-side vibrations. These values are slightly larger than the expected values  $\zeta_{ss,max} = 0.0128$  and  $\zeta_{fa,max} = 0.0129$  obtained in Section

2.3.1, presumably due to the vibration modes being modified by the presence of the dampers. Inserting the dampers in the structure modifies the vibration modes slightly, whereby soil and aerodynamic damping could also be increased. Finally, in Fig. 3.5(c) the displacement across the viscous dash-pot in the hybrid damper is plotted. When comparing the pure passive case with the hybrid damper using  $\nu = 0.75$  the displacement across the dash-pot is amplified by approximately a factor of four, which agrees with the theoretical predictions from the expression in eq. (3.13). Thus, the present simulations conducted in HAWC2 show that the performance of the hybrid viscous damper is unaffected by aerodynamic damping, and that inherent and supplemental damping values are approximately additive, also during operation of the wind turbine.

### 3.5.2. Fatigue analysis

The fatigue limit state is a governing factor for the design of monopile support structures. In order to demonstrate that the hybrid viscous damper can reduce the accumulated damage in the monopile, a three hour wave load record is applied to the offshore wind turbine in HAWC2. The wave loading is generated as a three hour (10800 s) realisation of a common Pierson-Moskowitz spectrum, with a peak frequency of 0.1 Hz and significant wave height of 6 m, as also used in [22]. As for the previous analyses, the wave load is applied with a misalignment angle of  $45^\circ$  relative to the  $y$ -axis, whereby the fore-aft and the side-side directions receive the same force components. Simulations are conducted for two cases: (a) without dampers and (b) with three hybrid dampers installed inside the tower, where as before the gain parameter  $\nu = 0.75$  and the filter parameters  $\omega_f = \tau_f \omega_s^2 = \omega_s/8$  have been used. The simulations in HAWC2 with and without damper system are conducted for the same seed in the realisation of the wave loading, whereby the time histories for the damped response are directly comparable to those without damper system.

Figure 3.6 shows the time response histories of (a) the top tower position  $u_{x,top}$  in side-to-side  $x$ -direction and the base bending moment  $M_{y,base}$  around the  $y$ -axis at the bottom of the tower. The time  $t$  is normalised by the natural frequency  $\omega_s/(2\pi) = 0.2418$  Hz, and it is seen that the length of the time records in the figure corresponds to around 2600 vibration periods. The response of the wind turbine without damper is represented by the gray curve (–) in the background, while the red curve (–) in the front shows the damped response. The black dashed horizontal line (– –) indicates the (common) mean value, while the gray and red dashed lines represent the corresponding standard deviations. The maximum deflections and bending moments are indicated in the figure by the asterisk markers. It is seen that the top tower deflection is only reduced slightly by the hybrid damper system, with a reduction in maximum deflection (relative to mean) of 13% and a corresponding reduction in standard deviation of 23%. The reduction in the base moment at the bottom of the tower is significantly larger. The maximum bending moment (relative

to mean) is reduced by 38% due to presence of the hybrid damper system, while the standard deviation of the base moment is reduced by 49%.

A fatigue analysis is conducted based on the irregular response of the wind turbine tower using the rainflow counting procedure described in [27]. Typically (normal) stress cycles are detected and accumulated. However, in the present case the base bending moment  $M_{y,base}$  is used directly in the fatigue analysis. A standard rainflow counting procedure is applied to generate moment increments  $\Delta M_j$  from the base bending moment record. The accumulated damage  $D_M$  is then estimated by the summation

$$D = \sum_{j=1}^N \frac{\Delta M_j^m}{K}, \quad (3.16)$$

with power law exponent  $m$  and constant  $K$ , see [27]. The present results for the damage are normalised by the constant  $K$  and an exponent of  $m = 3$  is assumed. The accumulated damage ratio is obtained as  $D_d/D_0 = 0.13$ , while a corresponding damage ratio, corrected with respect to the individual number of cycles, is determined as 0.20, see [P2]. Both damage ratios indicate that the proposed hybrid damper system is able to reduce the accumulated damage and thereby increase the fatigue life of the offshore wind turbine.

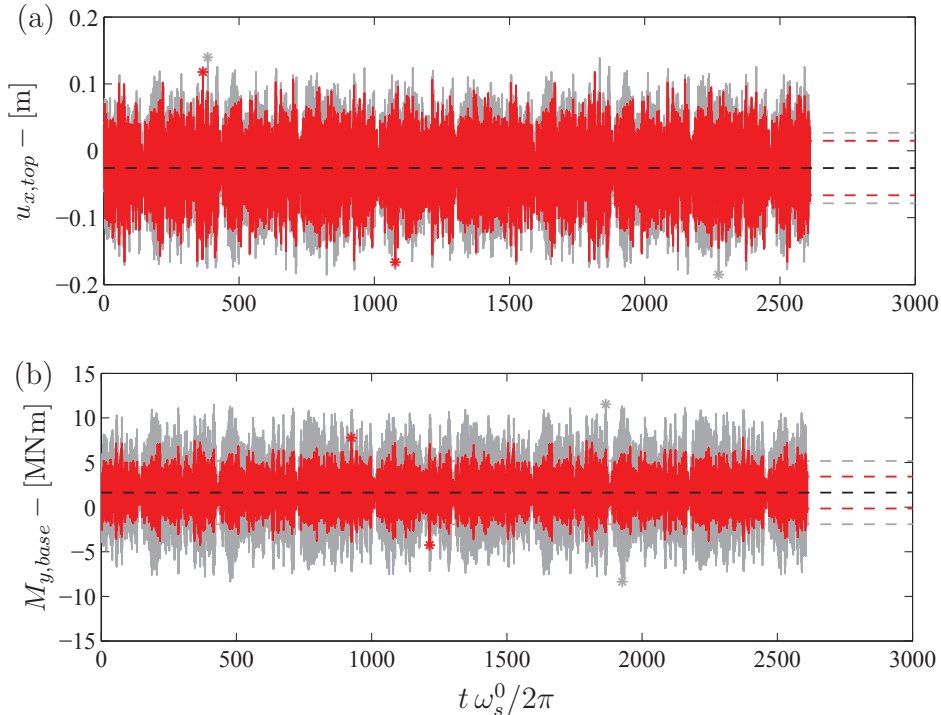


FIGURE 3.6. Tower top position in side-side  $x$ -direction (a) and base moment around  $y$ -axis (b).

## 4. ACTIVE TUNED MASS DAMPER

Effective damping of tower vibrations of offshore wind turbines by a Tuned Mass Damper (TMD) is associated with a large damper mass and a placement at the top of the wind turbine, which is highly undesirable. The significant additional mass of a TMD therefore constitutes a major limitation for its use with respect to damping of tower vibrations. An Active TMD (ATMD) is a hybrid device where the spring and damper of a passive TMD is supplemented by an actuator. It is a well known concept in structural control, especially for mitigation of excessive vibrations in high-rise buildings subjected to strong wind and earthquake loads, where the ATMD may enhance damping performance compared to the passive TMD [2, 35]. The concept has also been implemented in a number of high-rise buildings in Japan [21]. For optimal feedback control of the ATMD, different strategies have been proposed. Chang & Soong [5] proposed a state feedback scheme combined with a Linear Quadratic Regulator determined by minimising both the primary structural response and the control effort. Later Chang & Yang [4] assumed white noise excitation and used a complete feedback scheme in which the optimum gain parameters are determined from a minimisation of the response variance, while Nishimura [30] proposed a pure acceleration feedback format in which with optimum gain determined by a dynamic amplification analysis similar to that of the passive TMD. As demonstrated by Nishimura [30], for a single dof system, this acceleration scheme provides a reduction of the dynamic amplification of the primary mass compared to the TMD, but for the same damper mass and without any increase in the maximum dynamic amplification of the damper mass. However, for a flexible structure with an infinite number of dofs, the scheme has an inherent instability associated with a singularity in the mass matrix, which makes it unfeasible for practical implementation.

In the paper [P3] the ATMD concept is applied to a wind turbine for damping of tower vibrations. It is demonstrated that a simple feedback format based on the absolute displacement of the tower and the relative velocity of the damper mass can provide guaranteed stability and enhanced performance compared to the passive TMD for the same damper mass, whereby the ATMD can be considered an appealing alternative to the TMD concept for damping of tower vibrations. Tuning of the ATMD is based on a modal representation of the critical tower mode(s), and a simple procedure, equivalent to the tuning procedure of the passive TMD, combined with a simple minimisation of the active control force, provides the optimum

damper parameters and gain values. The optimum design of the proposed ATMD for damping of tower vibrations from [P3] is summarised in the following.

#### 4.1. Equation of motion for ATMD

A fixed offshore wind turbine with an Active Tuned Mass Damper (ATMD) is illustrated in Fig. 4.1(a). The ATMD is positioned at the top of the wind turbine, where the amplitude of the critical tower modes are expected to be largest. The ATMD consists of a damper mass  $m_a$  connected to the wind turbine through a linear spring  $k_a$ , a viscous dash-pot  $c_a$  and an actuator force  $f_a$ , as illustrated in Fig. 4.1(b). The ATMD exerts the force

$$f = c_a \dot{u}_a + k_a u_a - f_a, \quad (4.1)$$

on the wind turbine, while the equation of motion for the ATMD is given by

$$m_a \ddot{u}_a + c_a \dot{u}_a + k_a u_a = -m_a \mathbf{w}^T \ddot{\mathbf{u}} + f_a. \quad (4.2)$$

The connection of the ATMD to the tower is described by the connectivity vector  $\mathbf{w}$ , containing only zeros except at the dof at which the ATMD is attached. The actuator is regulated using feedback from the absolute displacement  $\mathbf{w}^T \mathbf{u}$  of the tower and the relative velocity  $\dot{u}_a$  of the damper mass, whereby the actuator force is given by

$$f_a = -G_k \mathbf{w}^T \mathbf{u} - g_c c_a \dot{u}_a, \quad (4.3)$$

where  $G_k$  is the gain associated with the absolute displacement of the tower, and  $g_c$  is the non-dimensional gain associated with feedback of the relative velocity of the damper mass. The actuator force from eq. (4.3) is initially substituted into both the equation for the ATMD in eq. (4.2) and the corresponding equation for the ATMD force in eq. (4.1), and these equations are subsequently combined with

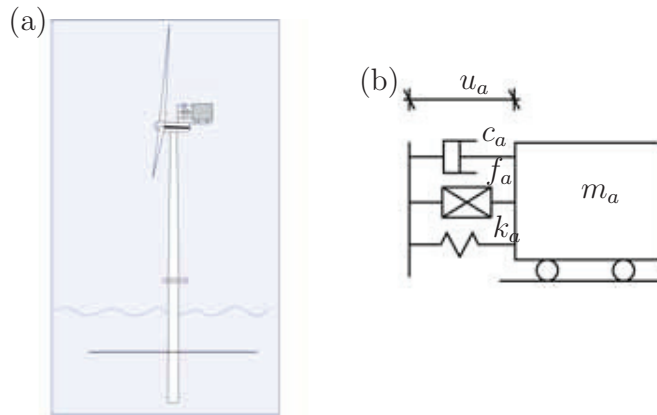


FIGURE 4.1. (a) Fixed offshore wind turbine with (b) ATMD.

the equations of motion for the wind turbine in eq. (2.1) to determine the final closed-loop system of equations for the wind turbine and ATMD,

$$\begin{aligned} \begin{bmatrix} \mathbf{M} + \mathbf{M}_a & \mathbf{w}m_a \\ m_a\mathbf{w}^T & m_a \end{bmatrix} \begin{bmatrix} \ddot{\mathbf{u}}(t) \\ \ddot{u}_a(t) \end{bmatrix} + \begin{bmatrix} \mathbf{0}\mathbf{0}^T & \mathbf{0} \\ \mathbf{0}^T & (1 + g_c)c_a \end{bmatrix} \begin{bmatrix} \dot{\mathbf{u}}(t) \\ \dot{u}_a(t) \end{bmatrix} \\ + \begin{bmatrix} \mathbf{K} & \mathbf{0} \\ G_k\mathbf{w}^T & k_a \end{bmatrix} \begin{bmatrix} \mathbf{u}(t) \\ u_a(t) \end{bmatrix} = \begin{bmatrix} \mathbf{f}(t) \\ 0 \end{bmatrix}. \end{aligned} \quad (4.4)$$

The combined mass matrix  $\mathbf{M} + \mathbf{M}_a = \mathbf{M} + \mathbf{w}\mathbf{w}^T m_a$  is the original mass matrix of the wind turbine plus the additional mass of the ATMD. The stiffness matrix is seen to be positive definite for any value of  $G_k$ , while for  $g_c > -1$  the damping matrix is positive semi-definite. For gain values  $g_c > -1$  all eigenfrequencies therefore have positive imaginary part, whereby the system is stable.

#### 4.2. Optimum modal tuning

Optimum tuning of the ATMD is based on the dynamic amplification of the wind turbine, similar to the optimum tuning of the passive TMD. The displacement of the wind turbine is conveniently described by a modal representation in terms of the mode-shape vector  $\mathbf{u}_j$  and modal coordinate  $r_j$  as

$$\mathbf{u}(t) = \mathbf{u}_j r_j(t), \quad (4.5)$$

whereby the modal mass and modal stiffness associated with mode  $j$  are given by  $m_j = \mathbf{u}_j^T \mathbf{M} \mathbf{u}_j$  and  $k_j = \mathbf{u}_j^T \mathbf{K} \mathbf{u}_j$ . Inserting eq. (4.5) into eq. (4.4) gives the equations of motion for the modal coordinate  $r_j$  and the relative displacement  $u_a$  of the ATMD as

$$\begin{aligned} \begin{bmatrix} (1 + \mu_j) & \mu_j \\ 1 & 1 \end{bmatrix} \begin{bmatrix} \ddot{r}_j(t) \\ \ddot{u}_a(t) \end{bmatrix} + \begin{bmatrix} 0 & 0 \\ 0 & (1 + g_c)2\zeta_a\omega_a \end{bmatrix} \begin{bmatrix} \dot{r}_j(t) \\ \dot{u}_a(t) \end{bmatrix} \\ + \begin{bmatrix} \omega_j^2 & 0 \\ g_k\omega_j^2/\mu_j & \omega_a^2 \end{bmatrix} \begin{bmatrix} r_j(t) \\ u_a(t) \end{bmatrix} = \begin{bmatrix} f_j(t)/m_j \\ 0 \end{bmatrix} \end{aligned} \quad (4.6)$$

where  $f_j = \mathbf{u}_j^T \mathbf{f}$  is the modal load. The equations are characterised by the modal mass ratio  $\mu_j = m_a/m_j$ , the natural frequency  $\omega_j = \sqrt{k_j/m_j}$  associated with mode  $j$ , the frequency  $\omega_a = \sqrt{k_a/m_a}$  of the ATMD, the damping ratio  $\zeta_a = c_a/(2\sqrt{m_a k_a})$  of the ATMD, the non-dimensional feedback gain  $g_k = G_k/k_j$  associated with displacement of the tower, and the non-dimensional gain parameter  $g_c$ . Assuming harmonic solutions with modal amplitude denoted by a bar and  $\omega > 0$  as the forcing frequency, the dynamic amplification of the modal coordinate  $r_j$  is given by

$$\frac{\bar{r}_j}{r_{j,sta}} = \frac{\omega_j^2 [\omega_a^2 - \omega^2 + 2i(1 + g_c)\zeta_a\omega_a\omega]}{\omega^4 - [\omega_j^2(1 - g_k) + \omega_a^2(1 + \mu_j)]\omega^2 + \omega_a^2\omega_j^2 + 2i(1 + g_c)\zeta_a\omega_a\omega[\omega_j^2 - \omega^2(1 + \mu_j)]}, \quad (4.7)$$

where  $r_{j,sta} = \bar{f}_j/k_j$  is the static displacement associated with the targeted vibration mode  $j$ .

#### 4.2.1. Frequency tuning

As seen from the dynamic amplification of the modal coordinate  $r_j$  in Figure (4.2) implementation of the ATMD gives rise to two "neutral frequencies",  $\omega_A$  and  $\omega_B$ , around the structural frequency  $\omega_j$ , at which the magnitude of the frequency response is independent of the added damping. The optimum frequency tuning of the ATMD is determined by setting the magnitude at these two neutral frequencies equal to each other, equivalent to the optimum frequency tuning of the passive TMD, credited to Den Hartog [11]. The neutral frequencies  $\omega_A$  and  $\omega_B$  are determined first, by setting the magnitude of eq. (4.7) equal at the two limits  $(1 + g_c)\zeta_a = 0$  and  $(1 + g_c)\zeta_a \rightarrow \infty$ . Then the response magnitude at these two frequencies are set equal to each other, whereby the optimum frequency tuning of the ATMD is determined as

$$\frac{\omega_a}{\omega_j} = \frac{1}{\sqrt{2}} \frac{\sqrt{2 + g_k + g_k\mu_j}}{1 + \mu_j}. \quad (4.8)$$

The optimum frequency tuning is seen to depend both on the mass ratio  $\mu_j$  and the gain parameter  $g_k$ . Furthermore,  $g_k = -2/(1 + \mu_j)$  is seen to correspond to a design limit, since it leads to the frequency tuning  $\omega_a = 0$ . For  $g_k \rightarrow 0$  the optimum tuning in [11] of the passive TMD is recovered. From the optimum frequency tuning in (4.8) the dynamic amplification  $A_{max}$  at the neutral frequencies is determined as

$$A_{max} = \sqrt{\frac{2 + \mu_j}{\mu_j - g_k - g_k\mu_j}}. \quad (4.9)$$

Comparing this solution to the dynamic amplification of the passive TMD, the ATMD is seen to offer further reduction in the dynamic amplification by appropriate choice of  $g_k < 0$ , while in the limit  $g_k \rightarrow 0$  the dynamic amplification of the

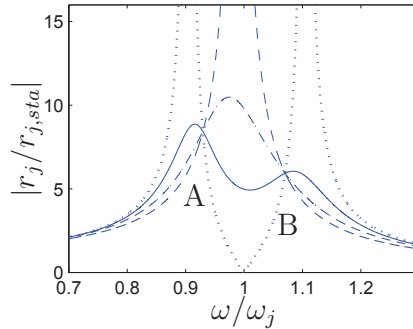


FIGURE 4.2. Dynamic amplification for  $\mu_j = -g_k = 0.02$ ,  $\omega_a = \omega_j$  and  $\zeta_a(1 + g_c) = 0.0$  ( $\cdot \cdot$ ),  $0.1$  ( $-$ ),  $0.2$  ( $- \cdot -$ ) and  $\infty$  ( $- -$ ).

mechanical TMD is recovered. The design limit  $g_k = -2/(1 + \mu_j)$  from eq. (4.8) is seen to correspond to  $A_{max} = 1$ , equivalent to no dynamic amplification.

#### 4.2.2. Damper tuning

With the optimum frequency tuning in eq. (4.8) the dynamic amplification at the two neutral frequencies is equal, and damping of the ATMD should therefore be scaled, so that a flat plateau between the two neutral frequencies is obtained. In [25] Krenk determined the optimum damper tuning of the passive TMD by selecting a frequency  $\omega_\infty$  in between the two neutral frequencies and then setting the dynamic amplification equal at the three frequencies  $\omega_a$ ,  $\omega_\infty$  and  $\omega_B$ . Hereby, a flat plateau is obtained. The same approach is applied in the present case for the ATMD. The dynamic amplification at the intermediate frequency  $\omega_\infty = \sqrt{k_j/(m_j + m_a)}$ , corresponding to the frequency when the viscous dash-pot is locked, is set equal to the dynamic amplification at the two neutral frequencies, whereby the optimum damping ratio is given as

$$(1 + g_c)\zeta_a = \sqrt{\frac{1}{2} \frac{\mu_j - g_k - g_k\mu_j - g_k^2/8 - g_k^2\mu_j/4 - g_k^2\mu_j^2/8}{1 + \mu_j + g_k/2 + g_k\mu_j + g_k/2\mu_j^2}}. \quad (4.10)$$

For  $g_k = g_c = 0$  the optimum damper tuning of the passive TMD in [25] is recovered.

#### 4.2.3. Tuning for reduction of control force

Proper tuning of the gain parameter  $g_c$  is determined by studying the frequency response of the active control force of the ATMD, as seen in Fig. 4.3. The active control force has two terms, the first proportional to  $G_k = g_k k_j$ , the second proportional to  $g_c$ . Close to the structural frequency  $\omega_j$  the control force proportional to  $g_k$  will be approximately  $180^\circ$  out of phase with the control force proportional to  $g_c$ , whereby the two terms seem to cancel. For the tuning

$$g_c^{opt} = -\frac{g_k \omega_j^2}{\mu_j \omega^2}, \quad (4.11)$$

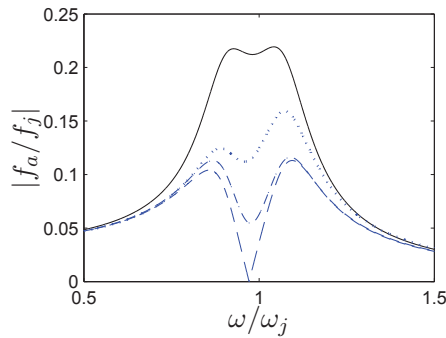


FIGURE 4.3. Magnitude of the the normalised control force, for  $g_c = 0$  (—),  $g_c = g_c^{opt}/2$  (— · —),  $g_c = g_c^{opt}$  (— —) and  $g_c \rightarrow \infty$  (· · ·), and for  $\mu = 0.02$  and  $A_{max} = 6$ .

the two terms in fact are found to cancel completely at the frequency  $\omega = \omega_a$ , whereby the control force vanishes. Compared to the case with  $g_c = 0$  (–), the tuning in eq. (4.11) gives a significant reduction in the control force around  $\omega_j$ , while for  $\omega \rightarrow 0$  and  $\omega \rightarrow \infty$  the difference for various values for  $g_c$  becomes insignificant. The tuning in eq. (4.11) is in the following chosen as the optimum tuning of  $g_c$ , since it effectively reduces the control effort around the resonance frequency.

#### 4.3. Frequency response analysis in HAWC2

To illustrate the performance of the ATMD a frequency response analysis is conducted in HAWC2 with the OC3 wind turbine described in Section 4.1. In order to introduce damping to both the side-side vibrations and the fore-aft vibrations two ATMDs are installed at the top of the tower with the same properties for both dampers. The ATMDs are implemented in the HAWC2 model using an external dll. Compared to the simulations in Section 3.5, the present analysis is conducted for the wind turbine at standstill and without wind, whereby aerodynamic effects are omitted. In the simulations the wind turbine is loaded by a time harmonic force at MSL with a series of different frequencies around resonance, and the amplitude of the steady state response is determined for each series once the initial transient response has disappeared. Four different scenarios are analysed: Active damping with  $A_{max} = 6$ , active damping with  $A_{max} = 10$ , and passive damping with  $A_{max} = 14.18$ , all with a damper mass ratio  $\mu_j = 0.01$ . The final scenario is without any external damping corresponding to  $\mu_j = 0.00$ . The properties for the ATMDs are given in Table 4.1.

The computed dynamic amplification for the wind turbine tower top and damper displacement for the two directions are shown in Fig. 4.4. As expected the tower top responses for the two directions are seen to be almost the same. Assuming that the wind turbine is vibrating primarily in one mode at resonance the dynamic amplification is approximately given by  $1/(2\zeta)$ . For the case without a damper the amplitude at resonance is approximately 44.6 which corresponds to a damping ratio of  $\zeta_{struc} = 0.0115$  for soil and structural damping alone, equivalent to the results in Section 3.5. As demonstrated for the passive TMD in [25] the tuning in eq. (4.8) corresponds to dividing the added damping equally between the two modes. Assuming that the tower top response at the two "neutral frequencies" is given by

TABLE 4.1. ATMD properties for  $\mu = 0.01$

$A_{max}$	$\omega_a/(2\pi)$ [Hz]	$\zeta_a(1 + g_c)$ [%]	$m_a$ [kg]	$k_a$ [N/m]	$c_a$ [N-s/m]	$g_k$	$g_c$
14.18	0.2361	7.04	4450	9796	929	0.000	0.00
10	0.2355	9.98	4450	9747	649	-0.010	1.03
6	0.2334	16.75	4450	9572	381	-0.045	4.74

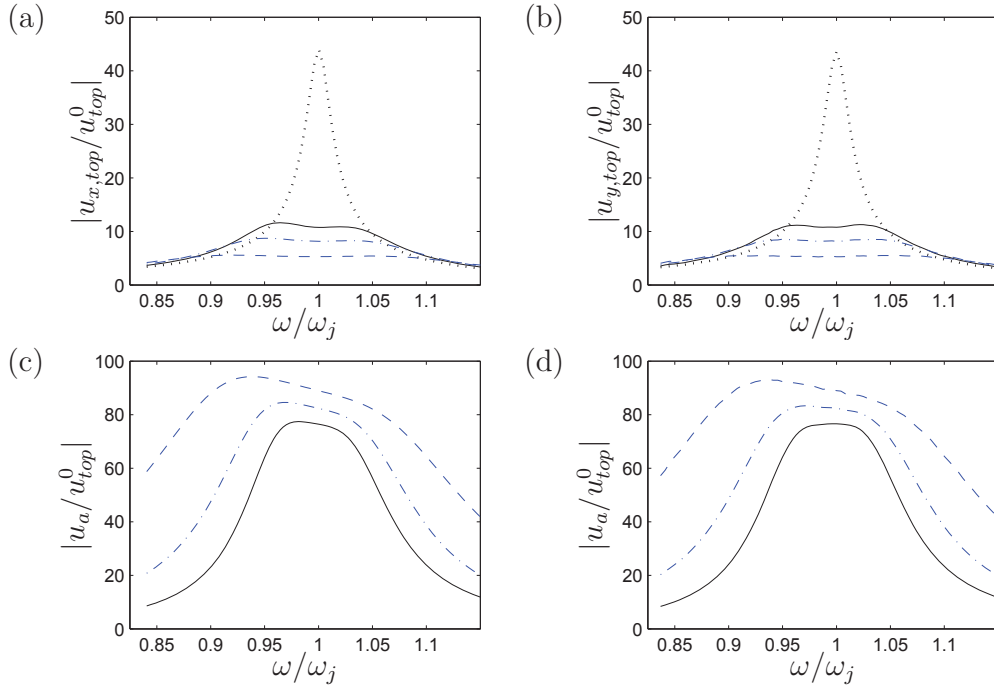


FIGURE 4.4. Dynamic amplification of tower top in (a) sideways and (b) rotor direction and of damper mass in (c) sideways and (d) rotor direction. Dynamic amplification  $A_{max} = 14.17$  ( $g_k = g_c = 0$ ) (—),  $A_{max} = 10$  (- · -) and  $A_{max} = 6$  (- -) with  $\mu = 0.01$ , and without damper ( $\mu_j = 0.00$ ) (· ·).

$1/(2\zeta)$  the damping ratio for the passive case is the estimated to  $\zeta_{14} = 0.0467$ , which corresponds well with half the added damping  $\Delta\zeta_{14} = 0.0352$  according to Table 4.1 plus the inherent structural damping  $\zeta_{struc} = 0.0115$ . By the same procedure the critical damping ratio for the case with  $A_{max} = 10$  is estimated to  $\zeta_{10} = 0.0613$ , while for  $A_{max} = 6$  the estimation gives  $\zeta_6 = 0.0948$ . This again corresponds well with half the added damping  $\Delta\zeta_{10} = 0.0499$  and  $\Delta\zeta_6 = 0.0837$  plus the inherent damping of  $\zeta_{struc} = 0.0115$ . Thus, structural damping, soil damping and damping due to the ATMD seems to be additive in the frequency domain. Comparing the displacement of the damper mass in Fig. 4.4(c) and (d) the displacement is seen to increase as  $A_{max}$  is decreased. Thus, the decrease in damper mass is accompanied by an increase in damper displacement, which therefore constitutes one of the main limitations of the proposed ATMD concept.

## 5. REAL TIME HYBRID SIMULATIONS OF HYBRID VISCOUS DAMPER

The hybrid viscous damper described in Chapter 3 has the potential to increase either the attainable damping or the damper stroke, compared to the pure passive case. In practice the performance of the hybrid viscous damper is limited by especially the inherent delay between sensor measurements and actuator response. Furthermore, a passive dash-pot with a pure viscous force response, as used in the hybrid viscous damper, represents an idealised case, which is not fully achievable in practice. Thus, it is of interest to perform physical tests for evaluating the performance of the hybrid viscous damper. However, large scale tests of dampers in structures are both expensive and cumbersome. Real time hybrid simulation (RTHS) is a test method that involves the technique of substructuring, where the structural system is divided into an *experimental substructure* and a *numerical substructure*, which are tested together as a single system in real time. In this way the physical test setup can be limited to the most critical sub-components of a structure, usually of reduced size and with undefined properties. Since the test is executed in real time it allows for physical testing of dampers and dissipative devices in connection with a numerical model of a primary structure [3,6].

In the paper [P4] results from a series of RTHS experiments are presented, where a physical model of the hybrid viscous damper is tested together with a numerical model of both a shear frame and an offshore wind turbine, in order to validate the results obtained in [A3] and [P2]. The results demonstrate that the hybrid viscous damper can be used to increase damping or to amplify the displacement across the damper. However, the results also show that discrepancies between the desired damper force response and the actual damper force response may to some extent deteriorate the performance of the hybrid viscous damper. The following chapter presents a description of the experimental setup and a presentation of the most important results.

### 5.1. *Experimental setup*

In a RTHS the test structure is divided into two parts: An experimental substructure represented by a physical model in the laboratory and a numerical substructure represented by a numerical or mathematical model. In the present analysis RTHS

is applied for the analysis of a model of the hybrid viscous damper attached to two types of structures: A 10 storey shear frame structure loaded by a ramp load and an offshore wind turbine structure loaded by a wave train of three waves. For the hybrid damper in the shear frame, the actuator displacement is regulated by a filtered IFF to enhance the damping performance, whereby these results obtained by RTHS are comparable to the numerical results obtained in Section 3.3.2. For the hybrid damper in the offshore wind turbine the actuator displacement is regulated by an IFF controller with the main purpose to increase damper displacement, whereby the results obtained from the RTHS are comparable to the numerical results presented in Section 3.5.1. The hybrid damper model, composed of a magnetorheological (MR) damper in series with an actuator and a load cell, is considered as the experimental substructure, while the primary structure (shear frame or wind turbine) is represented by the numerical substructure. The numerical model receives as input the damper force of the hybrid viscous damper measured by the load cell, while it returns the displacement of the hybrid viscous damper at the interface by means of actuators in the experimental substructure.

#### 5.1.1. Numerical substructure

A main limitation of RTHS is the inherent time delay between the numerical substructure and the experimental substructure. The time delay is mainly dictated by the actuator transfer system, communication delays as well as the computational delays in solving for the dofs in the numerical substructure. Thus, in order to keep the time delay within a feasible limit the numerical substructure should have a limited number of dofs. The numerical substructure with the shear frame is identical to the model used in Section 3.3.2, while for the wind turbine a simplified linear beam model is used with only eight dofs, representing only displacements in the side-side direction. Both models are represented by equations of motion given as in eq. (2.1). Structural damping is omitted in the simulations, whereby all damping in the model is due to the hybrid viscous damper. Due to a limited sampling rate and the inherent phase lags and time delays that may cause instabilities, the total damper force  $f$  is partitioned into two parts: the force  $f_e$  from the actual hybrid damper representing the experimental substructure and  $f_n$  from a numerical hybrid viscous damper model contained in the numerical substructure. Thus, the resulting damper force is given by the sum

$$f(t) = f_e(t) + f_n(t). \quad (5.1)$$

The ratio between the damper force from the experimental substructure and the damper force from the numerical substructure is regulated by a mixing parameter  $\eta$ , which simply determines the ratio between the viscous parameter  $c_e$  realised by the controllable MR damper in the experimental substructure and the remaining viscous parameter  $c_n$  in the numerical substructure. Thus, the split in eq. (5.1) of the total damper force can instead be represented by the following split of the *total*

viscous damping parameter  $c_{tot}$  into

$$c_e = \eta c_{tot} \quad , \quad c_n = (1 - \eta) c_{tot}. \quad (5.2)$$

By changing the value of  $\eta$  from 0 to 1 the corresponding ratio between the damper force in the numerical and the experimental substructures shifts between the case where the entire damper force is computed numerically ( $\eta = 0$ ) and the situation where the damper force is fully represented in the experimental substructure ( $\eta = 1$ ).

### 5.1.2. Experimental substructure

The experimental substructure consist of a physical model of the hybrid viscous damper. The idealised viscous dash-pot is in the experimental substructure replaced by a semi-active MR damper, which is regulated to emulate the velocity proportional damper force of the ideal viscous dash-pot. The MR damper is placed in series with a hydraulic actuator and a load cell, as shown in Figure 5.1. The load cell measures the damper force  $f_e^m(t)$  produced by the MR damper in the experimental substructure, and the interface between the experimental substructure and the numerical substructure is realised by a high performance Speedgoat/xPC real-time kernel.

The actuator is equipped with an internal Linear Variable Differential Transformer (LVDT), which measures the actuator displacement and thereby the deformation of the MR damper. The measured actuator displacement is controlled in an inner loop by a SC6000 controller and in an outer loop by a robust integrated actuator control strategy. The inner loop stabilises the actuator, while the outer loop guarantees that the desired damper deformation derived from the numerical substructure and the

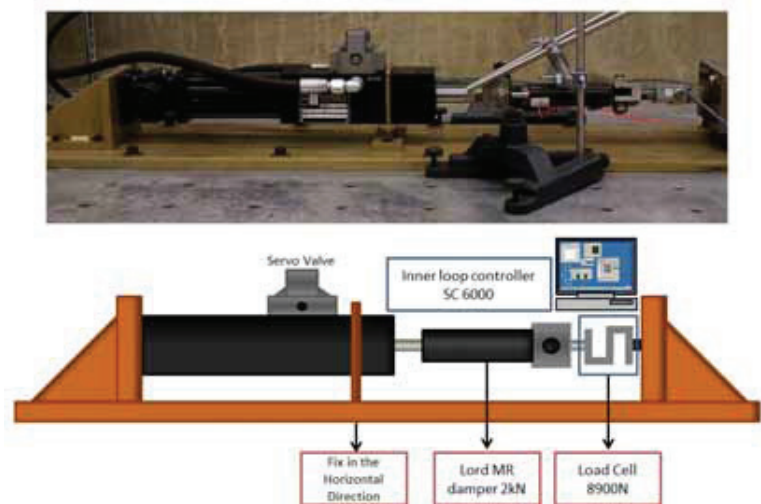


FIGURE 5.1. Experimental setup.

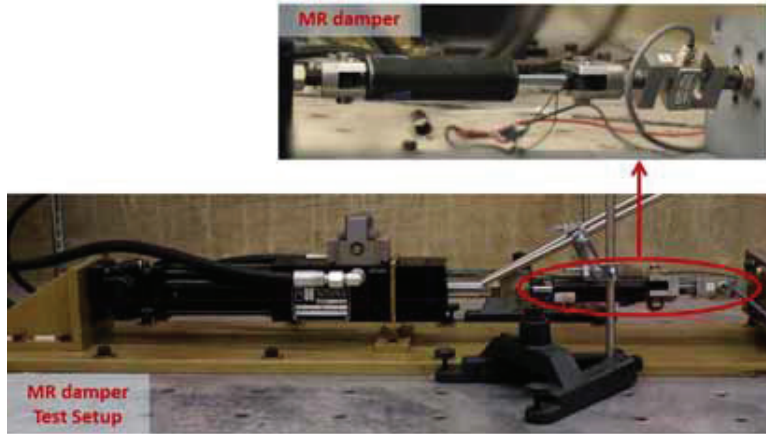


FIGURE 5.2. MR damper test setup.

control equation is implemented appropriately, see [32]. Figure 5.2 shows the MR damper, which is a model RD-8041-1 produced by LORD company, with a specified peak to peak damper force of approximately 2.4 kN when subjected to a velocity of 0.05 m/s at 1 A current input. To reproduce the performance of the hybrid viscous damper the MR damper is controlled using a bang-bang feedback control algorithm. This bang-bang control emulates the behavior of the idealised viscous dash-pot by tracking the desired force  $f_e^d$  of the ideal viscous damper contained in the experimental substructure. The bang-bang controller compares the measured damper force  $f_e^m$  from the load cell with the desired force  $f_e^d$  obtained by the control equation, and determines the command current  $I$  that allows the actual force in the MR damper  $f_e^m$  to track the corresponding desired force  $f_e^d$ . The bang-bang control is an on-off strategy, where maximum current  $I = I_{max}$  is applied when  $f_e^m < f_e^d$ , while  $I = 0$  in the opposite case when  $f_e^m > f_e^d$ . Furthermore, in order to account for the large variation in the desired damper force  $f_e^d$  the force tracking also involves a nonlinear force mapping from the numerical model to the experimental substructure. The force measured in the experimental setup is multiplied with an appropriate factor before it is transmitted to the numerical substructure, and the computed displacement from the numerical substructure is subsequently divided by the same factor before it is fed back to the actuator in the experimental setup. Further details concerning this nonlinear mapping can be found in the paper by Ou & Dyke [31].

A schematic overview of the RTHS setup is provided in the block diagram in Fig. 5.3. The *Finite Element model* in the block diagram represents the governing equations of motion. The input to this numerical model is the external load  $\mathbf{f}$  and the measured damper force  $f_e^m$  from the load cell. The output of this block is the computed displacements and velocities, and in particular the deformation of the hybrid viscous damper  $u = \mathbf{w}^T \mathbf{u}$  and its velocity component  $\dot{u} = \mathbf{w}^T \dot{\mathbf{u}}$ . The displacement of the actuator is determined by the *force feedback controller* block, which receives

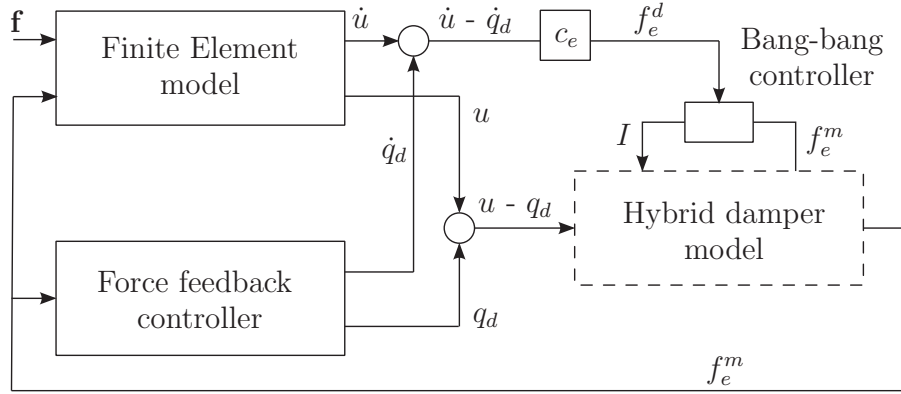


FIGURE 5.3. Schematic overview of the RTHS setup in block diagrams.

the measured damper force  $f_e^m$  as input. The output of this block is the desired actuator displacement  $q_d$  and its velocity  $\dot{q}_d$ , determined by solving eq. (3.9) for the shear frame with filtered IFF control and by eq. (3.14) for the wind turbine with the stroke amplifying IFF. Note that in both eqs. (3.9) and (3.14) the input is only the experimentally measured damper force  $f_e^m$ , due to the partitioning in eq. (5.1). The desired viscous damper force  $f_e^d = c_e (\dot{u} - \dot{q}_d)$  is then input to the *Bang-bang controller*, which is used to control the MR damper via the damper current  $I$ . The damper deformation  $u - q_d$  is passed on to the hydraulic actuator. In the present experiment the hydraulic actuator acts both as the active element in the hybrid damper and as interface, transferring the displacement of the numerical substructure to the experimental substructure. The displacement of the actuator is therefore given as the combined sum of the command displacement  $-q_d$  from the *force feedback controller* and the hybrid damper displacement  $u = \mathbf{w}^T \mathbf{u}$  computed by the *Finite Element model* in the numerical substructure. The output of the *hybrid damper model* is the damper force in the experimental substructure measured by the load cell.

## 5.2. RTHS with shear frame and filtered IFF controller

The present section presents results from the RTHS with the hybrid viscous damper installed in a shear frame, where the actuator displacement is regulated by a filtered IFF control for enhanced damping performance as presented in Section 3.2.1. In the RTHS a mixing parameter of  $\eta = 0.5$  is used, and the experimental results are compared with numerical results corresponding to  $\eta = 0$ .

### 5.2.1. Force tracking and actuator drift

Initially, it is illustrated how an error in the force tracking influences the drift in the actuator signal and thereby the damper displacement. To facilitate a comparison the desired damper force  $f_e^d$  is compared with the measured damper force  $f_e^m$ , while

the desired damper displacement  $u - q_e$  sent to the actuator is compared with the corresponding damper displacement  $u - q$  obtained by a direct numerical time integration of the equations of motion for  $\eta = 0$ . The results are presented in Fig. 5.4 for  $\nu = -2.0$ , and with  $\omega_q = \omega_s/20$  (a,b),  $\omega_q = \omega_s/8$  (c,d) and  $\omega_q = \omega_s/5$  (e,f). The damper force is scaled by the force  $p_0$  corresponding to the load level after two vibration periods, while the displacement are scaled by the static tower top displacement  $u_{top}^0$  corresponding to this load level. The difference between the desired and measured damper force represents the force tracking error, while the difference between the desired damper displacement and the displacement from a numerical simulation represents the drift of the actuator displacement. As seen from Fig. 5.4(a,c,e) the force tracking is in fact quite accurate, as the measured force  $f_e^m$  seems to track the desired damper force  $f_e^d$  quite well. However, especially around the local peaks the bang-bang control tends to overshoot the desired damper force, which, as shown later in Section 5.2.2, leads to a slightly reduced damping performance. The comparison between the desired damper displacement and the computed displacement shown in Fig. 5.4(b,d,f) shows larger differences than for the damper force comparison.

The relative error in the force tracking  $\varepsilon_f = (f_e^m - f_e^d)/f_{e,max}^d$  and the relative error in the damper displacement  $\varepsilon_{uq} = (u - q_d - (u - q))/(u - q)_{max}$  are plotted as red solid curves, supplemented by the mean values  $\bar{\varepsilon}_f$  and  $\bar{\varepsilon}_{uq}$  at the upper right corner of each sub-figure. Both error signals are filtered twice by a rectangular window function of length  $T_1 = 2\pi/\omega_s$ , in order to highlight the low frequency content of the force error that leads to drift in the actuator signal. The tracking errors  $\varepsilon_f$  for the three different simulations are seen to be very similar, and largest at the beginning where the load is ramped up. Comparing the relative error in the force tracking  $\varepsilon_f$  with the relative error in the damper displacement  $\varepsilon_{uq}$  during the first two vibration periods ( $t < 4\pi/\omega_s$ ) there seems to be a tendency that a positive force error  $\varepsilon_f > 0$  coincides with a negative slope in the displacement error  $d\varepsilon_{uq}/dt < 0$ . After the two initial periods the external load is removed and the error in the damper force in general becomes smaller ( $\varepsilon_f \rightarrow 0$ ), which agrees well with the magnitude of the displacement error also becoming smaller ( $\varepsilon_{uq} \rightarrow 0$ ). Furthermore, it is observed that for increasing values of the corner frequency  $\omega_q = \omega_s/20$ (b)  $< \omega_q = \omega_s/8$ (d)  $< \omega_q = \omega_s/5$ (f), the magnitude of the displacement error  $\varepsilon_{uq}$  descends towards zero at a faster rate, whereby the drift in the damper displacement is reduced. Since the curves for the tracking error  $\varepsilon_f$  in Fig. 5.4(a,c,e) seem to be almost identical, the observed reduction in drift in Fig. 5.4(b,d,f) is most likely due to the increase in corner frequency  $\omega_q$ . Thus, the filtered integration of the actuator velocity controlled by the corner frequency  $\omega_q$  is seen to reduce actuator drift induced by errors in the force tracking.

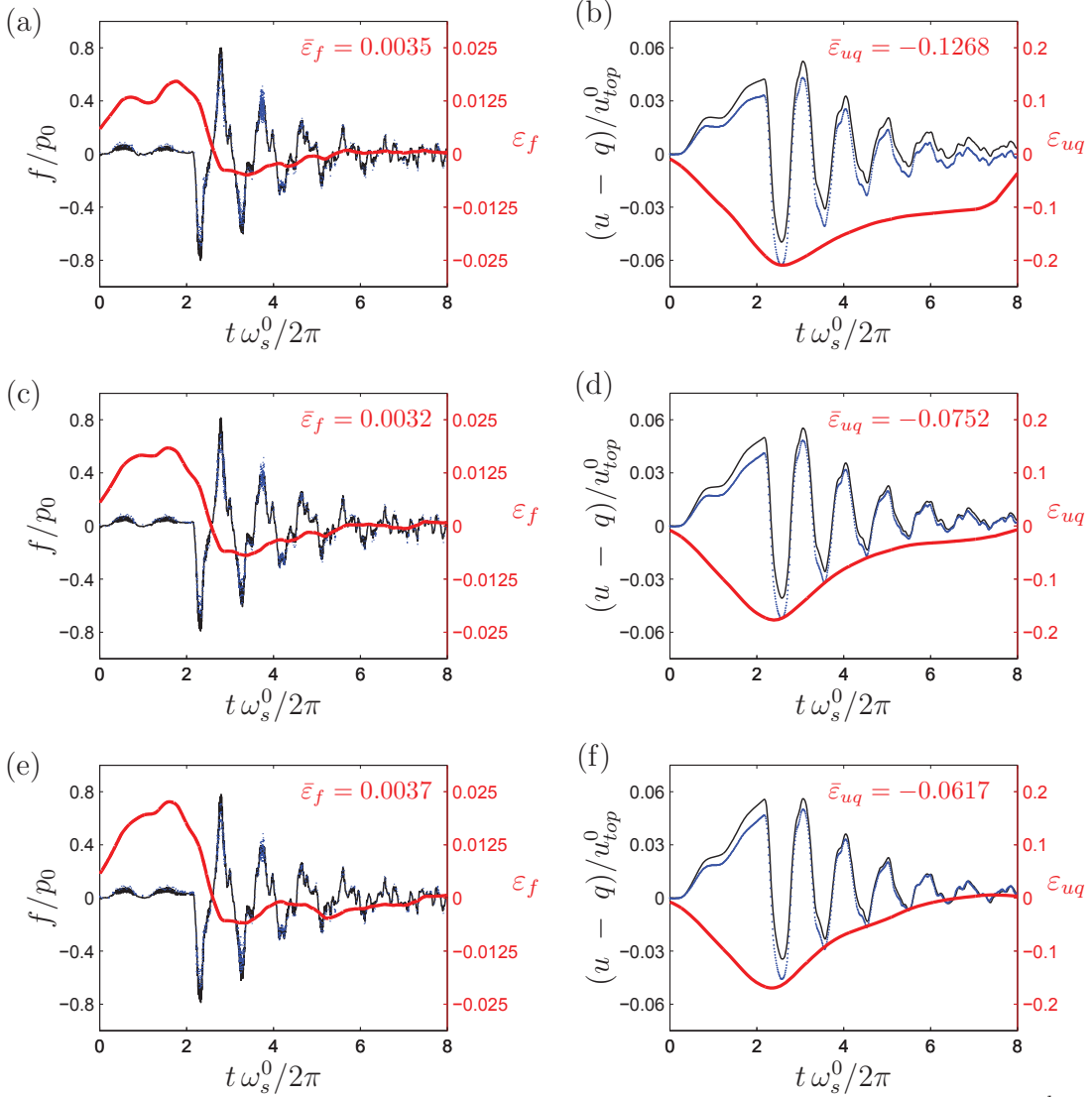


FIGURE 5.4. Measured damper force  $f_e^m$  ( $\cdot\cdot$ ) compared with desired damper force  $f_e^d$  ( $-$ ) and desired damper displacement  $u - q_d$  ( $\cdot\cdot$ ) compared with numerical damper displacement ( $-$ ) for filtered IFF controller with  $\nu = -2.0$  and  $\omega_q = \omega_s/20$  (a,b),  $\omega_s/8$  (c,d) and  $\omega_s/5$  (e,f), respectively. Error measure for damper force  $\varepsilon_f$  and damper displacement  $\varepsilon_{uq}$  given by ( $-$ ).

*5.2.2. Damping performance*

In this section the damping performance of the physical model of the hybrid viscous damper is illustrated. The displacement response  $u_{top}$  of the shear frame top floor is shown in Fig. 5.5. The displacement from the RTHS is compared with the numerical simulation results obtained by direct time integration for  $\eta = 0$ . The results are computed for  $\nu = 0.0, -2.0$  and  $-4.0$  and with  $\omega_q = \omega_s/8$ , whereby the numerical results presented in the present section differs from the numerical results presented in Section 3.3.2 for  $\omega_q = 0$ .

In general good agreement between the experimental results and the numerical results is observed, and as illustrated by the dashed exponential decay curves the experimental results verify that for  $\nu < 0$  the apparent damping increases when the magnitude  $|\nu|$  increases. As in Section 3.3.2 the damping ratio is estimated by the logarithmic decrement evaluated between both the first and the fourth maximum and minimum in the free vibration response. The estimated damping ratios are compared in Table 5.1. For  $\eta = 0$  damping is seen to be reduced for a non-zero value of the corner frequency  $\omega_q = \omega_s/8$ , and the deterioration in damping performance becomes more pronounced for increasing magnitude of negative  $\nu$ ,  $-8\% \rightarrow -13\%$ . Thus, it is important to choose  $\omega_q$  sufficiently large to avoid damper drift, however without deteriorating the performance of the hybrid damper. Comparing the RTHS results with the corresponding numerical results for  $\omega_q = \omega_s/8$ , only a minor decrease in damping performance is observed. The decrease in damping also seems to be somewhat independent of the magnitude of the gain value  $\nu$ , and may instead be attributed to the performance of the bang-bang control as mentioned in Section 5.2.1. The rather small deviations between the results obtained by the direct time integration and by the hybrid simulation shows that the performance of the hybrid viscous damper is relatively robust with respect to errors in the force tracking.

*5.3. RTHS with offshore wind turbine and IFF controller*

In this section results from the RTHS with the hybrid viscous damper installed in an offshore wind turbine using the experimental setup as described in Section 5.1.2 are presented. The actuator displacement is regulated by an IFF controller for increased damper displacement as described in Section 3.4. A mixing parameter

TABLE 5.1. Damping ratio  $\zeta$  estimated from free vibration response

		$\nu = 0$	$\nu = -2$	$\nu = -4$
Num.	$(\eta = 0), \omega_q = 0$	0.053	0.086	0.108
Num.	$(\eta = 0), \omega_q = \omega_s/8$	0.053	0.093 - 8 %	0.124 - 13 %
RTHS	$(\eta = 0.5), \omega_q = \omega_s/8$	0.051 - 4 %	0.082 - 5 %	0.106 - 2 %

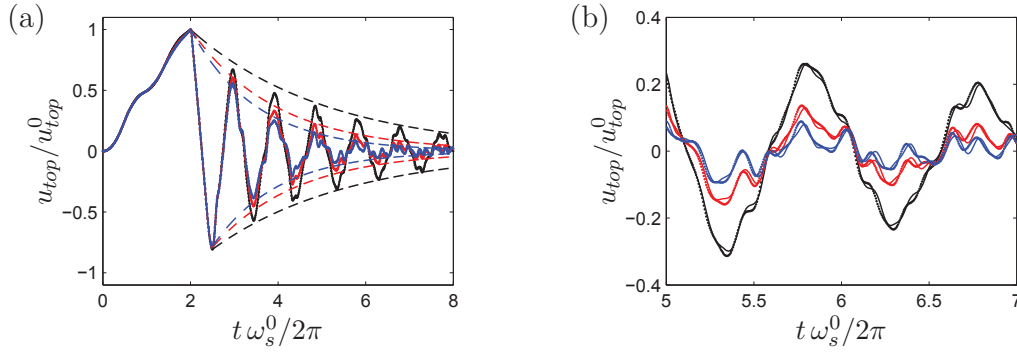


FIGURE 5.5. Top-floor response by numerical simulation for  $\nu = 0.0$  (—),  $-2.0$  (---) and  $-4.0$  (---) and by RTHS for  $\nu = 0.0$  (· ·),  $-2.0$  (· ·) and  $-4.0$  (· ·) and with  $\omega_q = \omega_s/8$ .

of  $\eta = 0.1$  is used in the RTHS, whereby 10 % of the total damper force in the simulation is from the experimental substructure. The experimental results are compared with pure numerical results, corresponding to  $\eta = 0$ .

### 5.3.1. Actuator drift and filter parameters

The performance of the second order filter in eq. (3.14) in terms of reducing drift is investigated by comparing the measured damper force  $f_e^d$  of the MR damper with the desired damper force  $f_e^d$ , and by comparing the desired damper displacement  $u - q_d$  with the corresponding displacement obtained by direct time integration for  $\eta = 0$ . The results are presented for  $\nu = 0.5$  in Fig. 5.6(a-d) and for  $\nu = 0.75$  in Fig. 5.6(e-h). The curves in Fig. 5.6(a,b) and Fig. 5.6(e,f) are obtained with filter frequency  $\omega_f = \tau_f \omega_s^2 = \omega_s/8$ , while in Fig. 5.6(c,d) and Fig. 5.6(g,h) the frequency is  $\omega_f = \tau_f \omega_s^2 = \omega_s/5$ . The small deviation between the desired and measured damper force, which mainly occur around the maxima and minima, is again attributed to the limited force tracking capabilities of the bang-bang control. The associated difference in damper displacement is seen to be somewhat larger than for the force tracking error, but with less irregularities. The latter can be ascribed to the integration in eq. (3.14), which acts as a low pass filter. When comparing the desired damper displacement ( $u - q_d$ ) for  $\nu = 0.5$  in Fig. 5.6(c,d) and for  $\nu = 0.75$  in Fig. 5.6(f,h) it is found that the damper amplitude is approximately doubled, which agrees with the theoretical result in eq. (3.13).

The red solid curves in figures 5.6 show the relative force tracking error. A comparison of the mean force tracking errors  $\bar{\varepsilon}_f$  and  $\bar{\varepsilon}_{uq}$  gives an indication of the influence of the choice of filter frequency  $\omega_f$ . For  $\nu = 0.5$  the error ratios are  $\bar{\varepsilon}_{uq}/\bar{\varepsilon}_f \simeq 5$  and 2.7 for  $\omega_f = \tau_f \omega_s^2 = \omega_s/8$  and  $\omega_s/5$ , respectively, while for  $\nu = 0.75$  they are  $\bar{\varepsilon}_{uq}/\bar{\varepsilon}_f \simeq 6.3$  and 3.9. The apparent inverse proportionality between the error ratio and the corresponding magnitude of the filter frequency  $\omega_f$  indicates that the drift can be effectively reduced by increasing the value of  $\omega_f = \tau_f \omega_s^2$ , while the drift in the actuator seems to increase with the magnitude of the gain parameter  $\nu$ .

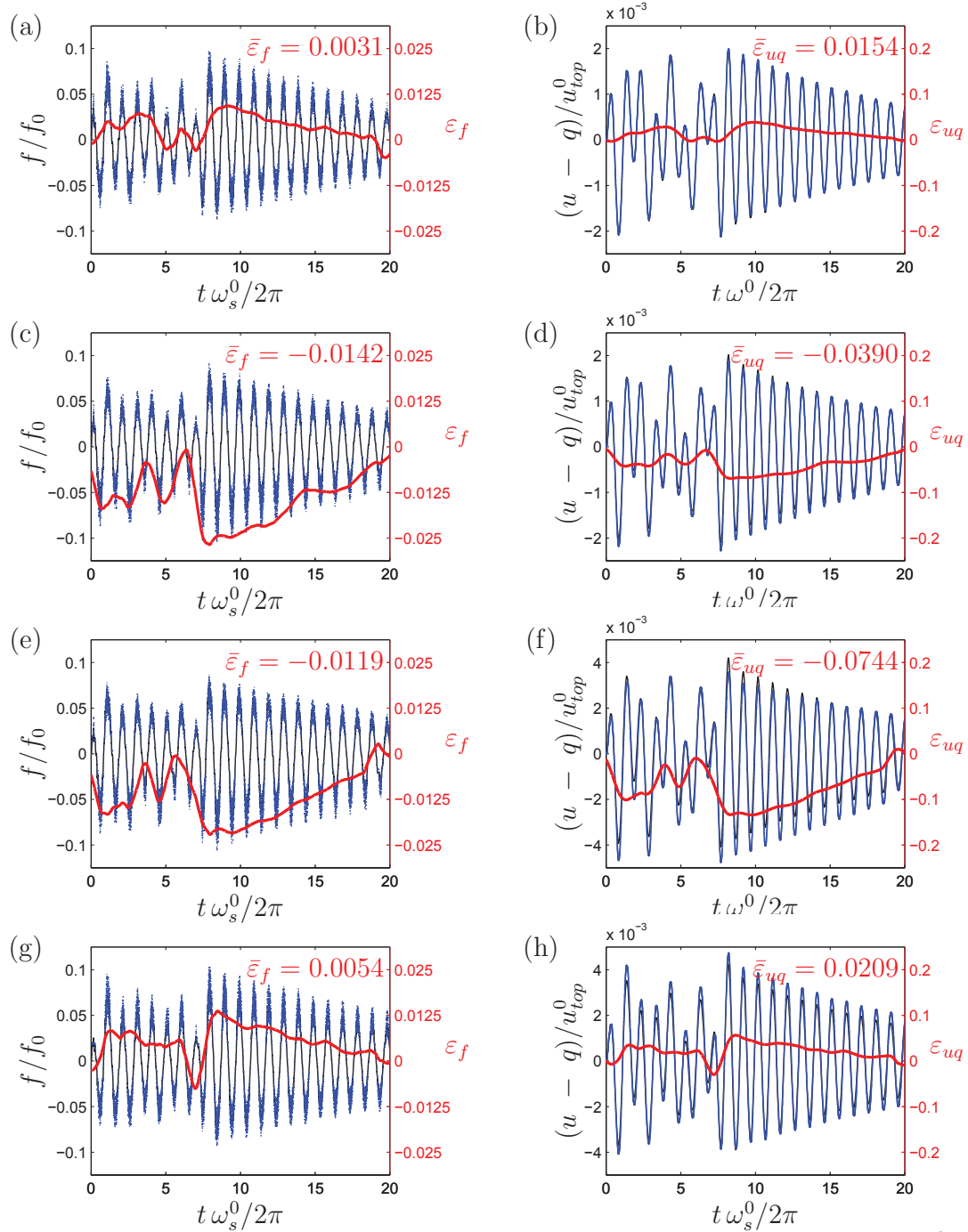


FIGURE 5.6. Measured damper force  $f_e^m$  ( $\cdot \cdot$ ) compared with desired damper force  $f_e^d$  ( $-$ ) and desired damper displacement  $u - q_d$  ( $\cdot \cdot$ ) compared with numerical damper displacement ( $-$ ). Results are shown for  $\nu = 0.5$  and  $\omega_f = \tau_f \omega_s^2 = \omega_s/8$  in (a)-(b) and with  $\omega_s/8$  in (c)-(d), and for  $\nu = 0.75$  with  $\omega_f = \tau_f \omega_s^2 = \omega_s/8$  in (e)-(f) and with  $\omega_s/5$  in (g)-(h). Error measure for damper force  $\varepsilon_f$  and damper displacement  $\varepsilon_{uq}$  given by ( $-$ ).

### Damping performance

The displacement of the wind turbine tower top is seen in Fig. 5.7 for gain value  $\nu = 0.75$ . The corner frequency is chosen as  $\omega_f = \tau_f \omega_s^2 = \omega_s/5$ , which is slightly higher than for the numerical simulations in 3.5.1. The experimental and numerical results are seen to match very well, and the damping performance appears to be almost identical for the RTHS and the corresponding numerical simulation. The critical damping ratios are estimated from the logarithmic decrement, and the exponentially decaying curves are seen to match almost exactly the corresponding decay in vibration amplitude. The average damping ratio is  $\zeta_{ss,num} = 0.0128$  for the numerical simulation, while  $\zeta_{ss,exp} = 0.0127$  is obtained from the RTHS results. Thus, the deviation between the two results is less than 1%, and also similar to the estimated attainable damping  $\zeta_{ss,max} = 0.0128$  for a pure viscous dash-pot in Section 2.3.1. The small reduction in damping ratio observed in the RTHS is most likely due to the bang-bang control and the non-viscous behavior of the MR damper. The results seem very promising, but it should be emphasised that a larger value of the mixing parameter  $\eta > 0.1$  might lead to additional inaccuracies and consequently reduced performance of the RTHS.

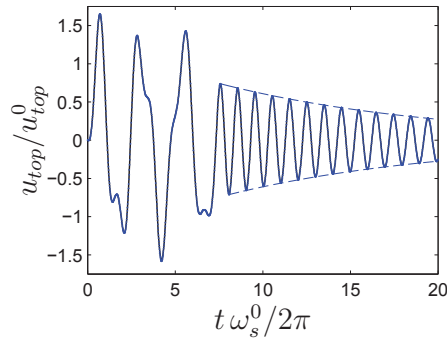


FIGURE 5.7. Top tower displacement as computed in the numerical substructure ( $\cdot \cdot$ ), and as computed by a numerical simulation ( $-$ ) for (a)  $\nu = 0.5$  and (b)  $\nu = 0.75$  with  $\omega_f = \tau_f \omega_s^2 = \omega_s/5$ .

## 6. CONCLUSION

In this thesis a number of novel strategies for damping of the two lowest critical tower modes of a fixed offshore wind turbine are presented. Tuned Mass Dampers (TMD) are employed already today in offshore wind turbines. Effective damping by a TMD is however associated with additional damper mass at the top of the wind turbine, which is highly undesirable. A common aim behind the damper concepts presented in this thesis is therefore to introduce sufficiently additional damping to the critical tower modes, without adding significant mass at the top of the wind turbine.

In [P1] it is demonstrated how the feasibility of installing passive damper at the bottom of the tower can be increased by installing dampers in a stroke amplifying brace. A toggle brace design is presented that amplifies the relative displacement of the tower to a larger displacement over the damper for the two lowest tower modes, and it is demonstrated how a symmetric configuration of viscous dash-pots can be tuned with the same viscous damping coefficient for optimal damping of both of the two lowest tower modes independent of the rotor orientation. The idea of implementing dampers at the bottom of the tower is also the main topic in [P2]. Here a hybrid viscous damper controlled by an Integral Force Feedback (IFF) is applied to increase the displacement of the tower to a larger displacement over the viscous dash-pot. With the hybrid viscous damper it is further demonstrated through numerical simulations in [P2] that optimum tuned dampers installed at the bottom of the tower can significantly reduce the fatigue damage in the monopile support structure. The hybrid viscous damper is however prone to drift in the actuator displacement, as illustrated through a series of Real Time Hybrid Simulations presented in [P4]. With a filtered integration appropriately tuned to the critical modes of the wind turbine, this drift can be reduced without a significant reduction in the damper performance.

Another approach for introducing sufficient damping to the critical tower modes for a reduced damper mass is by an Active Tuned Mass Damper (ATMD), as demonstrated in [P3]. A novel control strategy is proposed based on feedback from the wind turbine displacement and the relative velocity of the damper mass. By numerical simulations it is demonstrated that the performance of the ATMD towards harmonic loading is equivalent to that of the passive TMD, but with a significantly reduced damper mass. Another important feature of the proposed

control strategy is the reduced control force, realised by equating the control signal proportional to the wind turbine displacement with the control signal proportional to relative velocity.

A last topic of the thesis is the hybrid viscous damper with filtered IFF control for increased damping performance as presented in [A3] and [P4]. The filtered IFF control is seen to lead to increased attainable damping. The format is however also prone to drift in the actuator signal as demonstrated by the RTHS in [P4]. The drift can however be reduced by a dedicated filtering of the actuator velocity, which unfortunately is seen to reduce the damping performance of the hybrid viscous damper.

## BIBLIOGRAPHY

- [1] hawc2.dk. <http://http://www.hawc2.dk>.
- [2] S. Ankireddi and H.T.Y. Yang. Simple ATMD control methodology for tall buildings subject to wind loads. *Journal of Structural Engineering*, **122**(1):83–91, 1996.
- [3] Y. Cha, J. Zhang, A.K. Agrawal, B. Dong, A. Friedman, S.J. Dyke, and J. Ricles. Comparative studies of semiactive control strategies for MR dampers: pure simulation and real-time hybrid tests. *Journal of Structural Engineering*, **139**(7):1237–1248, 2013.
- [4] C.C. Chang and H.T.Y. Yang. Control of buildings using active tuned mass dampers. *Journal of engineering mechanics*, **121**(3):355–366, 1995.
- [5] J.C.H. Chang and T.T. Soong. Structural control using active tuned mass dampers. *Journal of the Engineering Mechanics Division*, **106**(6):1091–1098, 1980.
- [6] R. Christenson, Y.Z. Lin, A. Emmons, and B. Bass. Large-scale experimental verification of semiactive control through real-time hybrid simulation 1. *Journal of Structural Engineering*, **134**(4):522–534, 2008.
- [7] R. Collins, B. Basu, and B.M. Broderick. Vibration control of wind turbine towers using active and semi-active tuned mass dampers. In *International Solar Energy Society UK Section-Conference-C*, volume 85 95, 2006.
- [8] S. Colwell and B. Basu. Tuned liquid column dampers in offshore wind turbines for structural control. *Engineering Structures*, **31**(2):358–368, 2009.
- [9] M.C. Constantinou, P. Tsopelas, W. Hammel, and A.N. Sigaher. Toggle-brace-damper seismic energy dissipation systems. *Journal of Structural Engineering*, **127**(2):105–112, 2001.
- [10] M. Damgaard, L.B. Ibsen, L.V. Andersen, and J.K.F. Andersen. Cross-wind modal properties of offshore wind turbines identified by full scale testing. *Journal of Wind Engineering and Industrial Aerodynamics*, **116**:94–108, 2013.

- [11] J.P. Den Hartog. Mechanical vibrations, 1956. (Reprinted by Dover, New York, 1985).
- [12] C. Devriendt, P.J. Jordaens, G. De Sitter, and P. Guillaume. Damping estimation of an offshore wind turbine on a monopile foundation. *IET Renewable Power Generation*, **7**(4):401–412, 2013.
- [13] DNV. DNV offshore standard dnv-os-j101, design of offshore wind turbine. *Technical Standard* 134–135, 2013.
- [14] I. Enevoldsen and K.J. Mork. Effects of a vibration mass damper in a wind turbine tower. *Mechanics of Structures and Machines*, **24**(2):155–187, 1996.
- [15] EWEA. The european offshore wind industry - key trends and statistics 2014. Technical report, European Wind Energy Association, 2015. Available at: <<http://www.ewea.org/>> (accessed in February 2015).
- [16] A.M. Hansen and T.J. Larsen. Gear dynamics. Technical report, Risoe National Lab., 2009. Research in Aeroelasticity EFP-2007-II, Risoe-R-1698(EN):134–142.
- [17] M.H. Hansen. Aeroelastic stability analysis of wind turbines using an eigenvalue approach. *Wind Energy*, **7**(2):133–143, 2004.
- [18] J. Høgsberg and M.L. Brodersen. Hybrid viscous damper with filtered integral force feedback control. *Journal of Vibration and Control*.
- [19] J.R. Høgsberg and S. Krenk. Linear control strategies for damping of flexible structures. *Journal of Sound and Vibration*, **293**(1-2):59–77, 2006.
- [20] G.W. Housner, L.A. Bergman, T.K. Caughey, A.G. Chassiakos, R.O. Claus, S.F. Masri, R.E. Skelton, T.T. Soong, B.F. Spencer, and J.T.P. Yao. Structural control: Past, present, and future. *Journal of Engineering Mechanics*, **123**(9):897–971, 1997.
- [21] Y. Ikeda. Active and semi-active vibration control of buildings in Japan: Practical applications and verification. *Structural Control and Health Monitoring*, **16**(7-8):703–723, 2009.
- [22] J. Jonkman and W. Musial. Offshore Code Comparison Collaboration (OC3) for IEA task 23 offshore wind technology and deployment. Technical report, National Renewable Energy Laboratory, 2010. Technical Report NREL/TP-5000-48191.
- [23] J.M. Jonkman, S. Butterfield, W. Musial, and G. Scott. Definition of a 5-MW reference wind turbine for offshore system development, 2009. Technical Report NREL/TP-500-38060.

- [24] J.K. Kaldellis and M. Kapsali. Shifting towards offshore wind energy - recent activity and future development. *Energy Policy*, **53**:136–148, 2013.
- [25] S. Krenk. Frequency analysis of the tuned mass damper. *Journal of applied mechanics*, **72**(6):936–942, 2005.
- [26] T. J. Larsen and A. M. Hansen. *How 2 HAWC2, the user's manual*. Risø National Laboratory, 2007.
- [27] H. O. Madsen, S. Krenk, and N. C. Lind. *Methods of Structural Safety*. Dover Publications, New York, 2006.
- [28] J.A. Main and S. Krenk. Efficiency and tuning of viscous dampers on discrete systems. *Journal of Sound and Vibration*, **286**(1-2):97–122, 2005.
- [29] P.J. Murtagh, A. Ghosh, B. Basu, and B.M. Broderick. Passive control of wind turbine vibrations including blade/tower interaction and rotationally sampled turbulence. *Wind Energy*, **11**(4):305–317, 2008.
- [30] I. Nishimura, T. Kobori, M. Sakamoto, N. Koshika, K. Sasaki, and S. Ohru. Active tuned mass damper. *Smart Materials and Structures*, **1**(4):306, 1992.
- [31] G. Ou, M. L. Brodersen, and S. Dyke. Real time hybrid simulations case study: Vibration reduction of offshore wind turbine using hybrid controlled damper. (to be published).
- [32] G. Ou, A. I. Ozdagli, S. J. Dyke, and B. Wu. Robust integrated actuator control: Experimental verification and real-time hybrid-simulation implementation. *Earthquake Engineering & Structural Dynamics*, **44**(3):441–460, 2015.
- [33] A. Preumont and Y. Achkire. Active damping of structures with guy cables. *Journal of guidance, control, and dynamics*, **20**(2):320–326, 1997.
- [34] A. Preumont, J.P. Dufour, and C. Malekian. Active damping by a local force feedback with piezoelectric actuators. *Journal of guidance, control, and dynamics*, **15**(2):390–395, 1992.
- [35] F. Ricciardelli, A. D. Pizzimenti, and M. Mattei. Passive and active mass damper control of the response of tall buildings to wind gustiness. *Engineering structures*, **25**(9):1199–1209, 2003.
- [36] A.T. Rodriguez, C.E. Carcangiu, I. Pineda, T. Fischer, B. Kuhnle, M. Scheu, and M. Martin. Wind turbine structural damping control for tower load reduction. In *Civil Engineering Topics, Volume 4* 141–153. 2011.
- [37] T. E. Saeed, G. Nikolakopoulos, J. Jonasson, and H. Hedlund. A state-of-the-art review of structural control systems. *Journal of Vibration and Control*, 2013.

- [38] R. Shirzadeh, C. Devriendt, M. A. Bidakhvidi, and P. Guillaume. Experimental and computational damping estimation of an offshore wind turbine on a monopile foundation. *Journal of Wind Engineering and Industrial Aerodynamics*, **120**:96–106, 2013.
- [39] A.N. Sigaher and M.C. Constantinou. Scissor-jack-damper energy dissipation system. *Earthquake Spectra*, **19**(1):133–158, 2003.
- [40] J. R. Sladek and R. E. Klingner. Effect of tuned-mass dampers on seismic response. *Journal of Structural Engineering*, **109**(8):2004–2009, 1983.
- [41] T.T. Soong and B.F. Spencer. Supplemental energy dissipation: State-of-the-art and state-of-the-practice. *Engineering Structures*, **24**(3):243–259, 2002.
- [42] B.F. Spencer Jr and S. Nagarajaiah. State of the art of structural control. *Journal of structural engineering*, **129**(7):845–856, 2003.
- [43] B.F. Spencer Jr and M. K. Sain. Controlling buildings: A new frontier in feedback. *Control Systems, IEEE*, **17**(6):19–35, 1997.
- [44] G. M. Stewart and M. A. Lackner. The impact of passive tuned mass dampers and wind–wave misalignment on offshore wind turbine loads. *Engineering Structures*, **73**:54–61, 2014.
- [45] N.J. Tarp-Johansen, L. Andersen, E.D. Christensen, C. Mørch, S. Frandsen, and B. Kallesøe. Comparing sources of damping of cross-wind motion. In *Proceedings of the European Wind Energy Conference & Exhibition*, Stockholm, Sweden, 2009.
- [46] Y.L. Xu, B. Samali, and K.C.S. Kwok. Control of along-wind response of structures by mass and liquid dampers. *Journal of Engineering Mechanics*, **118**(1):20–39, 1992.

# P1

Damping of offshore wind turbine tower vibrations  
by a stroke amplifying brace

Mark L. Brodersen, Jan Høgsberg

*Energy Procedia*,  
Vol **53**:258–267, 2014.



EERA DeepWind'2014, 11th Deep Sea Offshore Wind R&D Conference

## Damping of offshore wind turbine tower vibrations by a stroke amplifying brace

Mark L. Brodersen, Jan Høgsberg

*Department of Mechanical Engineering, Technical University of Denmark, DK-2800 Lyngby, Denmark*

---

### Abstract

The potential of installing dampers inside the tower of an offshore wind turbine is investigated through simulations. Dampers are installed at the bottom to act on the curvature of the tower, and it is shown that dampers installed in suitable braces have the potential to increase the critical damping ratio of the two lowest tower modes by 1 percent. By using a toggle-brace system, damper stroke is increased, while the damper force is reduced. Finally, by installing the dampers in a symmetric configuration, tuning for maximum damping is approximately independent of the orientation of the rotor, thereby making this installation of dampers feasible.

© 2014 Elsevier Ltd. This is an open access article under the CC BY-NC-ND license

(<http://creativecommons.org/licenses/by-nc-nd/3.0/>).

Selection and peer-review under responsibility of SINTEF Energi AS

**Keywords:** Stroke amplifying toggle brace, Passive damping, Fixed offshore wind turbine

---

### Introduction

Design of monopile support structures for large offshore wind turbines, as the wind turbine illustrated in figure 1, is usually driven by fatigue. Due to the relatively low inherent damping of cross-wind tower vibrations, the fatigue lifespan is significantly influenced by cross-wind vibrations caused by wave loading misaligned with the wind [1]. In the future larger offshore wind turbines will be operating at larger water depths, whereby the critical tower frequency will be lowered and potentially approach the excitation frequency of the waves. This may cause fatigue damage due to wave loading to increase significantly, whereby the monopile support structure may reach its limit of structural feasibility. A way to extend the feasibility of the monopile support structure is by means of structural control, in which external devices are installed in order to reduce the dynamic response.

For structural control of fixed offshore wind turbines, resonant damping is the concept most widely used by the industry [1], and it is also the damping concept that has received the most attention in the literature. Installation of a resonant damper like a Tuned Liquid Damper (TLD) or a Tuned Mass Damper (TMD) have been shown to lead to a reduction of the fatigue damage accumulated in the monopile of an offshore wind turbine [2,3]. In order to be effective

---

\* Corresponding author. Tel.: +45 4525 1377 ; fax: +45 4588 4325.

*E-mail address:* [mlai@mek.dtu.dk](mailto:mlai@mek.dtu.dk)

a resonant damper like a TMD should be installed where the absolute motion of the targeted vibration mode is large, which is at the top of the tower or inside the nacelle. However, with a TMD efficient damping is associated with large damper motion and large damper mass, which is highly undesirable and maybe even unfeasible at the top of a slender wind turbine tower. In order to avoid these installation issues, a concept with semi-active dampers installed in a stroke amplifying toggle-brace-damper system inside the tower has been proposed by Fischer et al. [4]. The brace is installed in order to amplify the horizontal relative motion of the tower walls to a larger displacement of the damper. A toggle-brace system is a well known concept for application in shear frames [5], where it is used to amplify the horizontal drift of the frame to a larger displacement over the damper. This has been proven to enhance the energy dissipation of a damper installed in a shear frame, when compared to the same damper installed using a traditional diagonal brace [6]. Likewise, the present paper considers installation of passive dampers to act on the relative motion of the tower, though using a more realistic model for the tower wall deflection, that takes into account both horizontal and vertical displacements of the tower walls.

A passive damper is by definition collocated, which means that the two concepts of controllability and observability fuse together. In this paper the two concepts are represented in the term 'modal connectivity'. Critical for the effective implementation of passive dampers inside the tower is sufficient damper stroke and sufficient attainable damping, both related to modal connectivity. The damper stroke is represented by the displacement of the damper with respect to the targeted vibration form, while attainable damping is associated with the ability of the damper to change the natural frequency of the structure when the damper is locked [7]. Vibrations of the tower are dominated by a combination of the two lowest tower modes, fore-aft mode and side-to-side mode, as seen in figure 2 and figure 3, respectively. This means that both modes need to be addressed. In the two modes the tower is primarily deformed in bending, while rotor, nacelle and blades act as lumped inertia at the free end of the tower. Modal connectivity is maximized, by positioning the dampers at the bottom of the tower, where the curvature associated with bending is largest. Although the modal connectivity is maximized, the displacement of the damper is likely to be small, thereby making installation of passive dampers inside the tower unfeasible. In order to increase the displacement of the damper and thereby the feasibility of installing passive dampers inside the tower, a toggle-brace-damper concept is introduced. The toggle-brace concept amplifies the relative displacement of the tower to a larger displacement of the damper, whereby at the same time the damper force is decreased.

Another important aspect of installing passive dampers inside the tower is the relative circumferential positioning of the dampers. Since the wind turbine rotor can turn relative to the tower, dampers should be positioned in a layout so that damping is independent of the position of the rotor. In this paper it will be demonstrated that equally tuned dampers can be positioned in a circumferential symmetric layout, so that the damping ratio of the two lowest tower modes remain approximately constant with respect to the orientation of the rotor.

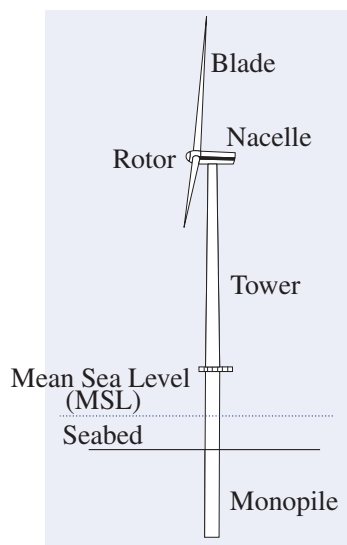


Fig. 1. Offshore wind turbine

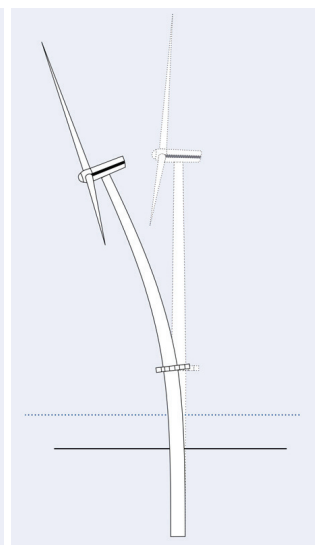


Fig. 2. Fore-aft mode

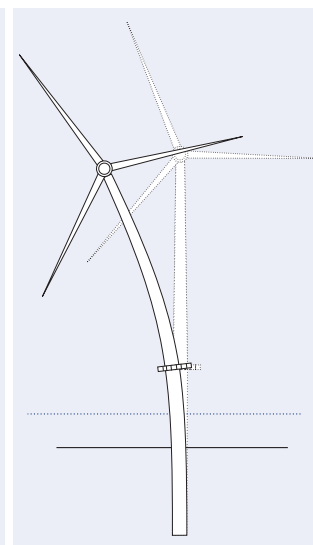


Fig. 3. Side-to-side mode

## Modelling of wind turbine with brace damper concept

Due to the slender geometry of the tower and blades, the structural dynamics of a wind turbine is commonly described using a non-linear numerical beam model. For a simple assessment of the influence of the brace damper system a linear model is however convenient. A simple linear beam model is obtained by assuming the wind turbine to be at standstill, by representing the inertia of the rotor, nacelle and blades as lumped inertia at the top of the tower and by modeling the flexible foundation of the soil using a linear Winkler type spring model.

The beam model, as illustrated in figure 4, is defined with the global  $y$ -axis in the direction of the rotor, the global  $x$ -axis in the direction perpendicular to the rotor, and the global  $z$ -axis in the vertical tower direction. A part of the beam model from node  $n$  to node  $n + 2$  is illustrated in figure 5. Each node in the beam model carries six degrees of freedom (dofs), three translations  $\mathbf{u}_n^T = [u_x, u_y, u_z]$  and three rotations  $\boldsymbol{\varphi}_n^T = [\varphi_x, \varphi_y, \varphi_z]$  all defined with respect to the global coordinate system of the beam model. The discretized equations of motion are given in terms of the nodal displacement vector  $\mathbf{u}$  as

$$\mathbf{M}\ddot{\mathbf{u}} + \mathbf{C}\dot{\mathbf{u}} + \mathbf{K}\mathbf{u} = \mathbf{f}_d + \mathbf{f}_{ext}, \quad (1)$$

where  $\mathbf{M}$  is the mass matrix,  $\mathbf{K}$  is the stiffness matrix,  $\mathbf{C} = \alpha\mathbf{M} + \beta\mathbf{K}$  is a proportional damping matrix to represent structural damping,  $\mathbf{f}_d$  is the nodal load vector due to external dampers, and  $\mathbf{f}_{ext}$  is the generalized forces associated with external loads due to wind and waves. The stiffness matrix  $\mathbf{K} = \mathbf{K}_e + \mathbf{K}_s$  consist of two parts: The usual constitutive elastic stiffness matrix  $\mathbf{K}_e$  and the stiffness matrix for the elastic foundation  $\mathbf{K}_s$ .  $\mathbf{K}_e$  is based on the complementary energy principle following Krenk [8], whereby both extension, bending, shear and torsion deformations are included in the element formulation. The specific implementation of the element stiffness matrix follows Svendsen [9].

### Damper implementation

Two different implementations of dampers are considered. The first implementation, with two dampers installed on opposite walls of the tower to act directly on the curvature of the tower, is shown in figure 6(a). In this paper this implementation is referred to as a curvature-brace. In the figure  $\theta_2$  describes the angle between the tower wall and the horizontal direction and  $\theta_3$  describes the circumferential angle between the global  $x$ -axis and the direction of the damper, which will change as the position of the rotor relative to the tower changes. When  $\theta_3 = 0^\circ$  and  $\theta_3 = 180^\circ$  the damper will only influence the side-to-side mode, while when  $\theta_3 = 90^\circ$  and  $\theta_3 = 270^\circ$  the damper will only influence the fore-aft mode. Figure 6(b) shows several braces installed in a homogeneously distributed circumferential layout with  $60^\circ$  between the orientation of each damper, in order for the combined curvature-brace system to be able to damp vibrations in any direction.

In spite of a large modal connectivity, the feasibility of a curvature-brace system is limited by the relatively small displacement over the dampers. To overcome this and thereby improve the feasibility, another implementation is considered, where dampers are installed in a curvature-toggle-brace, as shown in figure 6(c). Compared to the curvature-brace, the relative displacement of the tower is amplified to a larger displacement over the damper, by the use of a toggle mechanism. Attainable damping for the curvature-toggle-brace is expected to be the same as for the curvature brace. At one end the damper is connected to the toggle mechanism, while at the other end the damper is connected to a joint, which must be kept at the centerline of the tower cross section by e.g. a number of additional supporting braces. The geometry of the toggle-brace is described entirely in terms of the angle  $\theta_1$  between the brace and the tower wall, the angles  $\theta_2$  and  $\theta_3$ , and the radius  $r$  of the tower. Minimizing  $\theta_1$  will maximize the amplification of the toggle brace, while the distance of the toggle joint to the tower wall should be large enough to avoid snap-through during operational conditions. In this paper the angle is fixed at  $\theta_1 = 5^\circ$ . Figure 6(d) shows several braces in a curvature-toggle-brace system installed in a homogeneously distributed circumferential layout, with  $60^\circ$  between each damper.

### Connectivity vector

The influence of installing a damper in the wind turbine tower is in the beam model described by its connectivity vector  $\mathbf{w}$  and the magnitude of the damper force  $f_d$ , whereby the force vector is given as

$$\mathbf{f}_d = -\mathbf{w}f_d \quad (2)$$

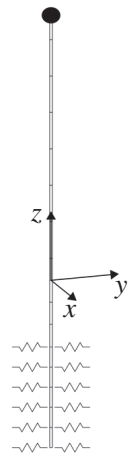


Fig. 4. Beam model

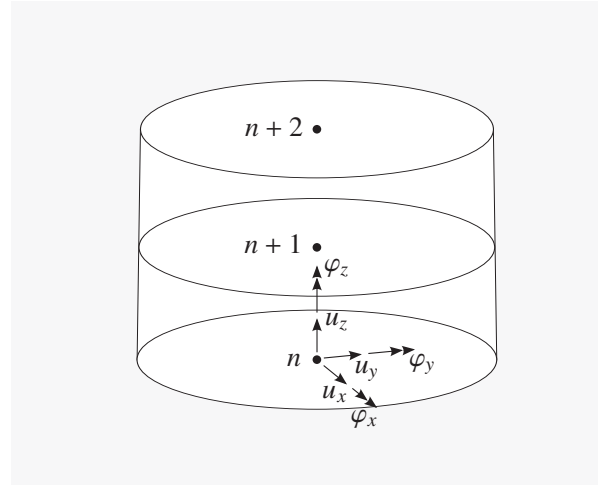
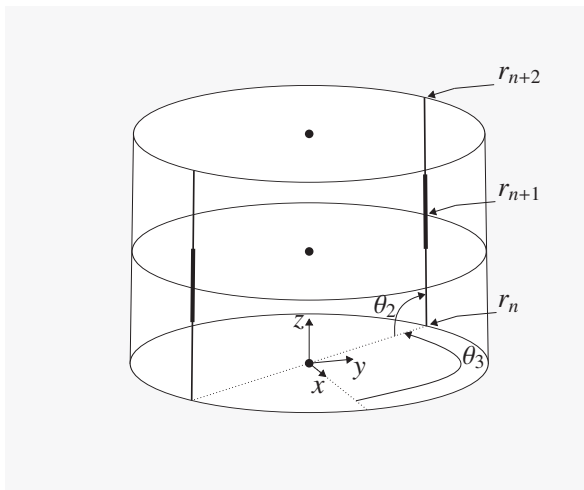
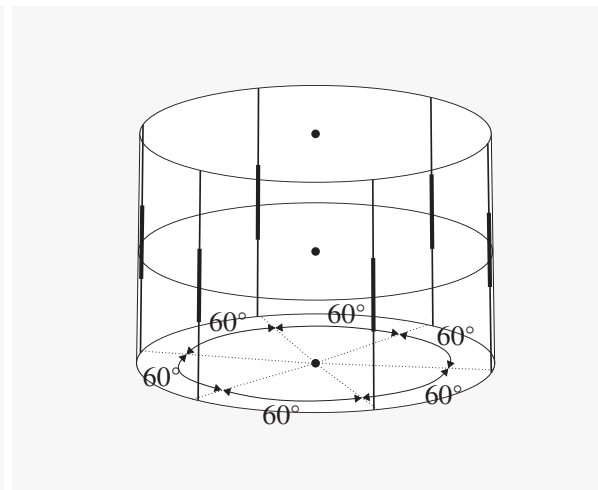


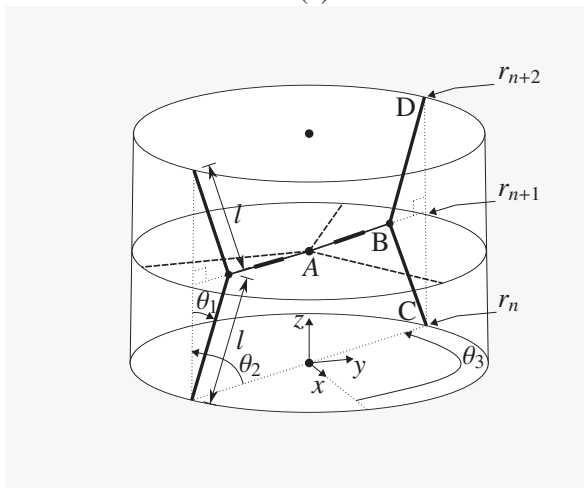
Fig. 5. Section of beam model



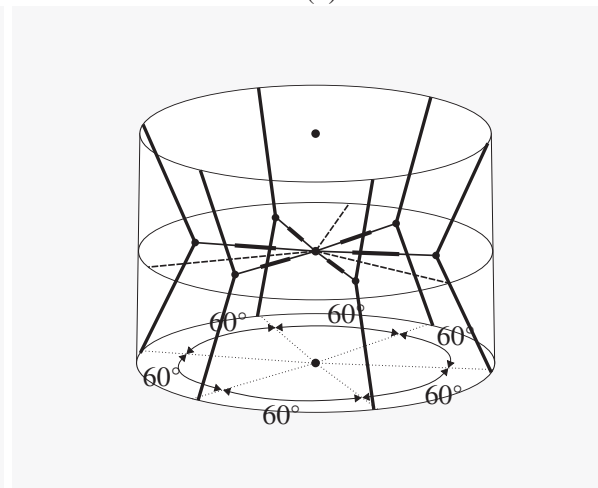
(a)



(b)



(c)



(d)

Fig. 6. (a) Curvature brace, (b) Curvature brace system, (c) Curvature toggle brace and (d) Curvature toggle brace system

The connectivity vector  $\mathbf{w}$  transforms the forces and moments imposed by the damper on the tower into equivalent nodal forces in the beam model. In this sense  $\mathbf{w}$  describes the connection of the damper to the tower structure through the brace mechanism, whereby in this context it may be seen as an extension of the magnification factor used for design of toggle-brace concepts in shear frames [5]. If the damper and connectivity vector are both assumed to operate linearly, the displacement of the damper  $u_d$  is given by

$$u_d = \mathbf{w}^T \mathbf{u} \tag{3}$$

Equation (3) implies that the brace members are rigid. The connectivity vector is determined by computing the nodal load vector imposed by the brace-damper system on the beam model representing the tower, with each damper considered separately. When the toggle-brace is connected to the tower centerline, it results in apparent nodal forces, whereas when the brace is connected to the tower wall, it leads to nodal forces as well as nodal moments.

As an example, consider the damper associated with member  $AB$  in figure 6(c). Each member of the brace acts as a bar, only allowing axial bar forces. The bar force  $N_{AB}$  in member  $AB$  is directly given as the damper force  $f_d$ , and due to symmetry, the bar force in member  $BC$ ,  $N_{BC}$ , equals the bar force in member  $BD$ ,  $N_{BD}$ , whereby force equilibrium of joint B gives

$$N_{BC} = N_{BD} = \frac{1}{2} \frac{f_d}{\sin \theta_1} \tag{4}$$

When assuming  $\cos \theta_1 \approx 1$ , the nodal load vectors for the nodes  $n, n + 1$  and  $n + 2$  follow as

$$\mathbf{f}_{d,n} = \begin{bmatrix} -\frac{1}{2} \cos \theta_3 \left( \frac{\cos \theta_2}{\sin \theta_1} + \sin \theta_2 \right) \\ -\frac{1}{2} \sin \theta_3 \left( \frac{\cos \theta_2}{\sin \theta_1} + \sin \theta_2 \right) \\ \frac{1}{2} \left( \frac{\sin \theta_2}{\sin \theta_1} - \cos \theta_2 \right) \\ \frac{1}{2} r_n \sin \theta_3 \left( \frac{\sin \theta_2}{\sin \theta_1} - \cos \theta_2 \right) \\ -\frac{1}{2} r_n \cos \theta_3 \left( \frac{\sin \theta_2}{\sin \theta_1} - \cos \theta_2 \right) \\ 0 \end{bmatrix} f_d, \quad \mathbf{f}_{d,n+1} = \begin{bmatrix} \cos \theta_3 \sin \theta_2 \\ \sin \theta_3 \sin \theta_2 \\ \cos \theta_2 \\ 0 \\ 0 \\ 0 \end{bmatrix} f_d, \quad \mathbf{f}_{d,n+2} = \begin{bmatrix} \frac{1}{2} \cos \theta_3 \left( \frac{\cos \theta_2}{\sin \theta_1} - \sin \theta_2 \right) \\ \frac{1}{2} \sin \theta_3 \left( \frac{\cos \theta_2}{\sin \theta_1} - \sin \theta_2 \right) \\ -\frac{1}{2} \left( \frac{\sin \theta_2}{\sin \theta_1} + \cos \theta_2 \right) \\ -\frac{1}{2} r_{n+2} \sin \theta_3 \left( \frac{\sin \theta_2}{\sin \theta_1} + \cos \theta_2 \right) \\ \frac{1}{2} r_{n+2} \cos \theta_3 \left( \frac{\sin \theta_2}{\sin \theta_1} + \cos \theta_2 \right) \\ 0 \end{bmatrix} f_d \tag{5}$$

The three linearized connectivity vectors for nodes  $n$  to  $n + 2$  are now obtained from (2) as

$$\mathbf{w}_n = \begin{bmatrix} \frac{1}{2} \cos \theta_3 \left( \frac{\cos \theta_2}{\sin \theta_1} + \sin \theta_2 \right) \\ \frac{1}{2} \sin \theta_3 \left( \frac{\cos \theta_2}{\sin \theta_1} + \sin \theta_2 \right) \\ -\frac{1}{2} \left( \frac{\sin \theta_2}{\sin \theta_1} - \cos \theta_2 \right) \\ -\frac{1}{2} r_n \sin \theta_3 \left( \frac{\sin \theta_2}{\sin \theta_1} - \cos \theta_2 \right) \\ \frac{1}{2} r_n \cos \theta_3 \left( \frac{\sin \theta_2}{\sin \theta_1} - \cos \theta_2 \right) \\ 0 \end{bmatrix}, \quad \mathbf{w}_{n+1} = \begin{bmatrix} -\cos \theta_3 \sin \theta_2 \\ -\sin \theta_3 \sin \theta_2 \\ -\cos \theta_2 \\ 0 \\ 0 \\ 0 \end{bmatrix}, \quad \mathbf{w}_{n+2} = \begin{bmatrix} -\frac{1}{2} \cos \theta_3 \left( \frac{\cos \theta_2}{\sin \theta_1} - \sin \theta_2 \right) \\ -\frac{1}{2} \sin \theta_3 \left( \frac{\cos \theta_2}{\sin \theta_1} - \sin \theta_2 \right) \\ \frac{1}{2} \left( \frac{\sin \theta_2}{\sin \theta_1} + \cos \theta_2 \right) \\ \frac{1}{2} r_{n+2} \sin \theta_3 \left( \frac{\sin \theta_2}{\sin \theta_1} + \cos \theta_2 \right) \\ -\frac{1}{2} r_{n+2} \cos \theta_3 \left( \frac{\sin \theta_2}{\sin \theta_1} + \cos \theta_2 \right) \\ 0 \end{bmatrix}, \tag{6}$$

The connectivity vector for the full brace is obtained by assembling the nodal vectors in (6) as

$$\mathbf{w}^T = [\dots \mathbf{w}_n^T \mathbf{w}_{n+1}^T \mathbf{w}_{n+2}^T \dots]^T, \tag{7}$$

The total load vector associated with several braces in a collective damping system is given by the summation

$$\mathbf{f}_d = \sum_k^N \mathbf{f}_{d,k}, \tag{8}$$

where  $N$  denotes the total number of damper braces in the circumferential direction.

**Influence of external damping system**

The dampers in the damper-brace system are assumed to be viscous dampers with a single common viscous damping parameter  $c$ . When expressing the damper force from each damper  $f_{d,k}$  in the frequency domain as

$$f_{d,k} = i c \omega u_{d,k}, \tag{9}$$

the contribution from the external damping system is

$$\mathbf{f}_d = -i \omega c \sum_k^N \mathbf{w}_k \mathbf{w}_k^T \mathbf{u}, \tag{10}$$

where  $N$  again denotes the total number of damper-braces in the circumferential direction. Setting  $\mathbf{f}_{ext} = \mathbf{0}$ , neglecting structural damping,  $\mathbf{C} = \mathbf{0}$ , and substituting (10) into the frequency representation of (1), gives the frequency equation of motion for the combined tower and damping system

$$\left( \mathbf{K} - \omega^2 \mathbf{M} + i \omega c \sum_k \mathbf{w}_k \mathbf{w}_k^T \right) \mathbf{u} = \mathbf{0}, \tag{11}$$

from which the eigenfrequencies  $\omega$ , associated with the side-to-side and the fore-aft mode, of the combined system are determined in the following section. For vanishing damping parameter ( $c = 0$ ) the frequency equations of motion of the undamped structure is recovered

$$(\mathbf{K} - \omega_0^2 \mathbf{M}) \mathbf{u}_0 = \mathbf{0} \tag{12}$$

For infinite damping parameter ( $c \rightarrow \infty$ ) the dampers are locked, leading to the frequency equation for another undamped system

$$(\mathbf{K} - \omega_\infty^2 \mathbf{M}) \mathbf{u}_\infty = \mathbf{r} \tag{13}$$

where  $\mathbf{r} = \mathbf{w} r$  is the reaction vector given in terms of the reaction force  $r$  required to lock the dampers.

*Two component representation for a single frequency*

The frequency of the side-to-side mode and for-aft mode are dealt with separately, by describing the combined system with tower and dampers in a two-component representation as proposed in [7]. In this simplified approach the full state  $\mathbf{u}$  is projected on to a subspace expanded by the two limiting real valued mode shapes,  $\mathbf{u}_0$  from (12), and  $\mathbf{u}_\infty$  from (13), whereby

$$\mathbf{u} = \mathbf{u}_0 \xi_0 + \mathbf{u}_\infty \xi_\infty, \tag{14}$$

with  $\xi_0$  and  $\xi_\infty$  as the corresponding modal amplitudes. From (14) an approximate explicit formula for the frequency  $\omega$  of the combined system can be derived, see [10], as

$$\frac{\omega - \omega_0}{\omega_\infty - \omega_0} = \frac{\Delta\omega}{\Delta\omega_\infty} \simeq \frac{i\eta}{1 + i\eta}, \tag{15}$$

where  $\eta$  is a non-dimensional damping parameter

$$\eta = \frac{\omega_0 c}{\omega_\infty^2 - \omega_0^2} \sum_k^N \gamma_k^2 = \frac{\omega_0 c}{\omega_\infty^2 - \omega_0^2} \gamma^2, \tag{16}$$

given by the cumulative sum,  $\gamma^2 = \sum_k^N \gamma_k^2$ , of the displacement of each damper  $\gamma_k = \mathbf{w}_k^T \mathbf{u}_0$ , as the mode shape  $\mathbf{u}_0$  has been normalized to unit modal mass,  $\mathbf{u}_0^T \mathbf{M} \mathbf{u}_0 = 1$ . The relation in (15) for the relative frequency increment has a general character. It describes a semi-circular trajectory in the complex plane, which for  $\eta = 1$  gives a maximum value for the imaginary part

$$\frac{\Delta\omega}{\Delta\omega_\infty} = \frac{i}{1 + i} \Rightarrow \text{Im}[\Delta\omega] = \text{Im}[\omega] = \frac{1}{2} \Delta\omega_\infty \tag{17}$$

This point corresponds to maximum attainable damping. The complex valued natural frequency is described in terms of the damping ratio  $\zeta$  as

$$\omega = |\omega| \left( \sqrt{1 - \zeta^2} + i\zeta \right), \quad (18)$$

whereby the damping ratio is given by

$$\zeta = \frac{\text{Im}[\omega]}{|\omega|} \quad (19)$$

Maximum attainable damping follows from insertion of (17), whereby

$$\zeta_{max} = \frac{\Delta\omega_{\infty}}{2|\omega|} \simeq \frac{\Delta\omega_{\infty}}{\omega_0 + \omega_{\infty}}, \quad (20)$$

where  $2|\omega| \simeq \omega_0 + \omega_{\infty}$  has been used to obtain the last expression. From (20) it is clear that attainable damping only depends on the change in frequency caused by locking the damper. For lightly damped structures, damping of the structure and the damping introduced by the external dampers are approximately additive, and  $\zeta_{max}$  is therefore the increase in damping. The optimum value for the viscous parameter,  $c_{opt}$ , is found from equation (16) by setting  $\eta = 1$ , whereby

$$c_{opt} = \frac{\omega_{\infty}^2 - \omega_0^2}{\omega_0 \gamma^2} \quad (21)$$

It is clearly seen that optimum tuning to get maximum damping is given as a ratio between the change in frequency associated with locking the dampers and the sum of the displacement across the dampers.

## Numerical simulations

The objective of this numerical example is to demonstrate the performance of the curvature-brace and curvature toggle-brace in damping of tower vibrations of an offshore wind turbine. The study considers a reference wind turbine used in the Offshore Code Comparison Collaboration study (OC3) [11]. It consist of the 77.6 m tall land based NREL 5 MW reference wind turbine, mounted on a 66 m long monopile. Viscous dampers are installed at the bottom of the tower 10 m above mean sea level, in a circumferential symmetric setup with six dampers positioned  $60^\circ$  apart, as illustrated in figures (b) and (d) for the curvature-brace and curvature-toggle-brace. The damper system is 4 m high, the dampers all use the same viscous damping parameter,  $c$ , and the brace members are assumed rigid.

### Damper displacement

Sufficient damper displacement is critical for the effective implementation of passive dampers inside the tower, in order to activate the damper and in order to reduce the damper force. The damper stroke with respect to the fore-aft and the side-to-side tower modes, is computed by equation (3) when assuming the tower top displacement in the two modes to be 0.5 m. The displacement of a damper  $u_d$  as function of the circumferential orientation of the damper,  $\theta_3$ , is seen in figure 7. The figure shows a comparison between the damper installed in a curvature-brace (dotted and dashed) and the damper installed in a curvature-toggle-brace (dash-dotted and solid). The two different curves for each brace represent the displacement with respect to the fore-aft mode and the side-to-side mode, respectively. As expected the displacement varies with respect to  $\theta_3$  according to a sine function for the fore-aft mode and according to a cosine function for the side-to-side mode. When the damper is installed in the curvature-toggle-brace the displacement is seen to be larger compared to the damper installed in the curvature-brace.

Optimum tuning of the dampers is given by equation (21). For proper tuning it is therefore especially  $\gamma^2 = \sum_k^N \gamma_k^2$ , that is relevant. Values for  $\gamma^2$  are plotted as function of the orientation of the rotor in figure 8. The figure shows curves for  $\gamma^2$  for the curvature-brace (dotted and dashed) and for the curvature-toggle-brace (dash-dotted and solid) with respect to both the fore-aft mode and side-to-side mode. As expected  $\gamma^2$  is larger for the curvature-toggle-brace than for the curvature-brace, leading to a smaller value for the optimum viscous parameter. For both braces the value of  $\gamma^2$  is approximately constant with respect to the orientation of the rotor, indicating that one value for the viscous parameter will be close to optimum for any orientation of the rotor. Furthermore, the curves for the fore-aft mode and

the side-to-side mode are very similar. If attainable damping for the two modes are the same, the optimum viscous parameter for the two modes will therefore also be the same.

*Root locus analysis*

The development of a complex root of the frequency equation (11) approximately follows a semicircle in the complex plane as described by the expression in equation (15). Figure 9 shows the development of the roots associated with the fore-aft mode and the side-to-side mode, as the value of the viscous damping parameter  $c$  is increased. Figures 9(a) and (b) are for the curvature-brace and figures 9(c) and (d) are for the curvature-toggle-brace. The solid curve represents the theoretical expression (15) given by the non-dimensional damping parameter  $\eta$  in (16), while the dots are numerical values computed for an increasing value of  $c$  by solving (11). The values for  $c$  have been determined by appropriate tuning, according to (16), so that dots 1 to 10 correspond to the values of  $\eta$  going from 0 to 1 and dots 10 to 19 correspond to the values of  $\eta$  going from 1 to  $\infty$ . For both modes the tuning has been with respect to the side-to-side mode, which means that the values for  $c$  are the same in figures 9(a) and (b) and the same in figures 9(c) and (d). By comparing figures 9(a) and (b) for the curvature-brace and figures 9(c) and (d) for the curvature-toggle-brace, attainable damping with respect to the two different tower modes are seen to be very similar. Since the values for  $\gamma^2$  for the two modes are the same, optimum tuning for the two modes is approximately the same. This is also seen by dot 10 being approximately at the maximum of both curves. Furthermore, attainable damping for the two braces is also seen to be similar, which demonstrates that the curvature-toggle-brace delivers the same damping as the curvature-brace, but with smaller damper size.

*Damper force*

The damper force is determined by equation (9), and the displacement of the damper with respect to the side-to-side mode, scaled according to a tower top displacement of 0.5 m. This is identical to the damper displacement shown in figure 7. Figure 10(a) shows the damper force as a function of  $\theta_3$  for a damper in a curvature-brace and figure 10(b) shows the damper force for a damper in a curvature-toggle-brace. The solid line in the figures corresponds to optimum viscous damping  $\zeta = \zeta_{max}$ , while the dashed line corresponds to a damping ratio half that of attainable damping  $\zeta = \zeta_{max}/2$ . As expected the damper force corresponding to optimum damping for a damper in a curvature-toggle-brace is significantly smaller than the damper force of a damper in curvature brace. Furthermore, due to the semicircular trajectory of the complex root in the complex plane, a damper system with a damping ratio half that of maximum attainable damping, only needs a damper force that is approximately one fourth of the damper force needed at optimum.

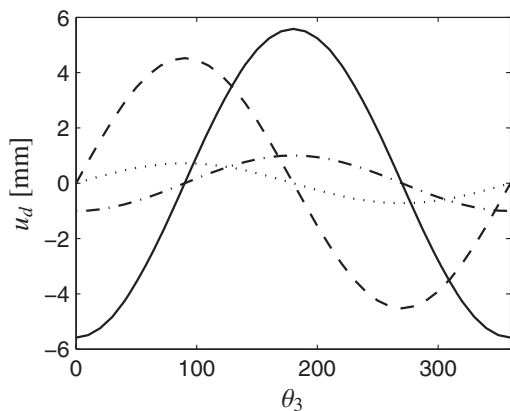


Fig. 7.  $u_d$  for the curvature brace with respect to the fore-aft mode (dotted) and the side-to-side mode (dash-dotted) and  $u_d$  for the curvature-toggle brace with respect to the fore-aft mode (dashed) and the side-to-side mode (solid)

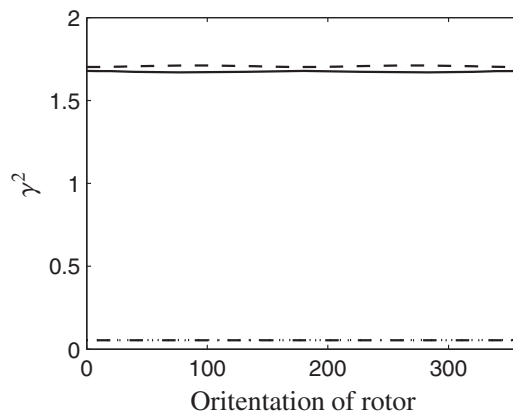


Fig. 8.  $\gamma^2$  for six curvature-braces with respect to the fore-aft mode (dotted) and the side-to-side mode (dash-dotted) and  $u_d$  for six curvature-toggle braces with respect to the fore-aft mode (dashed) and the side-to-side mode (solid)

Time simulation in HAWC2

In order to further investigate the damping effect of installing passive dampers in curvature-toggle-braces in a wind turbine tower, a simple time simulation is carried out using the commercial code HAWC2 [12]. HAWC2 (Horizontal Axis Wind turbine simulation Code 2nd generation) is an aero-elastic code developed at DTU Wind Energy, which allows for dynamic simulations of wind turbines during operation. A model of the OC3 reference wind turbine is used for the time simulations. The model includes Rayleigh damping, equivalent to a damping ratio of  $\zeta_u \approx 0.0065$  for the first two tower modes. The brace members and the toggle mechanism are modeled directly in HAWC2, while the damper is modeled as an external system using a d11 [13]. The curvature-toggle-brace system which is implemented in the HAWC2 model consist of six toggle-braces in a  $60^\circ$  configuration, equivalent to the system modeled with the simple beam model. The viscous damping parameter is tuned to optimum according to (21).

The wind turbine is again assumed at standstill. The structure is loaded by a single harmonic force acting at the waterline of the monopile, at an angle of  $45^\circ$  to the rotor direction, thus initiating both the fore-aft mode and the side-to-side mode. After some time the force is removed and the free decay is observed. Figure (11)(a) shows the tower

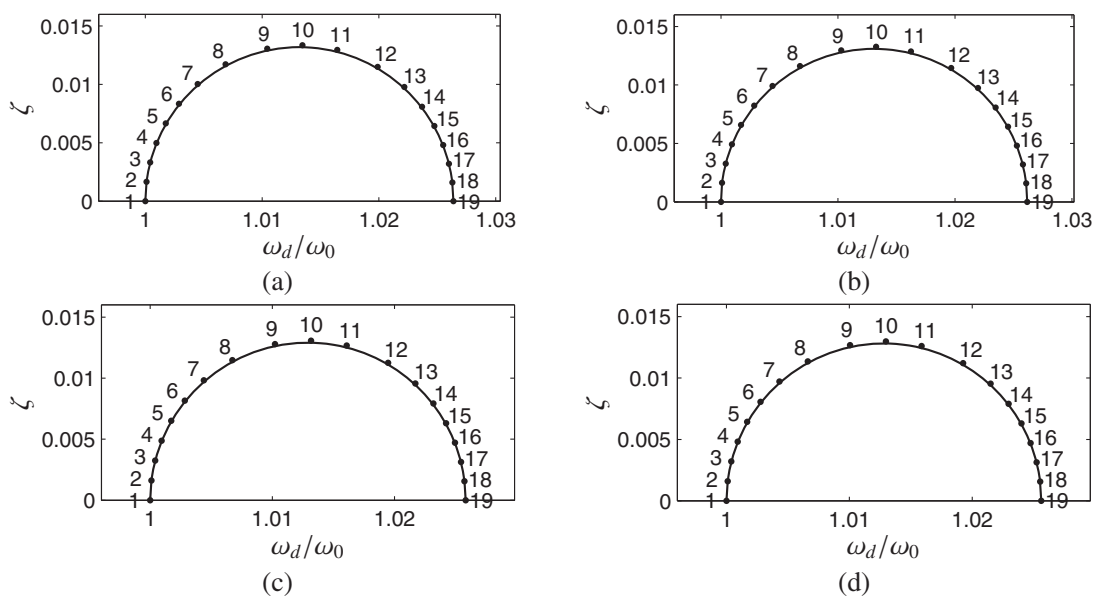


Fig. 9. Root locus associated with a curvature-brace system for (a) the fore-aft mode and (b) the side-to-side mode and root locus associated with a curvature-toggle-brace system for (c) the fore-aft mode and (d) the side-to-side mode

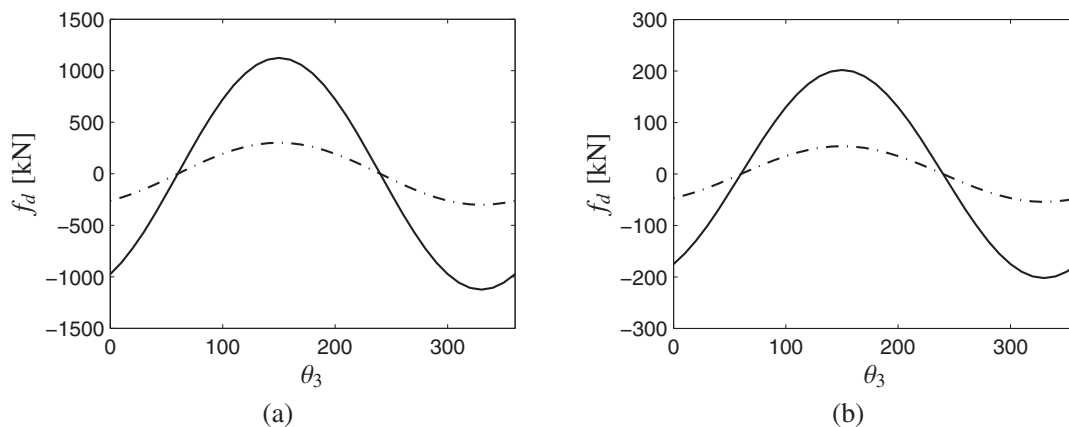


Fig. 10. Damper force as a function of  $\theta_3$  for the curvature-brace (a) and for the curvature-toggle-brace (b). The curves are for optimum damping  $\zeta = \zeta_{max}$  (solid) and for a damping ratio half that of maximum attainable damping  $\zeta = \zeta_{max}/2$  (dash-dotted)

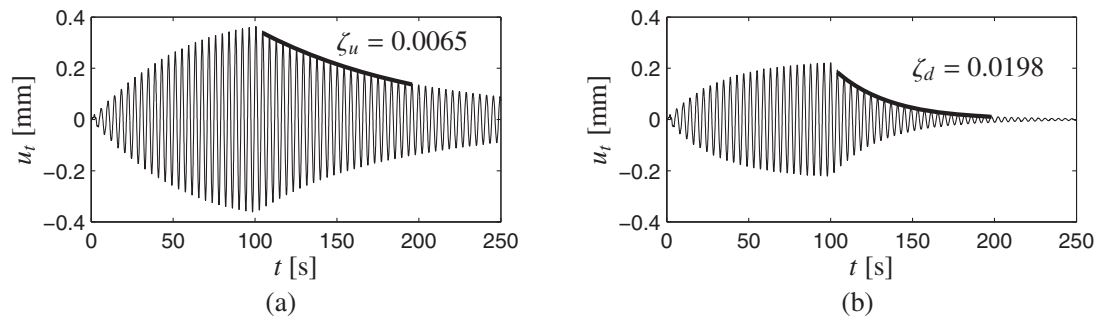


Fig. 11. Time simulation from HAWC2 without dampers (a) and with dampers (b)

top displacement for the wind turbine without external dampers, and figure (11)(b) shows the tower top displacement for the wind turbine with external dampers. The free decay is fitted with an exponential fit (solid line), from which an estimate of the damping ratio is computed. As expected the wind turbine with external dampers has the highest damping ratio. The difference in damping ratio between the two time simulations is  $\Delta\zeta = \zeta_d - \zeta_u \approx 0.013$ , which corresponds well to the maximum attainable damping previously estimated by the simple beam model.

## Conclusion

A new toggle-brace-damper concept for installing dampers at the bottom of fixed offshore wind turbines has been presented. Compared to a brace design where the damper is connected directly to the tower wall, the damper stroke is significantly increased, thereby increasing the feasibility of installing dampers inside the tower. In the numerical example presented a single circumferential row of toggle brace dampers is seen to increase the damping ratio of the two lowest tower modes by  $\Delta\zeta = 0.013$ . In a practical implementation 2-3 rows of dampers at different heights could be installed together in order to further increase attainable damping. As offshore wind turbines continue to increase in size and are moved to larger water depths, the toggle-brace-damper concept could become a feasible alternative to the tuned mass damper concept for damping of offshore wind turbine tower vibrations.

## References

- [1] Tarp-Johansen, N., Andersen, L., Christensen, E., Mørch, C., Frandsen, S., Kallešøe, B.. Comparing sources of damping of cross-wind motion. In: Proceedings of the European Wind Energy Conference & Exhibition. Stockholm, Sweden; 2009..
- [2] Colwell, S., Basu, B.. Tuned liquid column dampers in offshore wind turbines for structural control. *Engineering Structures* 2009;31(2):358–368.
- [3] Lackner, M.A., Rotea, M.A.. Passive structural control of offshore wind turbines. *Wind energy* 2011;14(3):373–388.
- [4] Fischer, T., Rainey, P., Bossanyi, E., Kühn, M.. Study on control concepts suitable for mitigation of loads from misaligned wind and waves on offshore wind turbines supported on monopiles. *Wind Engineering* 2011;35(5):561–574.
- [5] Constantinou, M., Tsopelas, P., Hammel, W., Sigaher, A.. Toggle-brace-damper seismic energy dissipation systems. *Journal of Structural Engineering* 2001;127(2):105–112.
- [6] Hwang, J.S., Huang, Y.N., Hung, Y.H.. Analytical and experimental study of the toggle-brace-damper systems. *Journal of Structural Engineering* 2005;131(7):1035–1043.
- [7] Main, J., Krenk, S.. Efficiency and tuning of viscous dampers on discrete systems. *Journal of Sound and Vibration* 2005;286(1-2):97–122.
- [8] Krenk, S.. A general format for curved and non-homogeneous beam elements. *Computers & structures* 1994;50(4):449–454.
- [9] Svendsen, M., Krenk, S., Høgsberg, J.. Wind turbine rotors with active vibration control. Ph.D. thesis; DTU; 2011.
- [10] Høgsberg, J.R., Krenk, S.. Linear control strategies for damping of flexible structures. *Journal of Sound and Vibration* 2006;293(1):59–77.
- [11] Jonkman, J., Musial, W.. Offshore code comparison collaboration (OC3) for IEA task 23 offshore wind technology and deployment. Tech. Rep.; National Renewable Energy Laboratory; 2010. NREL/TP-500-48191.
- [12] Larsen, T.J., Hansen, A.M.. How 2 HAWC2, the user's manual. Risø National Laboratory; 2007.
- [13] Hansen, A.M., Larsen, T.J.. Gear dynamics. Tech. Rep.; Risø National Lab.; 2009. Research in Aeroelasticity EFP-2007-II, Risø-R-1698(EN):134-142.



# P2

Hybrid damper with stroke amplification  
for damping of offshore wind turbines

Mark L. Brodersen, Jan Høgsberg

*Wind Energy*,  
Published online, 2016.

## RESEARCH ARTICLE

# Hybrid damper with stroke amplification for damping of offshore wind turbines

Mark L. Brodersen and Jan Høgsberg

Department of Mechanical Engineering, Technical University of Denmark, DK-2800 Kgs., Lyngby, Denmark

## ABSTRACT

The magnitude of tower vibrations of offshore wind turbines is a key design driver for the feasibility of the monopile support structure. A novel control concept for the damping of these tower vibrations is proposed, where viscous-type hybrid dampers are installed at the bottom of the wind turbine tower. The proposed hybrid damper consists of a passive viscous dashpot placed in series with a load cell and an active actuator. By integrated force feedback control of the actuator motion, the associated displacement amplitude over the viscous damper can be increased compared with the passive viscous case, hereby significantly increasing the feasibility of viscous dampers acting at the bottom of the wind turbine tower. To avoid drift in the actuator displacement, a filtered time integration of the measured force signal is introduced. Numerical examples demonstrate that the filtered time integration control leads to performance similar to that of passive viscous damping and substantial amplification of the damper deformation without actuator drift. Copyright © 2016 John Wiley & Sons, Ltd.

## KEYWORDS

monopile; tower vibrations; hybrid damper; integral force feedback; vibration control

## Correspondence

Mark L. Brodersen, Department of Mechanical Engineering, Technical University of Denmark, DK-2800 Kgs. Lyngby, Denmark.

E-mail: mlai@mek.dtu.dk

Received 30 March 2015; Revised 31 October 2015; Accepted 26 January 2016

## 1. INTRODUCTION

The monopile foundation is currently the most used support structure for shallow water offshore wind turbines. Compared with a jacket-type foundation, the monopile has a simple and relatively cost-effective design, which on the other hand also makes it prone to wave loading. It is primarily a combination of the two lowest tower modes, the side–side mode and the fore–aft mode as seen in Figure 1, which are excited by the waves. Especially, waves misaligned with the wind direction can cause large fatigue damage because of the absence of aerodynamic damping in the direction lateral to the wind.<sup>1,2</sup> In the near future, the majority of new offshore wind turbines will be taller and/or positioned at deeper waters, whereby the natural frequencies of the side–side mode and the fore–aft mode will be lowered. The natural frequencies will then move closer to the primary excitation frequency of the waves, causing resonant excitation to be more frequent. This may render the monopile support structure unfeasible. A means for increasing the feasibility of the monopile support structure would be to add external damping to the critical modes of the wind turbine structure.

Several concepts have been proposed for structural control of tower vibrations of offshore wind turbines. Passive resonant damper concepts like a pendulum absorber or a tuned mass or liquid damper are well-established concepts in structural control and therefore widely used by the wind turbine manufactures for vibration control of offshore wind turbines.<sup>3–7</sup> A resonant damper like a pendulum absorber has the potential to achieve very high damping ratios, although in order for the absorber to be effective, large mass and space at the top of the wind turbine is required. As wind turbines become larger and located at larger water depths, these mass and space requirements will increase and thereby limit the feasibility of pendulum-type absorbers even further. Active concepts such as individual pitch control or active generator torque control have also been proposed for control of the side–side vibrations.<sup>8,9</sup> These concepts are relatively easy to integrate in a standard rotor–nacelle assembly (RNA) unit, although they may increase loading on other components such as the gearbox or the pitch actuators. More recently, a passive concept has been proposed,<sup>10</sup> where dampers are installed inside the tower to act on the local curvature of the corresponding tower bending deformation. This concept utilizes stroke amplifying braces in order to amplify the relative motion of the tower, although the amplification is inherently limited for passive damping

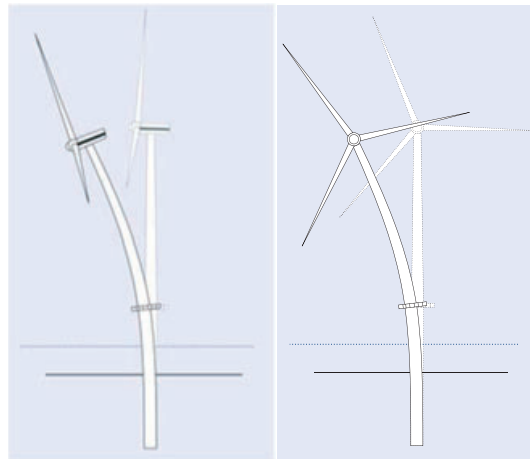


**Figure 1.** Fore–aft mode and side–side mode of a fixed offshore wind turbine.

devices. The specific concept of using toggle-brace damping systems for wind turbines has recently been covered by the patent.<sup>11</sup>

In the present paper, it is proposed to install dampers inside the bottom of the tower by means of the viscous hybrid damper concept introduced by Høgsberg and Brodersen.<sup>12</sup> The hybrid damper concept includes a pure viscous dashpot placed in series with both a force sensor and an active actuator. The actuator motion is controlled using a decentralized collocated control algorithm based on a filtered integral force feedback (IFF) from the force sensor. In this paper, a slightly modified controller scheme, without the filter time constant, is used. Eliminating the filter time scale from the feedback equation, the pure IFF scheme, introduced in another paper,<sup>13,14</sup> for control of truss structures using piezoelectric transducers, is recovered. Among other applications, the IFF format has also successfully been applied for control of cable-stayed bridges<sup>15,16</sup> and for control of large space structures.<sup>17</sup> In the present hybrid damper concept, appropriate tuning of this IFF controller scheme introduces amplified motion of the structure locally at the damper position, leading to significantly larger stroke over the viscous dashpot. Thus, the stroke amplification obtained by toggle-brace systems in the papers of Brodersen and Høgsberg<sup>10</sup> and Tsouroukdissian<sup>11</sup> is in the present case realized by active control. Since the generated hybrid damper force is in phase with the associated damper velocity, the controller scheme is theoretically unconditionally stable in an idealized environment without time delays and actuator saturation.

## 2. THE HYBRID DAMPER CONCEPT

The hybrid damper concept is illustrated in Figure 2(a). It consists of a viscous dashpot with viscous damping parameter  $c$  in series with a load cell, measuring the damper force  $f$  and an active actuator with piston motion  $q$ . The motion over the hybrid damper is given by  $u$ , whereby the measured force produced by the viscous dashpot is given as

$$f(t) = c(\dot{u}(t) - \dot{q}(t)) \quad (1)$$

The displacement of the actuator piston  $q(t)$  is determined by an IFF scheme,<sup>13</sup> given as

$$\dot{q}(t) = -gf(t) \quad (2)$$

where  $g$  is the control gain. For  $g = 0$ , the passive limit without piston motion  $q = 0$  is recovered. In large-scale structures, such as wind turbines, the desired damper reference signal  $q$  may be realized by a hydraulic actuator with, e.g. Proportional Integral Derivative (PID) control of the piston motion, measured by a Linear Variable Differential Transformer (LVDT) or an alternative displacement transducer. The implementation of active control strategies, and in particular IFF, is described in detail in another study.<sup>14</sup> The installation of the hybrid damper in a wind turbine tower is illustrated in Figure 2(b),(c). The direction of the fore–aft vibrations in the direction of the rotor is denoted by f-a, while the direction of the side–side vibrations is denoted by s-s. In these, the two most critical tower modes with regard to wave excitation, the tower is primarily deformed in bending, and the damper should therefore be installed at the bottom of the tower in order to maximize modal interaction, as also illustrated in a side view of the tower in Figure 2(b).

During operation, the RNA will change orientation following the direction of the wind. Thus, three or more dampers are needed in the circumferential direction to form a symmetric layout that leads to efficient damping of both the fore–aft

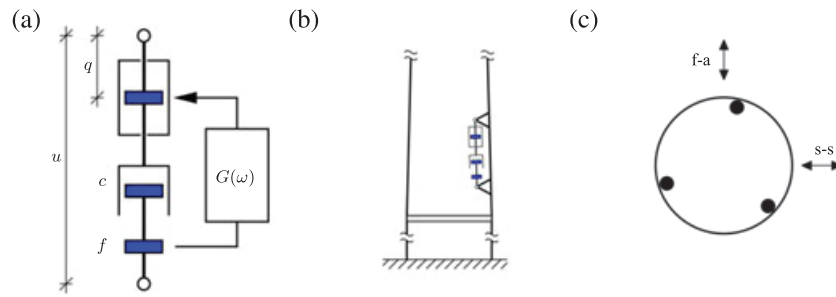


**Figure 2.** (a) Hybrid damper concept and its installation in the lower section of a wind turbine tower: (b) side view and (c) top view.

mode and the side–side mode, independent of the specific orientation of the RNA. The three-damper layout, as illustrated by the top view of the tower in Figure 2(c), is also applied for the toggle-brace systems in the papers of Brodersen and Høgsberg<sup>10</sup> and Tsouroukdissian.<sup>11</sup>

## 2.1. Frequency domain analysis

The hybrid damper characteristics are now investigated in the frequency domain. Harmonic solutions are assumed using the complex representations

$$u(t) = \bar{u} \exp i\omega t \quad , \quad q(t) = \bar{q} \exp i\omega t \quad , \quad f(t) = \bar{f} \exp i\omega t \quad (3)$$

with angular frequency  $\omega$  and with amplitudes denoted by a bar. In the frequency domain, the damper force in (1) is given by

$$\bar{f} = i\omega c (\bar{u} - \bar{q}) \quad (4)$$

The corresponding feedback equation in (2) now appears as

$$i\omega \bar{q} = -g \bar{f} \quad (5)$$

which can be rewritten in terms of the transfer function

$$G(\omega) = \frac{-g}{i\omega} \quad (6)$$

to establish the feedback relation  $\bar{q} = G(\omega)\bar{f}$  shown in Figure 2(a). The relation between damper force  $\bar{f}$  and the displacement  $\bar{u}$  of the hybrid damper is obtained by eliminating  $\bar{q}$  between (4) and (5). This gives the force relation

$$\bar{f} = i\omega c H \bar{u} \quad (7)$$

where the transfer function  $H$  in the present case is given as the constant

$$H = \frac{1}{1 - \nu} \quad (8)$$

with non-dimensional gain

$$\nu = c g \quad (9)$$

In (8), the transfer function  $H$  modifies the transfer relation of the hybrid damper relative to the pure viscous damper, which in the following will be used as a benchmark for assessing the performance of the proposed hybrid damper concept. In order to have positive damping, it is required that  $H > 0$ , thereby invoking the limit  $\nu < 1$ . The phase  $\varphi$  of the damper force is defined by the relation  $\tan \varphi = \text{Im}[H] / \text{Re}[H]$ , which for  $\nu < 1$  gives  $\varphi = 0$ . Thus, for the pure IFF controller, the damper force is fully in phase with damper velocity, and the controller is therefore unconditionally stable for  $\nu < 1$ . The amplification of the displacement over the viscous dashpot relative to the passive case with  $q = 0$  is given by the magnitude  $|H|$  of the transfer function

$$|H| = \left| \frac{\bar{u} - \bar{q}}{\bar{u}} \right| = \left| \frac{1}{1 - \nu} \right| \quad (10)$$

Thus, for  $0 < \nu < 1$ , the displacement of the viscous dashpot is amplified relative to the passive case with  $q = 0$ , whereas for  $\nu = 0$ , the pure viscous case is recovered. In this way, the hybrid damper can be used to increase the feasibility of installing a viscous damper in a flexible structure, such as a wind turbine, where the displacement over the damper is inherently small.

## 2.2. Filtered integration

The hybrid damper implemented with the IFF controller, as given by the feedback relation in (6), has a pole at  $s = i\omega = 0$  in the Laplace domain. This makes it prone to drift in the actuator displacement, which again can lead to saturation of the actuator signal. In order to reduce this drift, the actuator velocity is now integrated by a suitable filter. First, the actuator velocity is defined as an independent variable  $v = \dot{q}$ , and the feedback equation in (2) is therefore rewritten as

$$v(t) = -gf(t) \quad (11)$$

Subsequently, the actuator displacement  $q$  is obtained by integration of the velocity  $v$  through the second-order filter

$$\omega_f q(t) + \dot{q}(t) + \tau_f \ddot{q}(t) = v(t) \quad (12)$$

The first term with the corner frequency  $\omega_f$  reduces drift and potential actuator saturation in the command displacement signal  $q$ . Note that this is similar to the introduction of a forgetting factor in the paper of Preumont and colleagues.<sup>13</sup> The last term in (12) with the filter time constant  $\tau_f$  is added to compensate for the phase delay caused by the first term. The influence of this term will be demonstrated later in this section. Combining equations 11 and (12) gives

$$\omega_f q(t) + \dot{q}(t) + \tau_f \ddot{q}(t) = -gf(t) \quad (13)$$

In the frequency domain, obtained by assuming harmonic solutions as in (3), this equation can be written as

$$\left(\omega_f - \omega^2 \tau_f + i\omega\right) \bar{q} = -g\bar{f} \quad (14)$$

whereby the modified transfer function  $G(\omega)$  is given as

$$G(\omega) = \frac{-g}{\omega_f - \omega^2 \tau_f + i\omega} \quad (15)$$

The previous pole at  $i\omega = 0$  for the pure IFF format is now replaced by the pair of complex conjugate poles

$$s = i\omega = -1/(2\tau_f) \pm \sqrt{\omega_f/\tau_f} \sqrt{1/(4\omega_f\tau_f) - 1} \quad (16)$$

which reduces the actuator drift. Combining (14) with (4), the transfer function  $H(\omega)$  defined in (7) is now given as

$$H(\omega) = \frac{\omega_f - \tau_f \omega^2 + i\omega}{\omega_f - \tau_f \omega^2 + i\omega(1-\nu)} \quad (17)$$

with real and imaginary parts

$$\text{Re}[H(\omega)] = \frac{(\omega_f - \tau_f \omega^2)^2 + \omega^2(1-\nu)}{(\omega_f - \tau_f \omega^2)^2 + \omega^2(1-\nu)^2}, \quad \text{Im}[H(\omega)] = \frac{\omega\nu(\omega_f - \tau_f \omega^2)}{(\omega_f - \tau_f \omega^2)^2 + \omega^2(1-\nu)^2} \quad (18)$$

For  $\omega_f, \tau_f \rightarrow 0$ , the transfer function recovers the expression given in (8) for the pure IFF format. The frequency characteristics of  $H(\omega)$  given in (17) are conveniently described in terms of the magnitude

$$|H(\omega)| = \left| \frac{\bar{u} - \bar{q}}{\bar{u}} \right| = \sqrt{\frac{(\omega_f - \tau_f \omega^2)^2 + \omega^2}{(\omega_f - \tau_f \omega^2)^2 + \omega^2(1-\nu)^2}} \quad (19)$$

which represents the amplification of the damper displacement, and by the phase angle  $\varphi$  obtained from

$$\tan \varphi = \frac{\text{Im}[H(\omega)]}{\text{Re}[H(\omega)]} = \frac{\omega\nu(\omega_f - \tau_f \omega^2)}{\omega^2(1-\nu) + (\omega_f - \tau_f \omega^2)^2} \quad (20)$$

It can be seen from (19) that the amplification of the displacement over the viscous dashpot is in general reduced for nonnegative filter parameters  $\omega_f, \tau_f > 0$ , which unfortunately reduces the performance of the hybrid damper. However, by

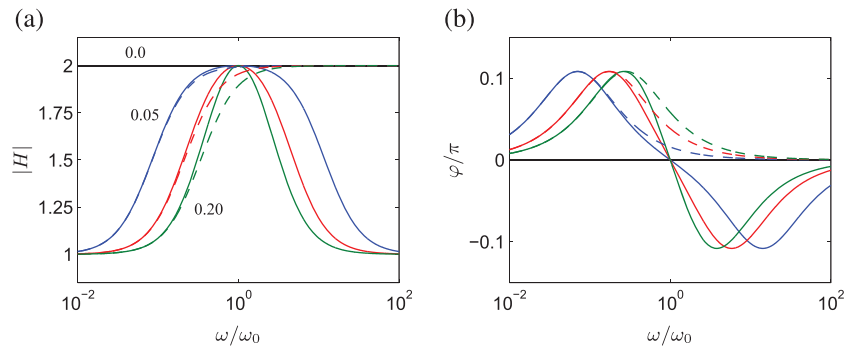


**Figure 3.** (a) Magnitude and (b) phase of frequency transfer function  $H(\omega)$  for  $\nu = 0.5$  with  $\tau_f = \omega_f/\omega_0^2$  (solid) and  $\tau_f = 0$  (dashed) and filter frequency  $\omega_f = 0.0$  (black),  $\omega_0/20$  (blue),  $\omega_0/8$  (red) and  $\omega_0/5$  (green).

choosing  $\omega_f$  and  $\tau_f$  so that  $\omega_f = \tau_f \omega_0^2$ , where  $\omega_0$  is the natural frequency of the structure, the magnitude and phase at this structural frequency  $\omega_0$  become

$$|H(\omega_0)| = \left| \frac{1}{1-\nu} \right|, \quad \varphi(\omega_0) = 0 \quad (21)$$

It is seen that the result for the pure IFF format in (8) is in fact recovered at structural resonance corresponding to  $\omega = \omega_0$ .

Figure 3 shows a plot of (i) the magnitude  $|H(\omega)|$  as given in (19) and (ii) the phase angle  $\varphi$  obtained from (20). The non-dimensional gain value is  $\nu = 0.5$ , while different values of  $\omega_f$  and  $\tau_f$  are chosen. The solid curves in the figure are for different nonnegative values of  $\omega_f = \tau_f \omega_0^2 < \omega_0$ , while the dashed curves represent the particular case with  $\tau_f = 0$  and different nonnegative values of  $\omega_f < \omega_0$ . The values of  $\omega_f$  are  $\omega_0/20$  (blue),  $\omega_0/8$  (red),  $\omega_0/5$  (green) and 0.00 (straight black). The latter case with  $\omega_f = 0$  corresponds to the case without filtered integration. For  $\tau_f = 0$  and  $0 < \omega_f < \omega_0$  (dashed curves), the magnitude is seen to be reduced to  $|H(\omega)| < 2$  compared with the case without filtered integration (straight black solid curve) with  $|H| = 2$ . The reduction is largest for frequencies below the resonance frequency  $\omega_0$ . For the case with  $\omega_f = \tau_f \omega_0^2$  (solid curves), the magnitude is reduced for the frequency intervals below and above the resonance frequency  $\omega_0$ , while around the resonance frequency  $\omega = \omega_0$ , the desired level of stroke amplification is retained. Thus, the amplification of the displacement of the damper is at its maximum at the structural resonance frequency where effective vibration damping is required.

The phase angle is plotted in Figure 3(b). For  $\tau_f = 0$  (dashed curves), a phase lead  $\varphi > 0$  is observed compared with the pure viscous case (straight black solid curve). For the case with  $\omega_f = \tau_f \omega_0^2$  (solid curves), a phase lead is observed below the resonance frequency  $\omega_0$ , while a phase lag  $\varphi < 0$  is obtained for frequencies above  $\omega_0$  with vanishing phase angle  $\varphi = 0$  at  $\omega = \omega_0$ . A phase lead  $\varphi > 0$  implies that the damper force acts ahead of the conjugated damper velocity, while a phase lag  $\varphi < 0$  corresponds to a damper force trailing velocity. The effect of a phase difference compared with pure viscous damping is discussed in the paper of Høgsberg and Krenk,<sup>18</sup> where it is demonstrated that a phase lead results in improved damper performance. Thus, by choosing the filter parameters from the equality  $\omega_f = \tau_f \omega_0^2$ , the drift of the actuator motion can be reduced, while retaining the desired displacement amplification at the natural frequency  $\omega_0$  of the critical mode(s) of the wind turbine. In practice, the filter parameters should be chosen large enough to limit drift, but also small enough not to deteriorate the damping performance of the hybrid damper in the frequency range close to the structural frequency  $\omega_0$ .

### 3. PROPERTIES OF WIND TURBINE AND DAMPERS

The present section introduces a numerical wind turbine model for later use in the investigation of damping of tower vibrations, with particular emphasis on the installation of the hybrid dampers. The wind turbine model is the 5 MW offshore wind turbine from the Offshore Code Comparison Collaboration study.<sup>19</sup> The wind turbine is supported by a monopile foundation, which is positioned at 20 m water depth with a penetration length of 36 m and connected to the wind turbine tower 10 m above mean sea level (MSL). The tower is connected to the nacelle at 87.6 m above MSL, with the hub located at a height of 90 m. Dampers are installed on the tower wall at the bottom of the tower with the upper point of attachment located 4 m above the bottom.

#### 3.1. Linear beam model

Initially, the wind turbine is assumed to be at standstill, and the wind turbine and monopile are therefore represented by a linear discrete beam model, with the horizontal  $y$ -axis in the rotor direction, the horizontal  $x$ -axis lateral to the rotor direction

and the vertical  $z$ -axis in the longitudinal tower direction. The beam model is three dimensional with three translational displacements  $\mathbf{u}_i^T = [u_{xi} u_{yi} u_{zi}]$  and three rotations  $\varphi^T = [\varphi_{xi} \varphi_{yi} \varphi_{zi}]$  at element nodes  $i = 1$  and  $2$ . Thus, the displacements of beam element  $j$  are described by the 12 degrees of freedom (dofs) contained in vector  $\mathbf{u}_j^T = [\mathbf{u}_1^T, \mathbf{u}_2^T]^T$ , as shown in Figure 4(a). The equations of motion for the total number of structural dofs in  $\mathbf{u}$  are given by

$$\mathbf{M}\ddot{\mathbf{u}} + \mathbf{C}\dot{\mathbf{u}} + \mathbf{K}\mathbf{u} = \mathbf{f} - \mathbf{f}_d \tag{22}$$

where  $\mathbf{M}$ ,  $\mathbf{C}$  and  $\mathbf{K}$  are the mass, damping and stiffness matrices, respectively, while  $\mathbf{f}$  is the external load vector and  $\mathbf{f}_d$  is the force vector representing the contributions from all hybrid dampers installed inside the tower. The stiffness matrix  $\mathbf{K}$  consists of a contribution from the constitutive stiffness matrix of the tower and monopile, based on the complementary energy principle following Krenk,<sup>20</sup> and a contribution from the soil stiffness, which is represented using linear springs. The mass matrix  $\mathbf{M}$  represents the distributed mass and inertia of the tower and monopile, and the inertia and mass of the nacelle, rotor and blades that are lumped at the top of the tower. The damping matrix  $\mathbf{C}$  is a proportional damping matrix that represents structural and soil damping, and it is tuned to provide the two targeted tower modes (fore–aft and side–side) with a realistic damping ratio of  $\zeta_{st} = 0.0115$  at standstill. The connection of the hybrid dampers to the tower is conveniently described by a connectivity vector  $\mathbf{w}$  for each damper, whereby the damper force vector is given by the summation

$$\mathbf{f}_d = \sum_{k=1}^r \mathbf{w}_k f_k \tag{23}$$

where  $r$  is the total number of dampers. Since the hybrid dampers are collocated, the damper displacement  $u_k$  of the  $k$ 'th damper is determined as

$$u_k = \mathbf{w}_k^T \mathbf{u} \tag{24}$$

The connectivity vector  $\mathbf{w}_k$  for the  $k$ 'th damper has the same dimension as the number of dofs in the structural model, and it contains all zeros except at the dofs for the two adjacent nodes  $n$  and  $n + 1$  where the dampers are attached in a circumferential configuration similar to that shown in Figure 4(c). The connectivity vector of the  $k$ 'th damper can therefore be written as

$$\mathbf{w}_k = [0 \quad \dots \quad 0 \quad \mathbf{w}_{k,n}^T \quad \mathbf{w}_{k,n+1}^T \quad 0 \quad \dots \quad 0]^T \tag{25}$$

where the two nodal connectivity vectors  $\mathbf{w}_{k,n}$  and  $\mathbf{w}_{k,n+1}$  associated with nodes  $n$  and  $n + 1$  of the beam model represent the lower and upper points of the damper attachment inside the tower. The vectors are determined by computing the nodal load vector that imposes the damper forces at the two tower nodes  $n$  and  $n + 1$ . This gives

$$\mathbf{w}_k^n = \begin{bmatrix} \cos(\theta_2^k) \cos(\theta_1) \\ \sin(\theta_2^k) \cos(\theta_1) \\ -\sin(\theta_1) \\ -\sin(\theta_2^k) \sin(\theta_1) d_1/2 \\ \cos(\theta_2^k) \sin(\theta_1) d_1/2 \\ 0 \end{bmatrix}, \quad \mathbf{w}_k^{n+1} = \begin{bmatrix} -\cos(\theta_2^k) \cos(\theta_1) \\ -\sin(\theta_2^k) \cos(\theta_1) \\ \sin(\theta_1) \\ \sin(\theta_2^k) \sin(\theta_1) d_2/2 \\ -\cos(\theta_2^k) \sin(\theta_1) d_2/2 \\ 0 \end{bmatrix} \tag{26}$$

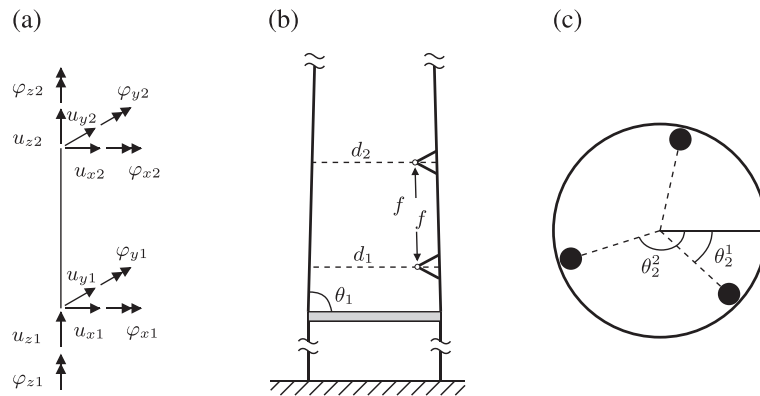


Figure 4. (a) 3D beam element and damper connectivity inside wind turbine tower: (b) side view and (c) top view.

Here,  $\theta_1$  is the conic angle of the tower, while  $d_1$  and  $d_2$  are the diameters of the tower at the lower and upper points of damper attachment inside the tower, as shown in Figure 4(b). The angle  $\theta_2^k$  represents the circumferential orientation of the  $k$ 'th damper as seen in Figure 4(c). The expressions for the two connectivity vectors in (26) only differ in terms of sign and magnitude of the lever arms  $d_1/2$  and  $d_2/2$ .

### 3.2. Stability

Inserting the viscous relation for the damper force in (1) and the feedback relation as given by (13) into the equations of motion in (22) provides the governing closed-loop equations as

$$\begin{bmatrix} \mathbf{M} & \mathbf{0} \\ \mathbf{0}^T & \tau_f \mathbf{I} \end{bmatrix} \begin{bmatrix} \ddot{\mathbf{u}} \\ \ddot{\mathbf{q}} \end{bmatrix} + \begin{bmatrix} \mathbf{C} + c\mathbf{W}\mathbf{W}^T & -c\mathbf{W} \\ \nu\mathbf{W}^T & (1-\nu)\mathbf{I} \end{bmatrix} \begin{bmatrix} \dot{\mathbf{u}} \\ \dot{\mathbf{q}} \end{bmatrix} + \begin{bmatrix} \mathbf{K} & \mathbf{0} \\ \mathbf{0}^T & \omega_f \mathbf{I} \end{bmatrix} \begin{bmatrix} \mathbf{u} \\ \mathbf{q} \end{bmatrix} = \begin{bmatrix} \mathbf{f} \\ \mathbf{0} \end{bmatrix} \quad (27)$$

where the dofs of the actuators are conveniently collected in the single column vector  $\mathbf{q}^T = [q_1 \dots q_r]$ , while the connectivity vectors are combined into a single matrix  $\mathbf{W} = [\mathbf{w}_1 \dots \mathbf{w}_r]$ . Assuming that  $\omega_f, \tau_f > 0$ , a nonnegative energy functional for the system of equations of motion in (27) is formulated as

$$V = \frac{1}{2} \dot{\mathbf{u}}^T \mathbf{M} \dot{\mathbf{u}} + \frac{1}{2} \frac{\tau_f}{g} \dot{\mathbf{q}}^T \dot{\mathbf{q}} + \frac{1}{2} \mathbf{u}^T \mathbf{K} \mathbf{u} + \frac{1}{2} \frac{\omega_f}{g} \mathbf{q}^T \mathbf{q} \geq 0 \quad (28)$$

The corresponding rate of this function is obtained from (27) and given by the expression

$$\dot{V} = -\dot{\mathbf{u}}^T \mathbf{C} \dot{\mathbf{u}} - c \left( \dot{\mathbf{u}}^T \mathbf{W} \mathbf{W}^T \dot{\mathbf{u}} + \dot{\mathbf{q}}^T \dot{\mathbf{q}} \frac{1-\nu}{\nu} \right) \quad (29)$$

This rate of the functional is negative for  $0 \leq \nu < 1$ . Thus, for  $(\mathbf{u}, \dot{\mathbf{u}}, \mathbf{q}, \dot{\mathbf{q}}) \neq 0$ , the energy  $V$  is a Lyapunov function, and the system in (27) is therefore asymptotically stable for  $0 \leq \nu < 1$  according to Lyapunov's second stability theorem.<sup>21</sup>

### 3.3. Damper tuning

As demonstrated by Main and Krenk,<sup>22</sup> the optimum tuning of supplemental viscous dampers can be estimated from a two-component representation, where the structural motion is expressed as a linear combination of the undamped mode shape  $\mathbf{u}_0$  determined from the undamped eigenvalue problem

$$(\mathbf{K} - \omega_0^2 \mathbf{M}) \mathbf{u}_0 = 0 \quad (30)$$

with natural frequency  $\omega_0$ , and the corresponding undamped mode shape vector  $\mathbf{u}_\infty$  associated with fully rigid viscous dampers and governed by the modified eigenvalue problem

$$(\mathbf{K} - \omega_\infty^2 \mathbf{M}) \mathbf{u}_\infty = \mathbf{r} \quad (31)$$

with frequency  $\omega_\infty$ . In (31), the force vector  $\mathbf{r}$  contains the reaction forces from the rigid dampers on the structure. Following the procedure outlined in the paper of Main and Krenk,<sup>22</sup> the optimum viscous parameter for the hybrid damper is obtained by the relation

$$c_{opt} \omega |H(\omega)| = \frac{\omega_\infty^2 - \omega_0^2}{\gamma^2} \quad (32)$$

Here,  $|H(\omega)|$  is the amplitude of the transfer function given in (19), while

$$\gamma^2 = \mathbf{u}_0^T (\mathbf{W} \mathbf{W}^T) \mathbf{u}_0 \quad (33)$$

represents the sum of squares of the modal amplitudes over the individual damper connections when the undamped mode shape vector is scaled to unit modal mass, i.e.  $\mathbf{u}_0^T \mathbf{M} \mathbf{u}_0 = 1$ . With the relation between the filter parameters given as  $\omega_f = \tau_f \omega_0^2$ , the magnitude of the transfer function in (19) can be approximated as

$$|H(\omega)| \simeq \left| \frac{1}{1-\nu} \right| \quad (34)$$

assuming that the angular frequency is sufficiently close to the resonance frequency, i.e.  $\omega \simeq \omega_0$ . Substitution of (34) into (32) gives the optimum damping parameter

$$c_{opt} \simeq \frac{2(\omega_\infty - \omega_0)}{\gamma^2} |1 - \nu| \quad (35)$$

where the approximation  $(\omega_\infty^2 - \omega_0^2)/\omega \simeq 2(\omega_\infty - \omega_0)$  has been used. The fraction on the right-hand side of (35) corresponds to the optimum damping parameter for the pure viscous damper, while the final factor  $|1 - \nu|$  represents the correction because of the filtered IFF format. By choosing  $0 < \nu < 1$  for increased damper stroke, the magnitude of  $c_{opt}$ , and thereby the size of the viscous dashpots, is reduced accordingly.

In order for the tuning to be optimal for any orientation of the RNA, the expression in (35) should be independent with respect to the orientation of the RNA for a constant value of  $\nu$  and thereby perform identical for both the side–side mode and the fore–aft mode. In Figure 5, the total modal damper displacement  $\gamma$  defined in (33) is plotted as function of the RNA orientation defined by the angle  $\theta_2^1$  in Figure 4c. In Figure 5, the subscript *ss* refers to the side–side mode, while *fa* refers to the fore–aft mode. The three different curves are for an increasing number of dampers  $r = 2$  (dashed),  $r = 3$  (solid) and  $r = 5$  (dash dotted). In each configuration, the dampers are positioned symmetrically with respect to the circumferential direction, whereby the angle  $\Delta\theta_2 = \theta_2^{k+1} - \theta_2^k$  between two adjacent dampers is given as  $\Delta\theta_2 = 360^\circ/r$ . The angle  $\theta_2^1$  describes the orientation of the first damper. For two dampers, the value for  $\gamma$  varies as a function of the RNA orientation, while for three or more dampers,  $\gamma$  is constant and approximately the same for fore–aft and side–side vibration modes. Table I shows the undamped frequencies  $\omega_0$  and  $\omega_\infty$ , the damping ratio  $\zeta_{st}$  for the two modes and the optimum damper parameter  $c_{opt}$  for three dampers ( $r = 3$ ). For more than three dampers,  $\gamma$  is simply increased proportionally according to the number of dampers, whereby the optimum damper parameter  $c_{opt}$  is reduced according to (35). In a practical implementation, a sufficiently large number of dampers would be preferable because it reduces the size of each damper and it limits the local force impact on the tower wall from the individual damper. In the present beam model, all dampers are connected to the same dofs, and the tower therefore only experiences a single damper, representing the combined effect of all dampers through the force vector in (23). To keep the computations as simple as possible, only three dampers are included in the beam model. It is found that for three or more dampers in a symmetric circumferential configuration, the ratio of the optimum viscous parameter obtained from (35) for the fore–aft (*fa*) and side–side (*ss*) vibration modes is  $c_{opt,fa}/c_{opt,ss} = 1.02$ . Because this ratio is close to unity, the same size viscous dampers and filter parameters can be used for all hybrid dampers inside the tower. For the following simulations, the mean value  $c_{opt} = (c_{opt,ss} + c_{opt,fa})/2$  is used as the optimum damping parameter, and the corresponding mean frequency  $\omega_0 = (\omega_{0,ss} + \omega_{0,fa})/2$  is used to determine filter parameters for the controller.

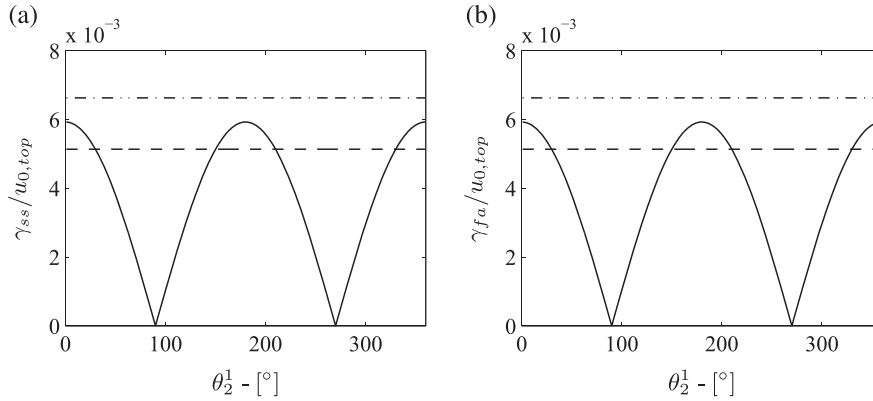


**Figure 5.** Modal damper displacement  $\gamma$  scaled by the modal tower top displacement  $u_{0,top}$  for (a) side–side and (b) fore–aft modes.

**Table I.** Modal properties for vibration modes and optimum damper values for three dampers with  $\nu = 0$ .

Mode	$\omega_0/(2\pi)$ [Hz]	$\omega_\infty/(2\pi)$ [Hz]	$\zeta_{st}$ [%]	$c_{opt}$ [Ns m <sup>-1</sup> ]
Side–side	0.2418	0.2481	1.15	$5.9 \cdot 10^9$
Fore–aft	0.2437	0.2501	1.15	$6.0 \cdot 10^9$

## 4. DAMPING OF WIND TURBINE TOWER VIBRATIONS

The performance of the hybrid damper configuration is now investigated. In the first part of this section, the wind turbine is assumed at standstill, and a root locus analysis, a frequency response analysis and a time transient analysis are conducted. In the final part, the performance of the hybrid damper is illustrated by simulations conducted in the commercial aeroelastic code Horizontal Axis Wind turbine simulation Code 2nd generation (HAWC2).<sup>23</sup> As discussed in the previous section, three hybrid dampers are installed symmetrically inside the tower, connected to the tower bottom and to the tower walls at 4 m above the bottom. Furthermore, in order for the damping to be independent of the particular orientation of the RNA, the same viscous parameter  $c$  and the same controller with filter parameters  $\nu$ ,  $\tau_f$  and  $\omega_f$  are assumed for all three hybrid dampers inside the tower.

### 4.1. Root locus analysis

The optimum tuning in (35) is based on an assumption that the trajectory of the root of the damped tower mode approximately follows a semicircle in the complex plane from the undamped frequency  $\omega_0$  to the undamped frequency  $\omega_\infty$  when the dampers are fully locked.<sup>22</sup> For this idealized semicircular trajectory, the corresponding maximum attainable damping ratio is given as

$$\zeta_{\max} = \frac{\omega_\infty - \omega_0}{\omega_\infty + \omega_0} \quad (36)$$

With respect to the wind turbine frequencies in Table I, the predicted maximum attainable damping ratio in (36) becomes  $\zeta_{\max}^{ss} = 0.0129$  for the side–side mode and  $\zeta_{\max}^{fa} = 0.0130$  for the fore–aft mode. To investigate the accuracy of the optimum tuning, the wind turbine with hybrid dampers installed is now investigated with respect to a root locus analysis. The system of governing equations in (27) is conveniently rewritten to state space format without external loading  $\mathbf{f} = \mathbf{0}$ ,

$$\frac{d}{dt} \begin{bmatrix} \mathbf{u} \\ \dot{\mathbf{u}} \\ \mathbf{q} \\ \dot{\mathbf{q}} \end{bmatrix} = \begin{bmatrix} \mathbf{0}_{uu} & \mathbf{I}_{uu} & \mathbf{0}_{uq} & \mathbf{0}_{uq} \\ -\mathbf{M}^{-1}\mathbf{K} & -\mathbf{M}^{-1}(\mathbf{C} + c\mathbf{W}\mathbf{W}^T) & \mathbf{0}_{uq} & c\mathbf{M}^{-1}\mathbf{W} \\ \mathbf{0}_{uq}^T & \mathbf{0}_{uq}^T & \mathbf{0}_{qq} & \mathbf{I}_{qq} \\ \mathbf{0}_{uq}^T & -\nu/\tau_f\mathbf{W}^T & -\omega_f/\tau_f\mathbf{I}_{qq} & -(1-\nu)/\tau_f\mathbf{I}_{qq} \end{bmatrix} \begin{bmatrix} \mathbf{u} \\ \dot{\mathbf{u}} \\ \mathbf{q} \\ \dot{\mathbf{q}} \end{bmatrix} \quad (37)$$

where  $\mathbf{0}$  and  $\mathbf{I}$  denote the zero and identity matrices, respectively, with subscripts  $u$  and  $q$  identifying the specific dimensions with reference to the number of components in the corresponding vectors  $\mathbf{u}$  and  $\mathbf{q}$ . The complex-valued natural frequencies  $\omega$  are determined directly from the eigenvalues  $i\omega$  of the system matrix in (37). The natural frequency can be written as

$$\omega = |\omega| \left( \sqrt{1 - \zeta^2} + i\zeta \right) \quad (38)$$

where the corresponding damping ratio is computed as

$$\zeta = \frac{\text{Im}[\omega]}{|\omega|} \quad (39)$$

Thus, the attainable damping ratio is seen to be closely related to the maximum of the imaginary part of the complex frequency.

Figure 6(a),(b) shows the trajectories of the complex natural frequency of the side–side and fore–aft vibration modes for an increasing value of the damping parameter  $c$ , a so-called root locus. The solid black curve is for  $\nu = 0$  and therefore represents the pure viscous case without actuator motion. The dashed black curve represents proportional intrinsic damping  $\zeta_{st} = 0.0115$ , with contributions from structural and soil damping as introduced in Section 3.1. Because the wind turbine is analyzed at standstill, aerodynamic damping is omitted in this initial analysis. The remaining three curves in the figure are for  $\nu = 0.9$  with  $\omega_f = \tau_f\omega_0^2 = \omega_0/8$  (blue), for  $\nu = 0.9$  with  $\omega_f = \tau_f\omega_0^2 = \omega_0$  (red) and for  $\nu = 0.975$  with  $\omega_f = \tau_f\omega_0^2 = \omega_0/8$  (green). The natural frequencies obtained from the eigenvalue analysis for  $c_{opt}$  in (35) are represented by the blue circles in the figure. The corresponding damping ratio determined by (39) is shown in Figure 6(c),(d). The proportional damping and the supplemental damping from the hybrid dampers are found to be approximately additive. For the pure viscous case (black solid), the trajectory accurately reproduces the expected semicircle, and the damping ratio at  $c_{opt}$  reproduces the estimated total maximum damping  $\zeta_{tot} \simeq \zeta_{st} + \zeta_{\max} \simeq 0.245$ . For increasing values of both the filter parameters and the gain value, the semicircular shape is distorted, and the attainable damping is consequently reduced. As seen from the damping ratio in Figure 6(c),(d), an increase in the filter and gain parameters implies that  $c_{opt}$  overestimates the actual optimum. The present results indicate that for gains  $\nu \leq 0.9$  and filter parameters  $\omega_f = \tau_f\omega_0^2 < \omega_0$ , the complex

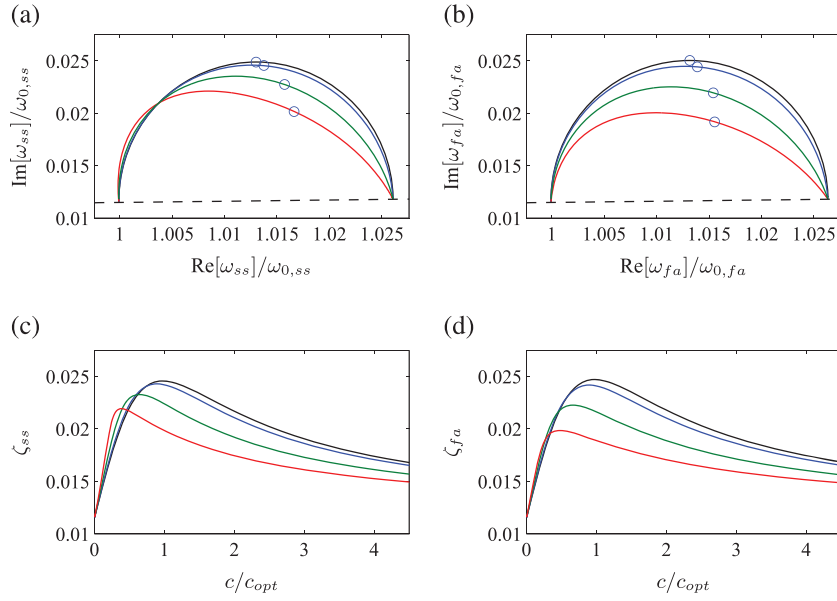


**Figure 6.** (a,b) Root locus plot and (c,d) damping ratio for increasing  $c$ , for side-side mode in (a,c) and fore-aft mode in (b,d). Damper parameters:  $\omega_f = \tau_f \omega_0^2 = \omega_0/8$  with  $\nu = 0$  (black),  $\nu = 0.9$  (blue) and  $\nu = 0.975$  (green) and  $\omega_f = \tau_f \omega_0^2 = \omega_0$  with  $\nu = 0.9$  (red).

trajectories approximately reproduces the desired semicircle of the pure viscous case, and  $c_{opt}$  gives a good estimate of the optimum damping parameter.

## 4.2. Frequency response analysis

In this section, the hybrid damper concept is investigated by a frequency response analysis, assuming harmonic solutions of the form

$$\mathbf{u} = \bar{\mathbf{u}} \exp i\omega t \quad , \quad \mathbf{q} = \bar{\mathbf{q}} \exp i\omega t \quad , \quad \mathbf{f} = \bar{\mathbf{f}} \exp i\omega t \quad (40)$$

with amplitudes denoted by a bar and with driving angular frequency  $\omega$ . Substituting (40) into the governing equations in (27) gives

$$\left( -\omega^2 \begin{bmatrix} \mathbf{M} & \mathbf{0} \\ \mathbf{0}^T & \tau_f \mathbf{I} \end{bmatrix} + i\omega \begin{bmatrix} \mathbf{C} + c\mathbf{W}\mathbf{W}^T & -c\mathbf{W} \\ \nu\mathbf{W}^T & (1-\nu)\mathbf{I} \end{bmatrix} + \begin{bmatrix} \mathbf{K} & \mathbf{0} \\ \mathbf{0}^T & \omega_f \mathbf{I} \end{bmatrix} \right) \begin{bmatrix} \bar{\mathbf{u}} \\ \bar{\mathbf{q}} \end{bmatrix} = \begin{bmatrix} \bar{\mathbf{f}} \\ \mathbf{0} \end{bmatrix} \quad (41)$$

from which the structural amplitudes  $\bar{\mathbf{u}}$  and actuator amplitudes  $\bar{\mathbf{q}}$  are determined for a given load amplitude  $\bar{\mathbf{f}}$ . The damper amplitudes  $\bar{u}_k$  are determined subsequently by (24),

$$\bar{u}_k = \mathbf{w}_k^T \bar{\mathbf{u}} \quad (42)$$

The wind turbine is loaded locally by a single force at MSL acting at an angle of  $45^\circ$  relative to the plane of the rotor, hereby representing a wave load misalignment with respect to the wind direction. The force vector can therefore be written as

$$\bar{\mathbf{f}} = f_0 \begin{bmatrix} 0, & \dots, & 1/\sqrt{2}, & 1/\sqrt{2}, & 0, & \dots, & 0 \end{bmatrix}^T \quad (43)$$

where  $f_0$  represents the magnitude of the external load.

Figure 7 shows the frequency response of the wind turbine and the hybrid damper for different gain values  $\nu = 0$  (black),  $\nu = 0.5$  (red) and  $\nu = 0.75$  (blue) and with filter parameters  $\omega_f = \tau_f \omega_0^2 = \omega_0/8$ . The curves are scaled by the corresponding static displacement  $w_{top}^0$  at the top of the wind turbine tower, whereby Figure 7(a) shows the dynamic amplification of the tower top. Since the natural frequency and damping of the two tower modes are almost identical, the response of the two modes will be in phase, and therefore, only the total response of the tower top is plotted in Figure 7(a), and as expected, the amplitude is the same for all three values for  $\nu$ . When the response is represented entirely by a single mode, the dynamic amplification factor at the resonance frequency is  $1/(2\zeta_{tot})$ . Assuming that the response of the wind turbine is a linear combination of the two tower modes, this can be used to estimate the damping ratio of the two modes with

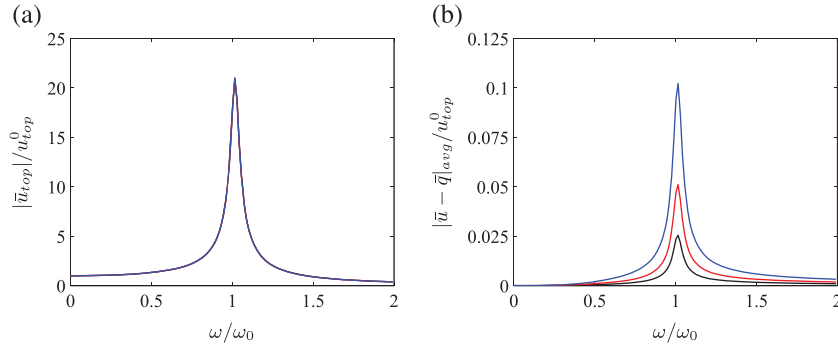


**Figure 7.** (a) Top floor and (b) damper displacement for  $\omega_f = \tau_f \omega_0 = \omega_0/8$  with  $\nu = 0.0$  (black), 0.5 (red) and 0.75 (blue).

the hybrid damper installed inside the tower. From the dynamic amplification of the tower top displacement in Figure 7(a), the damping ratio is estimated to be  $\zeta_{tot} = 0.0238$ , which corresponds fairly well with the damping ratio  $\zeta_{tot} = 0.0245$  predicted by the root loci in Figure 6. Figure 7(b) shows the average of the individual displacement amplitudes over the three dampers, which is constant for any orientation of the RNA, as shown in Figure 5. It is seen that the damper displacement in Figure 7(b) is increased significantly as  $\nu \rightarrow 1$ , which is in agreement with the expression in (10).

### 4.3. Time transient analysis and actuator drift

Drift of the actuator displacement may arise because of errors in the force measurements. An error in the force measurement will for the IFF controller correspond to adding an additional force term  $f_e$  on the right-hand side of equation 2, which by insertion of the damper force from (1) takes the form

$$\dot{q}(t) = -\nu(\dot{u}(t) - \dot{q}(t)) - g f_e(t) \quad (44)$$

The actuator displacement at time  $t_1$  can be determined by time integration as

$$q(t_1) = -\frac{\nu}{1-\nu} u(t_1) - \frac{g}{1-\nu} \int_0^{t_1} f_e(t) dt \quad (45)$$

The force error  $f_e$  is seen to lead to drift of the actuator displacement, and in particular, a constant force error will lead to constant increase in the drift. If the drift leads to saturation of the actuator signal, this may cause a significant reduction in the performance of the hybrid damper. The filtered time integration presented in Section 2.2 is introduced in order to avoid drift in the actuator signal, because of errors in the measured force feedback signal. To investigate the effect of the filtered integration, the hybrid damper concept is now analyzed by solving the closed-loop system of equation in (27) to obtain the time transient response when the wind turbine is loaded by a wave load at MSL. Furthermore, a force offset is included to represent a signal error locally in the feedback control loop of the third hybrid damper. The load consists of a wave train of three regular sine waves with realistic wave period  $T_w = 10$  s, whereafter the force drops to zero. The period  $T_w$  corresponds approximately to 0.4 wave periods per vibration period of the wind turbine. As in the previous example, the misaligned wave load acts at an angle of  $45^\circ$  relative to the rotor direction. The load vector is therefore given as

$$\mathbf{f}(t) = p(t) \left[ 0, \dots, 1/\sqrt{2}, 1/\sqrt{2}, 0, \dots, 0 \right]^T \quad (46)$$

where the time dependence of the load intensity  $p(t)$  is introduced as

$$\frac{p(t)}{f_0} = \begin{cases} \sin(2\pi t/T_w), & t \leq 3T_w \\ 0, & t > 3T_w \end{cases} \quad (47)$$

where  $f_0$  is the force amplitude. The constant offset error signal  $f_e = f_0/200$  is included in the feedback signal to the force feedback control of the third damper by simply adding the force term  $-g f_e$  to the right-hand side of the bottom equation in (27). The force error is only applied during the first three wave periods  $3T_w$  when the aforementioned wave train passes the wind turbine. For  $t > 3T_w$ , the offset error in the force signal is removed, i.e.  $f_e = 0$ .

Figure 8 shows the time-dependent response of the hybrid damper and wind turbine for  $\nu = 0.5$  and  $\omega_f = \tau_f = 0.0$  with error (blue) and without error (black) in the feedback signal and for  $\omega_f = \tau_f \omega_0^2 = \omega_0/8$  with error in the feedback

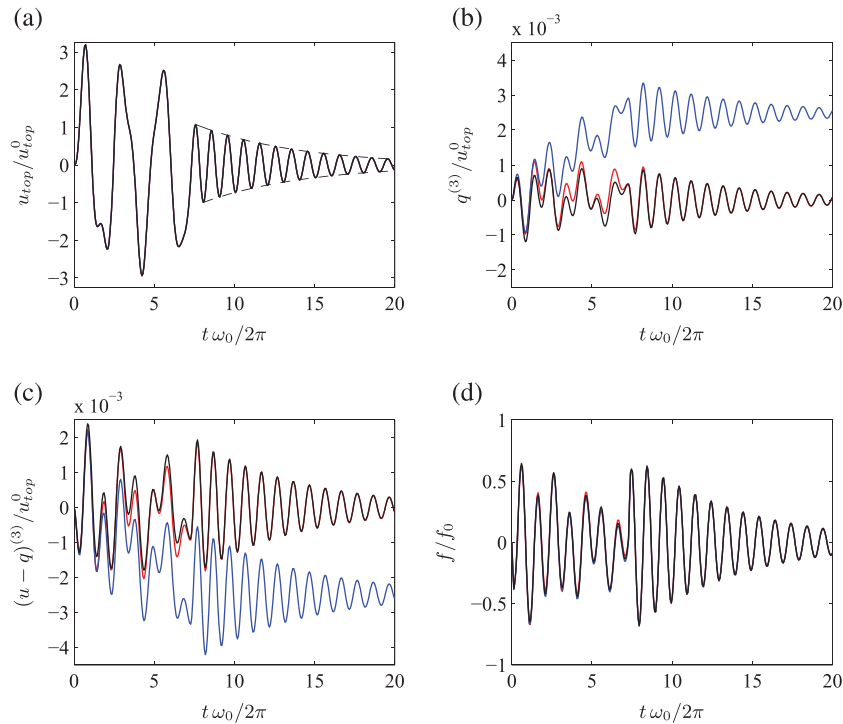


**Figure 8.** (a) Tower top displacement, (b) actuator displacement, (c) displacement of viscous dashpot and (d) damper force. The three curves represent  $\nu = 0.5$  and  $\omega_f = \tau_f = 0.0$  with error feedback signal (blue) and without error feedback signal (black) and with  $\omega_f = \tau_f \omega_0^2 = 0.125$  and error feedback signal (red).

signal (red). In Figure 8(a), the total displacement of the tower top is plotted. The response of the three simulations is seen to be practically identical, and by use of an exponential fit (indicated by the dashed curve), the apparent damping ratio is estimated to be  $\zeta_{tot} = 0.0248$ . This is in agreement with the damping ratios determined from both the root locus analysis in Section 4.1 and the frequency response analysis in Section 4.2. The actuator displacement of the third hybrid damper  $q^{(3)}$  is plotted in Figure 8(b). The actuator displacement is seen to have a linear drift during the wave train when an error is included in the feedback signal (blue) compared with the reference case with no errors in the signal (black). After the wave train has passed and the error signal is removed, the offset in  $q^{(3)}$  is constant. For the case with an error in the feedback signal and filtered integration (red), the offset of the actuator displacement is significantly reduced. Figure 8(c) shows the displacement of the viscous dashpot for the third hybrid damper  $(u - q)^{(3)}$ . The amplitude across the viscous dashpot is amplified to approximately twice the amplitude of the actuator displacement for the gain  $\nu = 0.5$ . Finally, Figure 8(d) shows the three damper force histories for the third hybrid damper  $f^{(3)}$  with error signal. As expected, the damper force is very similar for all the three simulations and therefore not influenced by the drift in the actuator motion. In the first part of the simulation, when the wind turbine is vibrating in a forced response, the damper force amplitude is small compared with the displacement response of the wind turbine in Figure 8(a), and it is of more irregular type. In the subsequent free vibration part, the damper force immediately increases, followed by a harmonically decaying response.

#### 4.4. Time transient simulations in HAWC2

Aerodynamic damping is the dominant damping component for the fore–aft vibrations in the rotor direction (y-axis) during operations of a wind turbine, while the associated side–side vibrations in the rotor plane direction (x-axis) are very lightly damped and therefore the target of the hybrid damper system. In the previous analysis, where the wind turbine is modeled by simple beam elements, the aerodynamic effects are omitted. To investigate the effect of aerodynamic damping, the time response simulations are now carried out using the dedicated aeroelastic code HAWC2, introduced in the user manual.<sup>23</sup> The HAWC2 code is developed at DTU Wind Energy and used for both industrial applications and research projects. The code includes a multibody formulation for modeling of the nonlinear structural dynamics and a so-called Stig Øye model for the aerodynamic modeling of the blades. Thus, the use of HAWC2 allows for very realistic dynamic simulations of wind turbines during operations and not only at standstill, as in the previous analysis in this section. The model used for

the simulations is downloaded from the HAWC2 webpage,<sup>24</sup> and this model is equivalent to that used in the Offshore Code Comparison Collaboration study.<sup>19</sup>

The wind turbine is loaded by a mean wind speed of  $8 \text{ m s}^{-1}$ , with zero turbulence intensity and a wind shear profile with power law exponent 0.14. The aerodynamic forces on the blades are computed using a blade element momentum model and aerodynamic drag on the tower, and nacelle is included as well. Soil and structural damping is tuned to give a critical damping ratio of  $\zeta_{st} = 0.0115$  for the two lowest tower (side–side and fore–aft) modes, which is identical to the linear beam model used in the previous part of this section. In HAWC2, the hybrid dampers are effectively implemented using an external dynamic link library, as explained in the paper of Hansen and Larsen<sup>25</sup> for an advanced dynamic gear model. In addition to the wind load, the wind turbine is also loaded by a wave train identical to the wave loading in the previous example, whereby the fore–aft mode and the side–side mode are simultaneously excited with equal magnitude. When increasing the misalignment of the wave train relative to the wind direction, the excitation of the lightly damped side–side mode will increase as well, resulting in larger vibration amplitudes. Thus, the magnitude of the displacement amplitudes presented in this section depends on the specific angle of misalignment because of the large aerodynamic damping in the fore–aft direction. The wave train is applied sufficiently long time after simulation start-up so that any initial transient response from the wind load has disappeared. Simulations are conducted for three cases: (i) without dampers, (ii) with three viscous dampers and (iii) with three hybrid dampers installed inside the tower. For the hybrid dampers, the gain parameter  $\nu = 0.75$  and the filter parameters  $\omega_f = \tau_f \omega_0^2 = \omega_0/8$  have been used.

In the HAWC2 model, the  $x$ -direction represents the in-plane direction and is therefore associated with the lightly damped side–side vibrations, while the corresponding  $y$ -direction represents the fore–aft vibration form. As seen in Figure 9(a), vibrations in the  $y$ -direction are damped much faster than the corresponding vibrations in the  $x$ -direction. This is due to the additional aerodynamic damping in the rotor direction. Without dampers, the effective damping ratio for the fore–aft vibrations is estimated from vibration decay to  $\zeta_{tot} = 0.1123$ , while this value increases to  $\zeta_{tot} = 0.1267$  in the case with hybrid or viscous dampers. These values are significantly higher than the values from the previous standstill simulations because of the presence of aerodynamic damping. For the side–side vibrations, the damping ratio is similarly estimated to  $\zeta_{tot} = 0.0122$  for the case without supplemental dampers, while it increases to  $\zeta_{tot} = 0.0264$  with dampers, which is slightly larger than the values obtained previously from the simulations at standstill. This increase could be due to modal interaction with the fore–aft mode, which has a significantly larger modal damping.

The additional damping from the supplemental dampers is obtained from the total damping ratios, by subtracting the values obtained from the simulations without dampers. This gives additional damping ratios of  $\zeta_{fa} = 0.0144$  for the

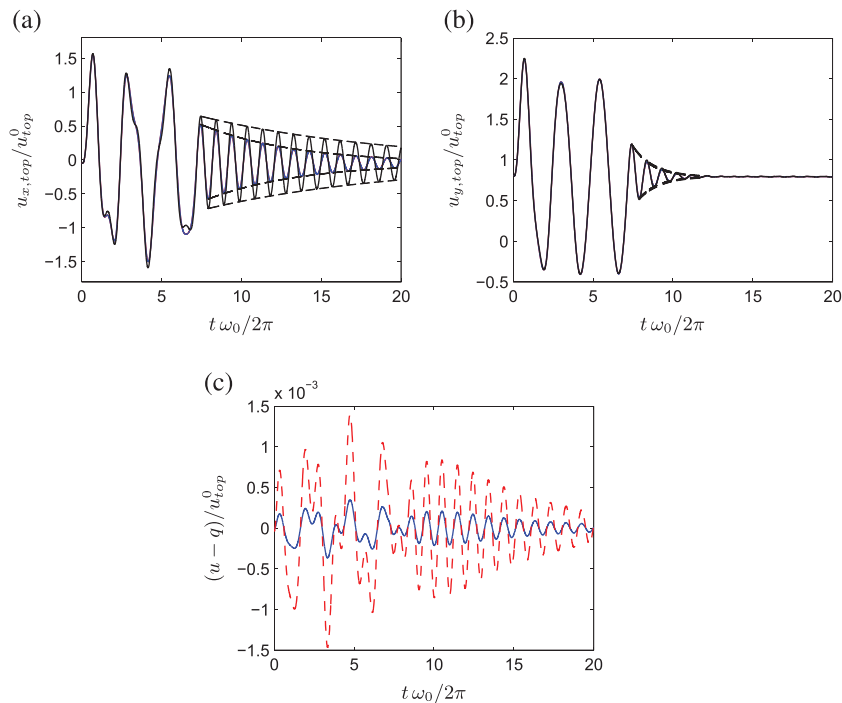


**Figure 9.** Tower top displacement in  $x$ -direction (a) and  $y$ -direction (b), and (c) displacement over the viscous dashpot for  $\nu = 0$  (blue) and for  $\nu = 0.75$  (red) with  $\omega_f = \tau_f \omega_0^2 = \omega_0/8$  and without dampers (black).

fore–aft vibrations and  $\zeta_{ss} = 0.0142$  for the side–side vibrations. These values are slightly larger than the expected value  $\zeta_{\max} = 0.013$  obtained from the previous analysis. These higher damping values are likely due to changes in the vibration form of the structure during operation caused by the insertion of dampers at the bottom of the tower. The modified vibration form causes increased soil and aerodynamic damping, which is added to the additional damping from the supplemental dampers. Thus, the present simulations conducted in HAWC2 show that the performance of the hybrid damper concept is unaffected by aerodynamic damping and that inherent and supplemental damping values are approximately additive, also during operation of the wind turbine. Finally, in Figure 9(c), the displacement over the viscous damper element in the hybrid damper is plotted. When comparing the pure viscous case with the hybrid damper using  $\nu = 0.75$ , the displacement across the damper is amplified by approximately a factor of 4, which again agrees with the theoretical predictions from the expression in (10).

#### 4.5. Fatigue analysis in HAWC2

A 3 h wave load record is now prepared and applied to the offshore wind turbine in HAWC2. The wind conditions are identical to those for the transient analysis in Section 4.4, which means that the wind is without turbulence and therefore only introduces a wind pressure in the  $y$ -direction and aerodynamic effects. The wave loading is generated as a 3 h (10,800 s) realization of a common Pierson–Moskowitz spectrum, with a peak frequency of 0.1 Hz and significant wave height of 6 m.<sup>19</sup> The wave load is again applied with a misalignment angle of  $45^\circ$  relative to the  $x$ -axis, whereby the fore–aft and side–side directions receive the same force components. Thus, the wave loading introduces the only stochastic loading on the structure. The reduction of the extreme response and accumulated damage due to the presence of the active damper system are investigated in this section. The simulations in HAWC2 with and without damper system are conducted for the same seed in the realization of the wave loading, whereby the time histories for the damped response are directly comparable with those without damper system.

Figure 10(a) shows the time response histories of the top tower position  $u_{x,top}$  in the side–side  $x$ -direction and the base bending moment  $M_{y,base}$  around the  $y$ -axis at the bottom of the tower. The time  $t$  is again normalized by the natural frequency  $\omega_0/(2\pi) = 0.2418$  Hz, and it is seen that the length of the time records in the figure corresponds to around 2600 vibration periods. The response of the wind turbine without damper is represented by the gray curve in the background, while the red curve in the front shows the damped response with  $\nu = 0.75$  and  $\omega_f = \tau_f \omega_0^2 = \omega_0/8$ . The black dashed horizontal line indicates the (common) mean value, while the gray and red dashed lines represent the corresponding standard deviations. The maximum deflections and bending moments are indicated in the figure by the asterisk markers. It is seen that the top tower deflection is only reduced slightly by the hybrid damper system, with a reduction in maximum deflection

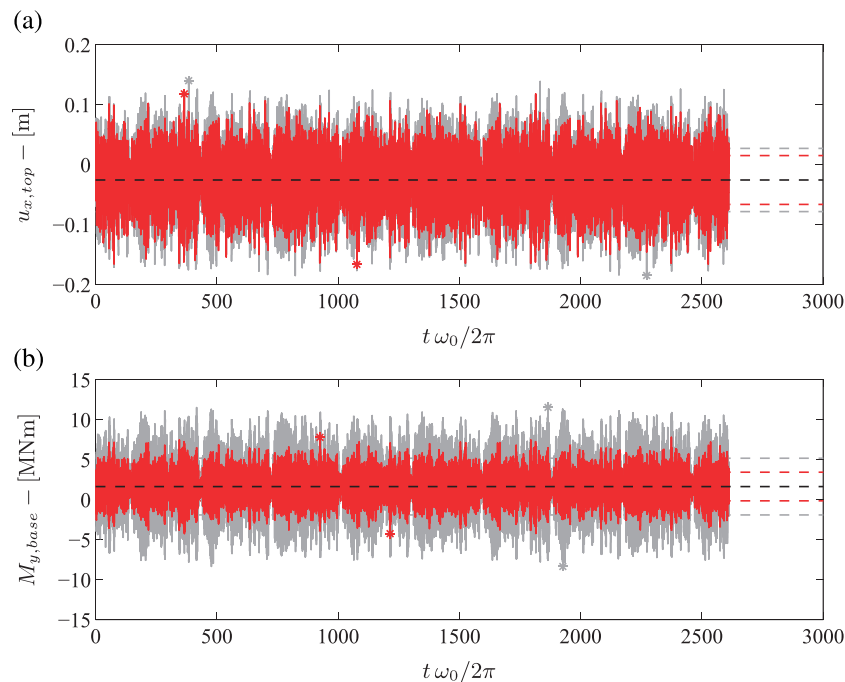


**Figure 10.** Tower top position in side–side  $x$ -direction (a) and base moment around  $y$ -axis (b).

(relative to mean) of 13% and a corresponding reduction in standard deviation of 23%. The reduction in the base moment at the bottom of the tower is significantly larger. The maximum bending moment (relative to mean) is reduced by 38% because of the presence of the hybrid damper system, while the standard deviation of the base moment is reduced by 49%.

A fatigue analysis is conducted based on the irregular response of the wind turbine tower using the rainflow counting procedure described in Madsen and colleagues.<sup>26</sup> Typically (normal) stress cycles are detected and accumulated. However, in the present case, the base bending moment  $M_{y,base}$  is used directly in the fatigue analysis. A standard rainflow counting procedure is applied to generate moment increments  $\Delta M_j$  from the base bending moment record associated. The accumulated damage  $D_M$  is then estimated from the summation

$$D = \sum_{j=1}^N \frac{\Delta M_j^m}{K} \quad (48)$$

with power law exponent  $m$  and constant  $K$ .<sup>26</sup> The present results for the damage are normalized by the constant  $K$ , and an exponent of  $m = 3$  is assumed. In the case without damper, the rainflow counting procedure detects  $N_0 = 3475$  cycles, while in the damped case, this number is reduced to  $N_d = 2313$ , which indicates that the damped response is significantly more regular than the undamped case. The accumulate damage without damper system is denoted  $D_0$ , while  $D_d$  in the damped case. The accumulated damage ratio is obtained as  $D_d/D_0 = 0.13$ , while a corresponding damage ratio, corrected with respect to the individual number of cycles, is determined as  $(D_d N_0)/(D_0 N_d) = 0.20$ . Both damage ratios indicate that the hybrid damper system proposed in the present paper is able to reduce the accumulate damage and thereby increase the fatigue life of the offshore wind turbine.

## 5. CONCLUSION

Damping of wind turbine tower vibrations due to misaligned wave loading is expected to be critical for the feasibility of the monopile support structure to be used for future offshore wind turbines at larger water depths. The present paper presents a novel solution for damping of tower vibrations, where viscous hybrid dampers are installed at the bottom of the wind turbine tower. In the hybrid damper concept, the actuator uses an IFF scheme for amplifying the displacement over the viscous dashpot element and thereby significantly increasing the feasibility of installing dampers at the bottom of the tower. In this pure IFF format, attainable damping is fully equivalent to the attainable damping of a passive viscous dashpot, and the optimum damping parameter may therefore be determined by appropriate scaling of the corresponding optimum damping parameter for the pure passive case obtained by the results in the paper of Main and Krenk.<sup>22</sup> To avoid drift in the actuator displacement, e.g. due to errors in the force measurements, a filtered integration of the actuator velocity is introduced. It is demonstrated through numerical examples that this filtering can significantly reduce the drift without notable loss of the damping performance. For large values of the filter parameters or gain values in the IFF controller, a reduction in attainable damping is found, which therefore limits the potential amplification of the damper displacement. It is found that with filter parameter values  $\omega_f = \tau_f \omega_0^2 = \omega_0/8$  and gain values  $\nu = 0.5-0.9$ , the associated amplification factor ranges from 2 to 10, while the attainable damping is approximately similar to that obtained by the pure passive viscous case. In the numerical simulations, the 5 MW offshore reference wind turbine from the Offshore Code Comparison Collaboration study<sup>19</sup> is considered. For this model, it is demonstrated that when several hybrid dampers are installed in a symmetric circumferential layout, the same size of dampers and filter parameters for each damper may be used without significant decrease in performance. Thus, the present damping configuration is sufficiently independent of the direction of the RNA. Furthermore, the simulations show that by placing hybrid dampers in a symmetric layout connected to the tower wall at the bottom of the tower and 4 m above the bottom, a damping ratio of approximately  $\zeta = 0.0125$  is achievable in both of the two lowest critical tower modes. Finally, a fatigue analysis is conducted in HAWC2, using irregular wave loading, which shows that the hybrid damper system reduces the accumulated damage in the wind turbine tower. The damping of the fore-aft and side-side vibration modes of the wind turbine might also affect other important vibration problems. For example, the present concept might introduce supplemental damping to the lightly damped edgewise vibration modes of the rotor, which are coupled to the side-side tower motions.<sup>27</sup> Furthermore, the present approach could also be effective in damping of the vibrations induced by voltage sag because of, e.g. grid fault.<sup>28,29</sup>

## ACKNOWLEDGEMENTS

This work has been supported by the Danish Energy Agency and Vestas Wind Systems A/S under the EUDP project 'Monopile cost reduction and demonstration by joint applied research'.

## REFERENCES

1. Tarp-Johansen NJ, Andersen L, Christensen ED, Mørch C, Kallesøe B, Frandsen S. Comparing sources of damping of cross-wind motion. *Proceedings of the european wind energy conference & exhibition*, Stockholm, Sweden, 2009.
2. Damgaard M, Ibsen LB, Andersen LV, Andersen JKF. Cross-wind modal properties of offshore wind turbines identified by full scale testing. *Journal of Wind Engineering and Industrial Aerodynamics* 2013; **116**: 94–108.
3. Murtagh PJ, Ghosh A, Basu B, Broderick BM. Passive control of wind turbine vibrations including blade/tower interaction and rotationally sampled turbulence. *Wind energy* 2008; **11**: 305–317.
4. Colwell S, Basu B. Tuned liquid column dampers in offshore wind turbines for structural control. *Engineering Structures* 2009; **31**: 358–368.
5. Lackner MA, Rotea MA. Passive structural control of offshore wind turbines. *Wind energy* 2011; **14**: 373–388.
6. Stewart GM, Lackner MA. The impact of passive tuned mass dampers and wind–wave misalignment on offshore wind turbine loads. *Engineering Structures* 2014; **73**: 54–61.
7. Dinh VN, Basu B. Passive control of floating offshore wind turbine nacelle and spar vibrations by multiple tuned mass dampers. *Structural Control and Health Monitoring* 2015; **22**: 152–176.
8. Stol KA, Zhao W, Wright AD. Individual blade pitch control for the Controls Advanced Research Turbine (CART). *Journal of solar energy engineering* 2006; **128**: 498–505.
9. Fischer T, Rainey P, Bossanyi E, Kühn M. Study on control concepts suitable for mitigation of loads from misaligned wind and waves on offshore wind turbines supported on monopiles. *Wind Engineering* 2011; **35**: 561–574.
10. Brodersen ML, Høgsberg J. Damping of offshore wind turbine tower vibrations by a stroke amplifying brace. *Energy Procedia* 2014; **53**: 258–267.
11. Tsouroukdissian AR. *System and Method for Damping Vibrations in a Wind Turbine*. US Patent 8,641,369, 2014.
12. Høgsberg J, Brodersen ML. Hybrid viscous damper with filtered integral force feedback control. *Journal of Vibration and Control* 2014, DOI: 10.1177/1077546314543912.
13. Preumont A, Dufour JP, Malekian C. Active damping by a local force feedback with piezoelectric actuators. *Journal of guidance, control, and dynamics* 1992; **15**: 390–395.
14. Preumont A. *Vibration Control of Active Structures: An Introduction. Third Edition*. Springer Verlag: Berlin, 2011.
15. Achkire Y, Preumont A. Active tendon control of cable-stayed bridges. *Earthquake Engineering & Structural Dynamics* 2001; **30**(7): 961–979.
16. Bossens F, Preumont A. Active tendon control of cable-stayed bridges: a large-scale demonstration. *Earthquake engineering & structural dynamics* 2001; **30**: 961–979.
17. Preumont A, Achkire Y, Bossens F. Active tendon control of large trusses. *AIAA journal* 2000; **38**: 493–498.
18. Høgsberg JR, Krenk S. Linear control strategies for damping of flexible structures. *Journal of Sound and Vibration* 2006; **293**: 59–77.
19. Jonkman J, Musial W. *Offshore code comparison collaboration (OC3) for IEA task 23 offshore wind technology and deployment*, Technical Report National Renewable Energy Laboratory, 2010. NREL/TP-500-48191.
20. Krenk S. A general format for curved and non-homogeneous beam elements. *Computers & structures* 1994; **50**: 449–454.
21. Hahn W, Baartz AP. *Stability of Motion*, Vol. 422. Springer: Berlin, 1967.
22. Main JA, Krenk S. Efficiency and tuning of viscous dampers on discrete systems. *Journal of Sound and Vibration* 2005; **s286**: 97–122.
23. Larsen TJ, Hansen AM. *How 2 HAWC2, The User's Manual*. Risø National Laboratory: Roskilde, 2007.
24. *Phase II, extended monopile*. Available: <http://www.hawc2.dk/HAWC2%20Download/HAWC2%20model.aspx> (Accessed: 04-01-2015).
25. Hansen AM, Larsen TJ. Gear dynamics. *Research in Aeroelasticity EFP-2007-II, 1698(EN)*. Risø National Laboratory, Roskilde, 2009; 134–142.
26. Madsen HO, Krenk S, Lind NC. *Methods of Structural Safety*. Dover Publications: New York, 2006.
27. Hansen MH. Aeroelastic instability problems for wind turbines. *Wind energy* 2007; **10**: 551–577.
28. Fadaeinedjad R, Moschopoulos G, Moallem M. Investigation of voltage sag impact on wind turbine tower vibrations. *Wind energy* 2008; **11**: 351–375.
29. Basu B, Staino A, Basu M. Role of flexible alternating current transmission systems devices in mitigating grid fault-induced vibration of wind turbines. *Wind energy* 2014; **17**: 1017–1033.



# P3

Active Tuned Mass Damper  
for damping of offshore wind turbine vibrations

Mark L. Brodersen, Ann-Sofie Bjørke, Jan Høgsberg

*Wind Energy*,  
(submitted)

# Active Tuned Mass Damper for damping of offshore wind turbine vibrations

Mark L. Brodersen<sup>1,2</sup>, Ann-Sofie Bjørke<sup>1,2</sup> and Jan Høgsberg<sup>1</sup>

<sup>1</sup>Department of Mechanical Engineering, Technical University of Denmark, DK-2800 Kgs. Lyngby, Denmark

<sup>2</sup>National Oilwell Varco Denmark I/S, Priorparken 480, DK-2605 Brøndby, Denmark

## ABSTRACT

An Active Tuned Mass Damper (ATMD) is employed for damping of tower vibrations of fixed offshore wind turbines, where the additional actuator force is controlled using feedback from the tower displacement and the relative velocity of the damper mass. An optimum tuning procedure equivalent to the tuning procedure of the passive Tuned Mass Damper (TMD) combined with a simple procedure for minimizing the control force is employed for determination of optimum damper parameters and feedback gain values. With time simulations in the aeroelastic code HAWC2 it is demonstrated how the ATMD can be used to further reduce the structural response of the wind turbine compared to the passive TMD and without an increase in damper mass. A limiting factor for the design of the ATMD is the displacement of the damper mass, which for the ATMD increases to compensate for the reduction in mass. Copyright © 0000 John Wiley & Sons, Ltd.

## KEYWORDS

Offshore wind turbine; Monopile; Tower vibrations; Active Tuned Mass Damper; Vibration control

## Correspondence

Mark L. Brodersen, National Oilwell Varco Denmark I/S, Priorparken 480, DK-2605 Brøndby, Denmark.

E-mail: MarkLaier.Brodersen@nov.com

Received . . .

## 1. INTRODUCTION

The monopile support is present day by far the most used support structure for offshore wind turbines, primarily due to its simple design. The design is relatively cost-effective compared to for example a jacket structure, though also quite sensitive to wave loading. Dimensioning of the monopiles are usually dictated by the fatigue loads, caused by wind and waves exciting primarily a combination of the two lowest tower modes, the fore-aft mode in the rotor direction and the side-side mode lateral to the rotor direction, where especially waves acting with an angle to the wind can cause large fatigue damage due to the absence of the aerodynamic damping in the direction lateral to the wind [1, 2, 3]. The future will see an increasing number of larger and more slender wind turbines positioned at deeper water depths [4]. For these structures the natural frequencies of the critical tower modes will be lower than for present day wind turbine structures, which will cause fatigue damage due to resonant wave loading to increase significantly. One way to decrease fatigue damage due to wave loading, and thereby increase the feasibility of the monopile support, would be to install external dampers.

So far research on the use of external dampers for fixed offshore wind turbines has focused mainly on passive concepts, with most focus on Dynamic Vibration Absorber (DVA) concepts, such as a Tuned Liquid Column Damper (TLCD) or a Tuned Mass Damper (TMD). Some of the pioneering work concerning applications in wind turbines includes the article by Colwell and Basu [5] in which the damping effect of a TLCD installed in an offshore wind turbine has been investigated by assuming correlated wind and wave load conditions. More recently, attention has focused on how to address the absence of aerodynamic damping in the side-side direction, when significant wind-wave misalignment is present, e.g. in the work by Stewart and Lackner [6] where the beneficial effect of a TMD in reducing the tower base moment is demonstrated through numerical simulations, and where in particular a significant reduction in the side-side moment has been reported. In order for a DVA to be effective it needs to be installed where the amplitude of the critical tower mode is largest, which for the wind turbine is at the top of the tower or in the nacelle. Effective damping by a DVA is furthermore associated with large damper mass, which constitutes a major limitation, since additional mass is highly undesirable at the top of the wind turbine.

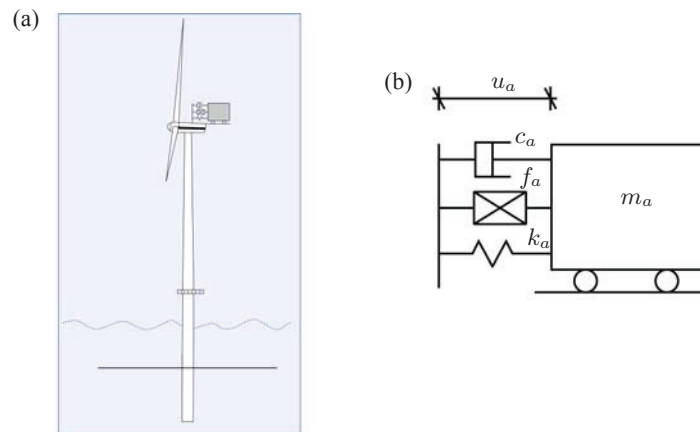


Figure 1. (a) Fixed offshore wind turbine with (b) ATMD.

The Active Tuned Mass Damper (ATMD) is a hybrid device consisting of a passive TMD supplemented by an actuator parallel to the spring and damper. It is a well known concept in structural control, especially for mitigation of excessive dynamic response of high-rise buildings subjected to strong wind and earthquake loads, where the ATMD has been proven to yield enhanced damping performance compared to the passive TMD [7, 8]. The concept has also seen physical implementation in a number of high-rise buildings in Japan [9]. For optimal feedback control of the ATMD, different strategies have been proposed. Chang and Soong [10] proposed a state feedback scheme combined with a Linear Quadratic Regulator determined by minimizing both the primary structural response and the control effort, Chang and Yang [11] assumed a white noise excitation and used a complete feedback scheme in which the optimum gain parameters is determined from a minimization of the response variance, while Nishimura [12] proposed a pure acceleration feedback format in which the optimum gain is determined by a dynamic amplification analysis similar to that of the passive TMD. As demonstrated in [12], for a single degree of freedom (dof) system this acceleration feedback scheme provides a reduction of the dynamic amplification of the primary mass compared to the TMD, but for the same damper mass and without any increase in the maximum dynamic amplification of the damper mass. However, for a flexible structure with a sufficiently large number of dofs this scheme contains an inherent instability as the mass matrix becomes indefinite in the high-frequency limit, which makes it unfeasible for practical implementation.

The present paper applies the ATMD concept for damping of wind turbine tower vibrations in order to overcome the limitations of the passive TMD. A simple feedback format that can provide guaranteed stability also for a flexible structure with multiple dofs is proposed in Section 2. By assuming a modal representation for the critical tower mode as in Section 2.1 the tuning procedure can be carried out for the reduced 2 dof system. Applying a dynamic amplification tuning procedure similar to that of the TMD combined with a tuning strategy for reduction of the active control energy optimal parameters are determined that both give an increased damping performance compared to the passive TMD, but for the same damper mass, and also reduces the used active control energy, as explained in Sections 2.2-2.4. In Section 3 the performance of the proposed ATMD damper format is investigated for damping of wind turbine tower vibrations by the use of comprehensive time simulations of a 5 MW offshore reference turbine conducted in the advanced aeroelastic code HAWC2 [13]. In order to compute the optimum damper parameters modal parameters of the critical tower modes are determined from the free decay response in Section 3.1. Next in Sections 3.2-3.3 it is demonstrated through both a frequency and a time transient response analysis that compared to the passive TMD the present ATMD can further reduce the response of the wind turbine, without increasing the damper mass.

## 2. MODELING OF ACTIVE TUNED MASS DAMPER

A fixed offshore wind turbine structure with an Active Tuned Mass Damper (ATMD) is illustrated in figure 1(a). The ATMD is positioned at the top of the wind turbine, where the amplitude of the critical tower modes are expected to be largest. In the initial design process, the wind turbine structure is assumed to be undamped and described by a linear discrete model with mass matrix  $\mathbf{M}$  and stiffness matrix  $\mathbf{K}$ . This is a fairly valid assumption since the critical tower modes are nearly unaffected by the rotations of the blades and since the modes have very low damping. Referring to figure 1(b) the ATMD exerts a force  $f = c_a \dot{u}_a + k_a u_a - f_a$  on the tower, where  $u_a$  is the relative displacement of the damper mass. Hereby the equation of motion (eom) for the structural degrees of freedom (dofs) of the wind turbine in  $\mathbf{u}$  can be written

as

$$\mathbf{M}\ddot{\mathbf{u}} + \mathbf{K}\mathbf{u} = \mathbf{f} + \mathbf{w}(c_a\dot{u}_a + k_a u_a - f_a). \quad (1)$$

In this equation the vector  $\mathbf{f}$  represents external loading, while the connectivity vector  $\mathbf{w}$  defines the connection of the ATMD to the tower. The connectivity vector  $\mathbf{w}$  will contain zeros except for the unit value at the dof, at which the ATMD is attached. The displacement of the tower at the location of the ATMD is therefore given by  $\mathbf{w}^T \mathbf{u}$ , whereby the eom for the ATMD is given as

$$m_a \ddot{u}_a + c_a \dot{u}_a + k_a u_a = -m_a \mathbf{w}^T \ddot{\mathbf{u}} + f_a. \quad (2)$$

Inserting (2) into (1) gives the more convenient format of the structural eom

$$(\mathbf{M} + \mathbf{M}_a)\ddot{\mathbf{u}} + \mathbf{K}\mathbf{u} = \mathbf{f} - m_a \mathbf{w} \ddot{u}_a, \quad (3)$$

where  $\mathbf{M} + \mathbf{M}_a = \mathbf{M} + \mathbf{w}\mathbf{w}^T m_a$  is the original mass matrix plus the additional mass of the ATMD. The equation system in (3) together with equation (2) constitutes the eoms for the wind turbine with an ATMD. By observing the two equations the closed-loop characteristics are described by  $-m_a \mathbf{w}^T \ddot{\mathbf{u}}$  as an input term in (2) and by  $-m_a \mathbf{w} \ddot{u}_a$  as a corresponding output term acting as a force on the wind turbine structure in (3). The active element of the ATMD exerts a control force  $f_a$ , which can be used to increase the input force to the external damper system, whereby the output force to the wind turbine is increased as well, so that the overall damping performance can be improved. In the present article the absolute displacement  $\mathbf{w}^T \mathbf{u}$  of the tower and the relative velocity  $\dot{u}_a$  of the damper mass are used as sensor signals in the feedback control. Hereby the actuator force is given by

$$f_a = -G_k \mathbf{w}^T \mathbf{u} - g_c c_a \dot{u}_a, \quad (4)$$

where  $G_k$  is the gain associated with the absolute displacement of the tower, while  $g_c$  is the non-dimensional gain associated with feedback of the relative velocity of the damper mass. The feedback gain  $G_k$  therefore corresponds to an increased input force to the external damper system, while the gain  $g_c$  corresponds to added damping. The displacement  $\mathbf{w}^T \mathbf{u}$  of the tower might be derived from high-precision GPS measurements as in [14, 15], while the relative velocity of the damper mass  $\dot{u}_a$  could be derived from the corresponding relative displacement and acceleration signals using a so-called kinematic Kalman filter [16, 17]. Inserting (4) into equations (3) and (2) provides the closed-loop system of equations for the wind turbine and ATMD as

$$\begin{aligned} \begin{bmatrix} \mathbf{M} + \mathbf{M}_a & \mathbf{w}m_a \\ m_a \mathbf{w}^T & m_a \end{bmatrix} \begin{bmatrix} \ddot{\mathbf{u}}(t) \\ \ddot{u}_a(t) \end{bmatrix} + \begin{bmatrix} \mathbf{0}\mathbf{0}^T & \mathbf{0} \\ \mathbf{0}^T & (1 + g_c)c_a \end{bmatrix} \begin{bmatrix} \dot{\mathbf{u}}(t) \\ \dot{u}_a(t) \end{bmatrix} \\ + \begin{bmatrix} \mathbf{K} & \mathbf{0} \\ G_k \mathbf{w}^T & k_a \end{bmatrix} \begin{bmatrix} \mathbf{u}(t) \\ u_a(t) \end{bmatrix} = \begin{bmatrix} \mathbf{f}(t) \\ 0 \end{bmatrix}, \end{aligned} \quad (5)$$

where  $\mathbf{0}$  is the zero vector. From (5) it is seen that the stiffness matrix is positive definite for any value of  $G_k$ , while for  $g_c > -1$  the damping matrix is positive semi-definite. Thus, for  $g_c > -1$  all the eigenfrequencies will have positive imaginary part, and therefore the system will be stable.

## 2.1. Modal representation of wind turbine structure

An ATMD is usually targeted at one specific mode, which suggests the use of a modal representation for the wind turbine. The displacement of the wind turbine with respect to mode  $j$  is described in terms of the mode-shape vector  $\mathbf{u}_j$  as

$$\mathbf{u}(t) = \mathbf{u}_j r_j(t), \quad (6)$$

where  $r_j$  is the modal coordinate, whereby the modal mass and stiffness associated with mode  $j$  are given by

$$m_j = \mathbf{u}_j^T \mathbf{M} \mathbf{u}_j, \quad k_j = \mathbf{u}_j^T \mathbf{K} \mathbf{u}_j. \quad (7)$$

For convenience the mode shape vector  $\mathbf{u}_j$  is scaled to unity at the location of the damper, so that  $\mathbf{w}^T \mathbf{u}_j = 1$ . Introducing the modal representation (6) with this scaling into (5) the two eoms for the modal coordinate  $r_j$  and the relative displacement  $u_a$  of the ATMD can be written as

$$\begin{aligned} \begin{bmatrix} (1 + \mu_j) & \mu_j \\ 1 & 1 \end{bmatrix} \begin{bmatrix} \ddot{r}_j(t) \\ \ddot{u}_a(t) \end{bmatrix} + \begin{bmatrix} 0 & 0 \\ 0 & (1 + g_c)2\zeta_a \omega_a \end{bmatrix} \begin{bmatrix} \dot{r}_j(t) \\ \dot{u}_a(t) \end{bmatrix} \\ + \begin{bmatrix} \omega_j^2 & 0 \\ g_k \omega_j^2 / \mu_j & \omega_a^2 \end{bmatrix} \begin{bmatrix} r_j(t) \\ u_a(t) \end{bmatrix} = \begin{bmatrix} f_j(t)/m_j \\ 0 \end{bmatrix}, \end{aligned} \quad (8)$$

where  $f_j = \mathbf{u}_j^T \mathbf{f}$  is the modal load. The equations are characterized by the modal mass ratio  $\mu_j$ , the natural frequency  $\omega_j$  associated with mode  $j$ , the frequency  $\omega_a$  of the ATMD, the damping ratio  $\zeta_a$  of the ATMD, the non-dimensional modal feedback gain  $g_k$  associated with the displacement of the tower and the non-dimensional gain parameter  $g_c$ ,

$$\mu_j = \frac{m_a}{m_j}, \quad \omega_j^2 = \frac{k_j}{m_j}, \quad \omega_a^2 = \frac{k_a}{m_a}, \quad 2\zeta_a = \frac{c_a}{\sqrt{m_a k_a}}, \quad g_k = \frac{G_k}{k_j}. \quad (9)$$

Thus, the new displacement gain  $g_k$  is non-dimensional. Assuming harmonic solutions for the equations in (8) on the form

$$r_j = \bar{r}_j \exp i\omega t, \quad u_a = \bar{u}_a \exp i\omega t, \quad f_j = \bar{f}_j \exp i\omega t, \quad (10)$$

with modal amplitude denoted by a bar and  $\omega > 0$  as the forcing frequency, the frequency response of the modal coordinate  $r_j$  is given by

$$\frac{\bar{r}_j}{r_{j,sta}} = \frac{\omega_j^2 [\omega_a^2 - \omega^2 + 2i(1 + g_c)\zeta_a \omega \omega_a]}{\omega^4 - [\omega_j^2(1 - g_k) + \omega_a^2(1 + \mu_j)] \omega^2 + \omega_a^2 \omega_j^2 + 2i(1 + g_c)\zeta_a \omega \omega_a [\omega_j^2 - \omega^2(1 + \mu_j)]}, \quad (11)$$

where  $r_{j,sta} = \bar{f}_j/k_j$  is the static displacement of mode  $j$ . The frequency response of the damper mass is given by

$$\frac{\bar{u}_a}{r_{j,sta}} = \frac{\omega_j^2 [\omega^2 - g_k \omega_j^2 \mu_j^{-1}]}{\omega^4 - [\omega_j^2(1 - g_k) + \omega_a^2(1 + \mu_j)] \omega^2 + \omega_a^2 \omega_j^2 + 2i(1 + g_c)\zeta_a \omega \omega_a [\omega_j^2 - \omega^2(1 + \mu_j)]}. \quad (12)$$

## 2.2. Optimum frequency tuning

The optimum frequency tuning of the ATMD is now determined with respect to mode  $j$ . Figure (2) shows a plot of the dynamic amplification of mode  $j$  as given by (11) for different values of the modified damping ratio  $(1 + g_c)\zeta_a$ . Similar to the passive TMD the ATMD gives rise to two neutral frequencies, denoted as  $\omega_A$  and  $\omega_B$ , which are located on both sides of the structural frequency  $\omega_j$  and at which the magnitude of the frequency response is independent of the damping parameter. The optimum frequency tuning of the ATMD is determined by setting the magnitude at these two neutral frequencies equal to each other, equivalent to the optimum frequency tuning of the passive TMD, credited to Den Hartog [18]. The present deviation follows the given by Krenk [19]. First the neutral frequencies  $\omega_A$  and  $\omega_B$  are determined by setting the magnitude of (11) equal at the limits  $(1 + g_c)\zeta_a = 0$  and  $(1 + g_c)\zeta_a \rightarrow \infty$ , which leads to

$$[\omega_a^2 - \omega^2] [\omega_a \omega (\omega_j^2 - \omega^2(1 + \mu_j))] = \pm \omega_a \omega [\omega^4 - (\omega_j^2(1 - g_k) + \omega_a^2(1 + \mu_j)) \omega^2 + \omega_a^2 \omega_j^2]. \quad (13)$$

Use of the plus sign leads to the roots  $\omega^2 = 0$  and  $\omega^2 = -\omega_j^2 g_k / \mu_j$ , while use of the minus sign gives the following quadratic equation in  $\omega^2$

$$(2 + \mu_j) \frac{\omega^2}{\omega_j^2} \frac{\omega^2}{\omega_a^2} - 2 \left[ \frac{\omega^2}{\omega_a^2} (1 - g_k/2) + \frac{\omega^2}{\omega_j^2} (1 + \mu_j) \right] + 2 = 0. \quad (14)$$

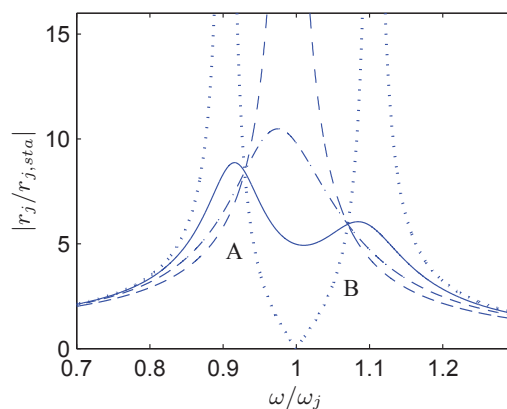


Figure 2. Dynamic amplification for  $\mu = -g_k = 0.02$ ,  $\omega_a = \omega_j$  and  $\zeta_a(1 + g_c) = 0.0$  ( $\cdot \cdot \cdot$ ),  $0.1$  ( $-$ ),  $0.2$  ( $- \cdot -$ ),  $\infty$  ( $\dots$ )

The roots of this equation are  $\omega_A^2$  and  $\omega_B^2$ . The roots are however only needed in the form of their sum, which can be determined by taking minus the coefficient of the linear term, divided by the coefficient of the quadratic term

$$\left(\frac{\omega_A}{\omega_0}\right)^2 + \left(\frac{\omega_B}{\omega_0}\right)^2 = \frac{2}{2 + \mu_j} \left[ (1 - g_k/2) + \frac{\omega^2}{\omega_a^2} (1 + \mu_j) \right]. \quad (15)$$

Next the magnitude at the two frequencies are set equal to each other. Evaluating (11) at the limit  $(1 - g_c)\zeta_a \rightarrow \infty$  gives the magnitude at the neutral frequencies

$$\frac{\bar{r}_j}{\bar{r}_{j,sta}} = \frac{1}{1 - (1 + \mu_j) \frac{\omega^2}{\omega_j^2}}, \quad (16)$$

At the lower frequency  $\omega_A$  the response of mode  $j$  is in phase with the external load, while at the higher frequency  $\omega_B$  the response is in opposite phase. As demonstrated in [19] equal magnitude of the response at the two frequencies results in

$$\left(\frac{\omega_A}{\omega_0}\right)^2 + \left(\frac{\omega_B}{\omega_0}\right)^2 = -\frac{2}{1 + \mu_j}, \quad (17)$$

and combining equation (15) and equation (17) then gives the optimum frequency tuning of the ATMD as

$$\frac{\omega_a}{\omega_0} = \frac{1}{\sqrt{2}} \frac{\sqrt{2 + g_k + g_k \mu}}{1 + \mu_j}. \quad (18)$$

The optimum frequency tuning is seen to depend both on the mass ratio  $\mu_j$  and the gain parameter  $g_k$ . Furthermore,  $g_k = -2/(1 + \mu_j)$  is seen to correspond to a design limit, since it leads to the frequency tuning  $\omega_a = 0$ . For  $g_k \rightarrow 0$  the optimum tuning of the passive TMD is recovered.

Inserting the frequency tuning (18) back into the quadratic equation in (14) provides the roots

$$(1 + \mu) \frac{\omega_{A,B}^2}{\omega_0^2} = 1 \pm \sqrt{\frac{\mu - g_k - g_k \mu}{2 + \mu}}. \quad (19)$$

The dynamic amplification at the two neutral frequencies  $\omega_{A,B}$  is denoted as  $A_{max}$ . It is determined by substituting (19) into (16), which gives

$$A_{max} = \sqrt{\frac{2 + \mu}{\mu - g_k - g_k \mu}}. \quad (20)$$

When comparing this expression for the ATMD to the dynamic amplification for the passive TMD it is seen that the ATMD offers further reduction in the dynamic amplification by an appropriate choice of  $g_k < 0$ , while in the limit  $g_k \rightarrow 0$  the dynamic amplification of the mechanical TMD is recovered. The design limit  $g_k = -2/(1 + \mu_j)$  from (18) is seen to correspond to  $A_{max} = 1$ , i.e. no dynamic amplification.

### 2.3. Optimum damper tuning

With the optimum frequency tuning in (18) the dynamic amplification at the two neutral frequencies is equal, and damping of the ATMD should therefore be scaled, so that a flat plateau between the two neutral frequencies is obtained. In [19] the optimum damper tuning of the passive TMD is determined by selecting a suitable frequency in between the two neutral frequencies and setting the dynamic amplification equal at the three frequencies, whereby a fairly flat plateau is obtained. The same approach is applied in the present case for the ATMD. The dynamic amplification at the frequency  $\omega_\infty = \sqrt{k_j/(m_j + m_a)}$ , which corresponds to the natural frequency of the structure when locking the damper, is thus equated to the dynamic amplification at the two neutral frequencies  $\omega_{A,B}$ . The frequency response at  $\omega_\infty$  follows from (11) as

$$\left[ \frac{\bar{r}_j}{r_{j,sta}} \right]_{\omega_\infty} = \frac{(\mu_j - g_k - g_k \mu_j) - 2i\zeta_a \sqrt{1 + g_k/2 + g_k/2\mu_j} \sqrt{1 + \mu_j}(1 + g_c)}{\mu_j - g_k - g_k \mu_j}, \quad (21)$$

whereby the magnitude is determined as the square root of

$$\left| \frac{\bar{r}_j}{r_{j,sta}} \right|_{\omega_\infty}^2 = \frac{(\mu_j - g_k - g_k \mu_j)^2 + 4\zeta_a^2 (1 + g_k/2 + g_k/2\mu_j)(1 + \mu_j)(1 + g_c)^2}{(\mu_j - g_k - g_k \mu_j)^2}. \quad (22)$$

When equating the dynamic amplification at the three frequencies  $\omega_\infty$  and  $\omega_{A,B}$  the following relation is obtained

$$\frac{2 + \mu}{\mu - g_k - g_k \mu} = \frac{(\mu_j - g_k - g_k \mu_j)^2 + 4\zeta_a^2 (1 + g_k/2 + g_k/2\mu_j)(1 + \mu_j)(1 + g_c)^2}{(\mu_j - g_k - g_k \mu_j)^2}, \quad (23)$$

which determines the optimum damping ratio as

$$(1 + g_c)\zeta_a = \sqrt{\frac{\frac{1}{2} \frac{\mu_j - g_k (1 + \mu_j) (1 + g_k/8 (1 + \mu_j))}{1 + \mu_j + g_k/2(1 + \mu_j)^2}}{2}}. \quad (24)$$

For most feasible designs with  $\mu_j \ll 1$  and  $|g_k| \ll 1$  this expression for the optimum damper tuning can be readily approximated to give

$$(1 + g_c)\zeta_a \simeq \sqrt{\frac{1}{2} \frac{\mu_j - g_k}{1 + \mu_j + g_k/2}}. \quad (25)$$

Together with the expression in (18) the expression above in (25) gives the optimum frequency and damper tuning for the ATMD, while for  $g_k = g_c = 0$  the optimum frequency and damper tuning of the passive TMD is recovered [19]. Comparison of the performance of the ATMD with that of the passive TMD in figure (3) shows that with active control the response of mode  $j$  can be reduced without increasing the damper mass, while the maximum damper mass amplification is increased only slightly. The displacement is however increased significantly for frequencies below the structural frequency. Thus, the ATMD can provide further amplitude reduction compared to the passive TMD, at the expense of a larger damper mass displacement.

#### 2.4. Tuning for reduction of control force

Proper tuning of the gain parameter  $g_c$  is determined by studying the active control force of the ATMD as given by equation (4). The active control force has two terms, the first which is proportional to  $G_k = g_k k_j$ , and the second which is proportional to  $g_c$ . Close to the structural frequency  $\omega_j$  the term proportional to  $g_k$  will be approximately in opposite phase with the second term proportional to  $g_c$ , whereby the two forces partly cancel. By assuming harmonic solutions as in (10) the frequency response of the control force is determined as

$$\left[ \frac{\bar{f}_a}{\bar{f}_j} \right] = - \frac{g_k \omega_j^2 [\omega_a^2 - \omega^2] + 2i\zeta_a \omega_a \omega \omega_j^2 [g_k + g_c \omega_a^2 / \omega_j^2 \mu_j]}{\omega^4 - [\omega_j^2 (1 - g_k) + \omega_a^2 (1 + \mu_j)] \omega^2 + \omega_a^2 \omega_j^2 + 2i\zeta_a \omega \omega_a (1 + g_c) [\omega_j^2 - \omega^2 (1 + \mu_j)]}. \quad (26)$$

When closely studying the frequency response in (26) it is found that by choosing  $g_c$  according to

$$g_c = - \frac{g_k \omega_0^2}{\mu_a \omega^2}, \quad (27)$$

the two terms cancel completely at the frequency  $\omega = \omega_a$ . Figure (4) shows the magnitude of the frequency response of the control force for different values of  $g_c$ . The curve (---) with the tuning according to (27) is seen to have a minimum at the frequency  $\omega_a$ , where the control force is zero. Compared to the case  $g_c = 0$  (—), this gives a significant reduction in the control force around  $\omega_j$ , while for  $\omega \rightarrow 0$  and  $\omega \rightarrow \infty$  the difference for different values for  $g_c$  becomes insignificant. Therefore, the tuning in (27) is in the following chosen as the optimum tuning of  $g_c$ , since it effectively reduces the control effort around the resonance frequency.

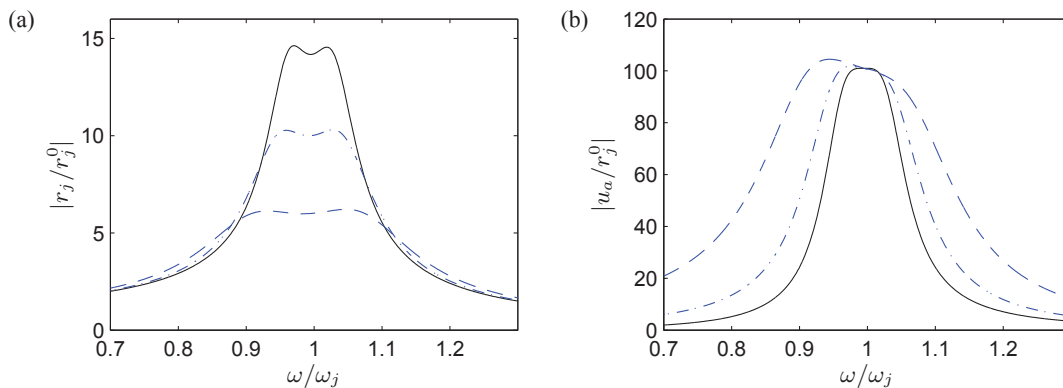


**Figure 3.** Dynamic amplification of mode  $j$  (a) and the damper mass (b) for  $\mu = 0.01$  and  $A_{max} = 14.17$  ( $g_k = 0$ ) (—),  $A_{max} = 10$  (---) and  $A_{max} = 6$  (-·-)

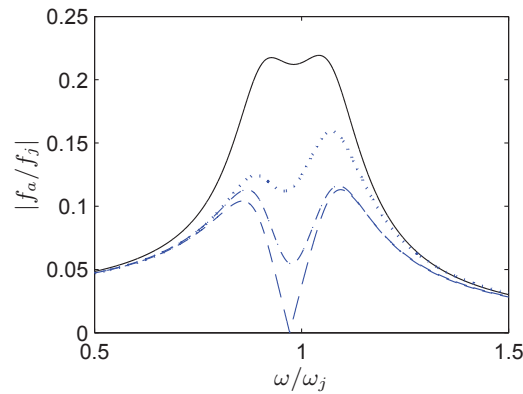


**Figure 4.** Magnitude of the the normalized control force, for  $g_c = 0$  (—),  $g_c = g_c^{opt}/2$  (- · -),  $g_c = g_c^{opt}$  (- -) and  $g_c \rightarrow \infty$  (· · ·), and for  $\mu = 0.02$  and  $A_{max} = 6$ .

**Table I.** Structural properties of the OC3 reference wind turbine

Description	Value
Hub height [m]	90
Tower-top height above MSL [m]	87.6
Tower-base height above MSL [m]	10
Water depth from MSL [m]	20
Penetration depth of monopile [m]	36
Tower mass [ton]	237
Mass of Nacelle+Rotor+Blades [ton]	351
Overall integrated mass [ton]	1216

### 3. DAMPING OF OFFSHORE WIND TURBINE TOWER VIBRATIONS

The performance of the ATMD with respect to damping of offshore wind turbine tower vibrations is now investigated by use of time simulations in HAWC2 [13]. HAWC2 (Horizontal Axis Wind Turbine simulation Code 2nd generation) is an aeroelastic code intended for realistic time simulations of wind turbines developed by DTU Wind Energy, but used both for research projects as well as industrial applications. The code includes a multi body formulation for modeling of nonlinear structural dynamics, a Stig Øye model for aerodynamic modeling of the blades, a hydrodynamic model for modeling of wave loading and added mass, and a nonlinear spring model for modeling of stiffness and damping of the flexible foundation of the soil. The wind turbine model used for the simulations is from the OC3 (Offshore Code Comparison Collaboration) project Phase 2 [20], and the numerical model has been downloaded from [www.hawc2.dk](http://www.hawc2.dk). The wind turbine is a slightly modified version of the 5 MW NREL reference wind turbine [21], which is installed on a monopile with a flexible soil foundation at 20 m of water depth. The tower is approximately 78 m tall and tapered from bottom to top, while the monopile has a constant thickness and diameter. Some of the main structural characteristics of the wind turbine are summarized in table I. In order to reduce vibrations of the two lowest critical tower modes, one ATMD is installed in the rotor direction and one ATMD is installed in the sideways direction. Implementation of the external damper systems into HAWC2 is done using an external dynamic link library (dll), as described in more detail for an advanced dynamic gear model in [22]. The ATMDs are connected to the first node of the tower top at 87.6 m above Mean Sea Level (MSL), where the modal amplitude of the two tower modes is expected to be large.

#### 3.1. Modal properties of critical tower modes

Optimum tuning of the ATMDs according to the expressions in (18), (20), (24) and (27) requires information about the critical modes of the wind turbine, including information about the natural frequency, modal mass and modal stiffness. In order to assess the modal properties, two simple decay analyses are conducted. In the decay analyses the wind turbine without ATMD is assumed at standstill, and the shaft and pitch bearings are fixed. Wind is turned off and the wave height is set to zero, whereby aerodynamic damping is excluded, while the contribution from added mass is included. Instead of

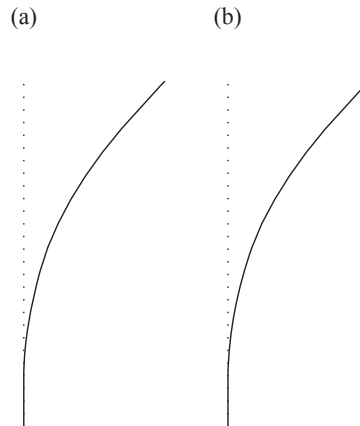


Figure 5. Illustration of the (a) side-side mode and (b) fore-aft mode

the load from wind and waves the turbine is loaded by a single-step load at the top of the tower, and the natural frequency, damping ratio and mode shape is estimated from the free vibrations of the wind turbine. The damping ratio of the two modes is found to be approximately  $\zeta = 0.0020$  with soil damping representing approximately one fifth (0.0004), while the remaining amount (0.0016) comes from proportional damping in the numerical model. In order to increase this to a more realistic value soil damping is simply calibrated to get a total damping ratio in both modes slightly larger than 0.001, which corresponds to experimentally predicted values in the literature [2, 23, 24]. The resulting values for the natural frequencies and damping ratios are presented in table II. The mode shapes of the two tower modes are estimated by taking the fourier transform of the decay signal for each node, and comparing amplitudes of the peaks at the tower frequency. The mode shapes are depicted in figure 5. In order to also estimate the modal mass and stiffness of the two modes, the mass matrix of the wind turbine is reproduced by lumping the mass of each element in the tower and monopile and the mass and inertia of the nacelle, generator, hub and blades. The modal mass is subsequently computed by using the mode shape determined from the decay analysis, and next the modal stiffness is determined from the modal mass and the natural frequency. The estimated values for the modal mass and modal stiffness are also given in table II. As seen from the table the modal properties for the two tower modes are almost the same and it therefore seems reasonable for the two ATMDs acting in the rotor direction and lateral to the rotor direction to be tuned according to the average modal parameters as given in table II. The optimum ATMD parameter values computed from these average modal properties for a mass ratio of  $\mu = 0.01$  are summarized in table III. These ATMD parameter values are used in the simulations in the following sections.

### 3.2. Frequency response

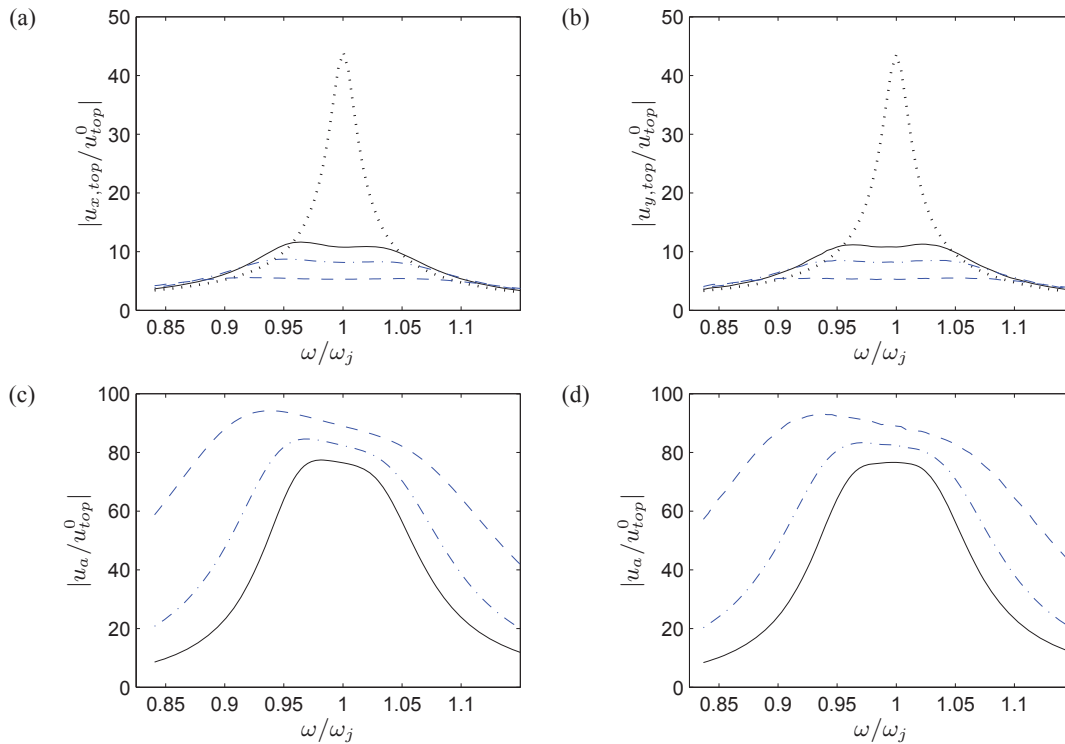
In order to estimate the frequency response of the wind turbine a series of time responses are computed. As for the estimation of the modal properties the wind turbine is again assumed to be at stand still, the wind loading is removed and

Table II. Modal properties of two lowest tower modes

	$\omega_0/(2\pi)$ [Hz]	$\zeta$ [%]	$m_j$ [ton]	$k_j$ [kN/m]
Side-to-side	0.2379	1.14	450	1006
Fore-aft	0.2390	1.15	440	990
Average	0.2385	1.15	445	999

Table III. ATMD properties for  $\mu = 0.01$

$A_{max}$	$\omega_a/(2\pi)$ [Hz]	$\zeta_a(1 + g_c)$ [%]	$m_a$ [kg]	$k_a$ [N/m]	$c_a$ [N-s/m]	$g_k$	$g_c$
14.18	0.2361	7.04	4450	9796	929	0.000	0.00
10	0.2355	9.98	4450	9747	649	-0.010	1.03
6	0.2334	16.75	4450	9572	381	-0.045	4.74



**Figure 6.** Dynamic amplification of tower top for (a) sideways - and (b) rotor direction and of damper for (c) sideways - and (d) rotor direction for  $\mu = 0$  (· · ·) and for  $\mu = 0.01$  and  $A_{max} = 14.17$  ( $g_k = g_c = 0$ ) (—),  $A_{max} = 10$  (---) and  $A_{max} = 6$  (-·-)

the wave height is set to zero. In each time simulation the wind turbine is instead loaded at MSL by a time varying harmonic force, either in the sideways direction or in the direction normal to the rotor plane. The frequency of the harmonic loading is increased slightly for each simulation, and after the initial transient response the corresponding amplitude of the steady state harmonic response is determined. The estimated dynamic amplification for the wind turbine tower top and damper displacement in the two (sideways and rotor) directions are shown in figure 6. As expected the tower top response curves is seen to be almost identical for the two directions. Assuming that the wind turbine is vibrating primarily at resonance in a single vibration mode the dynamic amplification is inversely proportional to the damping ratio via the factor  $1/(2\zeta)$ . In the case without a mass damper the amplitude at resonance is approximately 44.6, which corresponds to a damping ratio of  $\zeta = 0.0115$ , as also estimated by the modal damping ratio determined in Section 3.1. When comparing the response of the full wind turbine with the corresponding frequency response curves for the idealized single degree of freedom (sdf) system in figure 3, the response of the wind turbine top in figure 6 is seen to have a slightly different shape and thereby frequency dependence. This discrepancy is mainly due to the modal approximation of the wind turbine leading to the sdf system and because of the small off-tuning of the damper parameters caused by using the average modal properties for the two tower modes. The amplitude of the response is also seen to be even smaller than predicted for the sdf system. This is due to the inherent damping  $\zeta = 0.0115$  in the wind turbine model, which is not included in the results for the sdf structure. In [19] it has been demonstrated that for the passive TMD the tuning in (18) corresponds to dividing the added damping by the mass damper equally between the two vibration modes associated with the targeted vibration form of the structure. Assuming that the tower top response at the two neutral frequencies is approximately given by amplitude factor  $1/(2\zeta)$  the corresponding damping ratio for the passive case is estimated to be  $\zeta = 0.0467$ , which corresponds well with the sum of half of the added damping 0.0352 from table III and the inherent damping 0.0115. Following the same line of analysis the damping ratio for the case with  $A_{max} = 10$  is estimated to  $\zeta = 0.0613$ , while for  $A_{max} = 6$  the estimation gives  $\zeta = 0.0948$ . This again corresponds well with the inherent damping of 0.0115 plus half of the added damping 0.0499 and 0.0837, respectively. Thus, structural damping and damping from the ATMD appear to be additive during steady-state harmonic motion. Also the relative displacement of the damper mass decreases compared to the sdf case, although this reduction is more pronounced for the passive tuned mass damper than for the ATMD.

### 3.3. Time simulation

As demonstrated in the previous section the ATMD is very effective in reducing the steady state response of the wind turbine around resonance. To investigate the ability of the ATMD to mitigate the transient vibrations following the impact of large waves, the wind turbine with the ATMDs installed is now analyzed through time response simulations. The wind turbine is loaded by a mean wind speed of 8 m/s, with zero turbulence intensity and a constant shear format with parameter value 0.14 according to [13]. The aerodynamic drag on the tower and nacelle is also included. In addition to the wind load the wind turbine is also loaded by a wave train in a direction of  $45^\circ$  relative to the rotor direction. Hereby both the fore-aft mode (rotor direction) and side-side mode (sideways direction) are excited by the misaligned wave loading. The wave train is introduced as three consecutive sine waves at MSL with 10 s wave period. After the wave train has passed the wave loading is set to zero. Furthermore, the wave load is applied sufficiently long time after simulation startup, so that the initial transients from the wind loading can be neglected.

Figure 7 shows the response of the tower top. As expected the vibrations in the rotor direction (fore-aft mode) has a larger decay rate than the vibrations in the sideways direction (side-side mode). This is due to the large additional aerodynamic damping introduced in the rotor direction. The vibrations in the rotor direction also have a non-zero mean, due to the corresponding mean wind pressure, applying a constant load on the wind turbine. The damping in the two directions (modes) is estimated by an exponential fit to the vibration peaks of the free response of the wind turbine. A close-up of the free vibration part of the dynamic response is shown in figure 7(c,d). The solid curves represent the case without mass damper ( $\mu = 0$ ), while the dash-dotted and dashed curves represent the ATMD with  $\mu = 0.01$  and  $A_{max} = 14.17$  (TMD) and 6 (ATMD), respectively. For the case without mass damper (solid curves) the critical damping ratio of the vibrations in the rotor direction (fore-aft) is estimated to  $\zeta_{fa} = 0.1113$ , which is significantly larger compared to standstill because of the aerodynamic damping. By the same procedure the damping ratio of the sideways vibrations (side-side mode) is estimated to  $\zeta_{ss} = 0.0124$ , which is slightly higher than at standstill. This small increase, compared to 0.0115 at standstill, is mainly due to modal interaction between the vibrations in the rotor (fore-aft) and sideways (side-side) and the small aerodynamic damping also present in the sideways direction.

When including a TMD (dash-dotted curves) or an ATMD (dashed curves) it is seen in figure 7(c,d) that the decay rate for the free tower vibrations increases. However, the free vibration decay is no longer described by an exponential function. Instead a clear beating phenomenon is observed, where the amplitude of the regular vibrations are modulated by a slower vibrational behavior. This illustrates the interaction between the structure and mass damper, which obviously complicates the estimation of the damping ratio by an exponential fit procedure. However, by a suitable mean value through the modulating decay the damping ratio for the TMD gives  $\zeta_{ss}^{TMD} = 0.0476$  (sideways direction) and  $\zeta_{fa}^{TMD} = 0.1465$  (rotor direction), while for the ATMD the corresponding damping ratios increase to  $\zeta_{ss}^{ATMD} = 0.0961$  and  $\zeta_{fa}^{ATMD} = 0.1950$ . This again corresponds well with the inherent damping  $\zeta_{ss} = 0.0124$  (sideways direction) and  $\zeta_{fa} = 0.1113$  (rotor direction) plus half the added damping according to table III.

In figure 8 the relative displacement of the damper mass and the force exerted by the damper on the tower are shown for the TMD and ATMD. As expected the vibrations of the ATMD are larger than the vibrations of the passive TMD. However, this is primarily during the initial time period when the three waves are passing. This is caused by the feedback term  $G_{kutt_{top}}$ , proportional to the displacement of the tower top, which is amplifying also vibrations with a frequency below  $\omega_0$ . To avoid this, a high-pass filter should be used to filter the tower displacement signal, before it is fed back to the actuator. Later in the response during the beginning of the free decay, the amplitude of the ATMD response is larger than the TMD response. However, after only a few periods the response of the ATMD is reduced below the response of the TMD, because the vibrations of the tower with the ATMD are damped out. In the plot of the force (c,d) the trend is very similar to the curves for damper mass displacement. During the initial loading period and the initial phase of the free response the force is larger for the ATMD than for the TMD, while after only a few periods of the free response the force exerted by the ATMD is reduced below the force of the TMD.

## 4. CONCLUSION

Dynamic Vibration Absorber concepts traditionally used for damping of tower vibrations in fixed offshore wind turbines is limited in effectiveness by the size of the damper mass. Since additional mass at the top of the tower is highly undesirable, the present paper considers an ATMD format for damping of tower vibrations. Feedback of the tower top displacement and of the relative velocity of the damper mass is introduced to control the active element of the ATMD. By analogy to the optimum tuning of the passive TMD [19], a frequency tuning is introduced for a simple one degree of freedom system that sets the amplitude at the two "neutral frequencies" equal to each other. Furthermore, a damper tuning is introduced that produces a flat response around the tower frequency in the frequency domain, and at the same time minimizes the control effort required to operate the ATMD. The ATMD is found to provide significant decrease in the frequency response amplitude compared to the passive TMD without an increase in damper mass, and the added damping is found to be almost

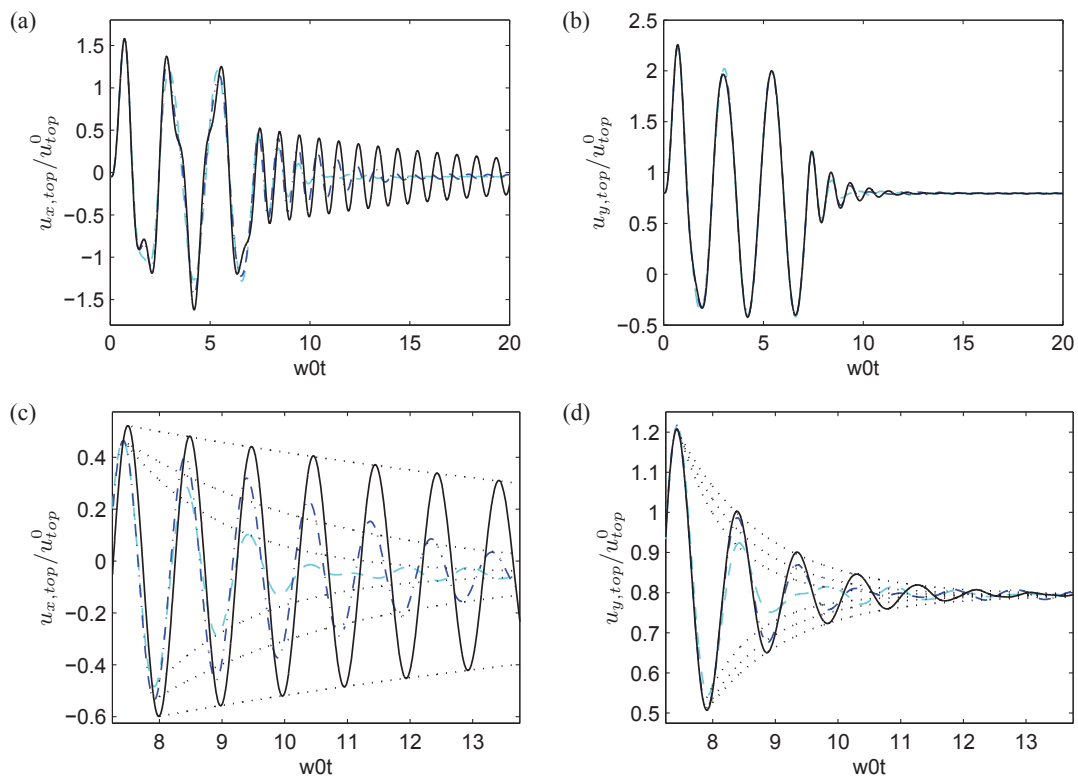


**Figure 7.** Time response of tower top for (a) and (c) sideways - and (b) and (d) rotor direction for  $\mu = 0$  (—) and for  $\mu = 0.01$  and  $A_{max} = 14.17$  ( $g_k = g_c = 0$ ) (-.-) and  $A_{max} = 6$  (- -)

additive to the inherent damping, from structural, soil and aerodynamic damping. A time response analysis demonstrates that also in reducing the transient response is the ATMD superior to the passive TMD, and the damping ratio as predicted by the frequency response analysis seems almost attainable. The reduced mass however comes at the price of increased damper mass displacement, which constitutes a limiting factor for the design of the ATMD. Especially at frequencies below the tower frequency, the vibrations of the damper mass are increased compared to the passive TMD, and this should be compensated for by introducing a high pass filter for filtering away frequencies below the natural frequencies of the two tower modes from the tower top displacement signal, before it is fed back to the actuator of the ATMD.

## ACKNOWLEDGEMENT

This work has been supported by the Danish Energy Agency and Vestas Wind Systems A/S under the EUDP project 'Monopile cost reduction and demonstration by joint applied research'.

## REFERENCES

1. Tarp-Johansen N, Andersen L, Christensen E, Mørch C, Frandsen S, Kallestø B. Comparing sources of damping of cross-wind motion. *Proceedings of the European Wind Energy Conference & Exhibition*, Stockholm, Sweden, 2009.
2. Damgaard M, Ibsen L, Andersen L, Andersen J. Cross-wind modal properties of offshore wind turbines identified by full scale testing. *Journal of Wind Engineering and Industrial Aerodynamics* 2013; **116**:94–108.
3. Tibaldi C, Kim T, Larsen T, Rasmussen F, Rocca Serra Rd, Sanz F. An investigation on wind turbine resonant vibrations. *Wind Energy* 2015; .
4. Association EWE. Report: The european offshore wind industry - key trends and statistics 2013. *Technical Report* 2014. URL [http://www.ewe.org/fileadmin/files/library/publications/statistics/European\\_offshore\\_statistics\\_2013.pdf](http://www.ewe.org/fileadmin/files/library/publications/statistics/European_offshore_statistics_2013.pdf).

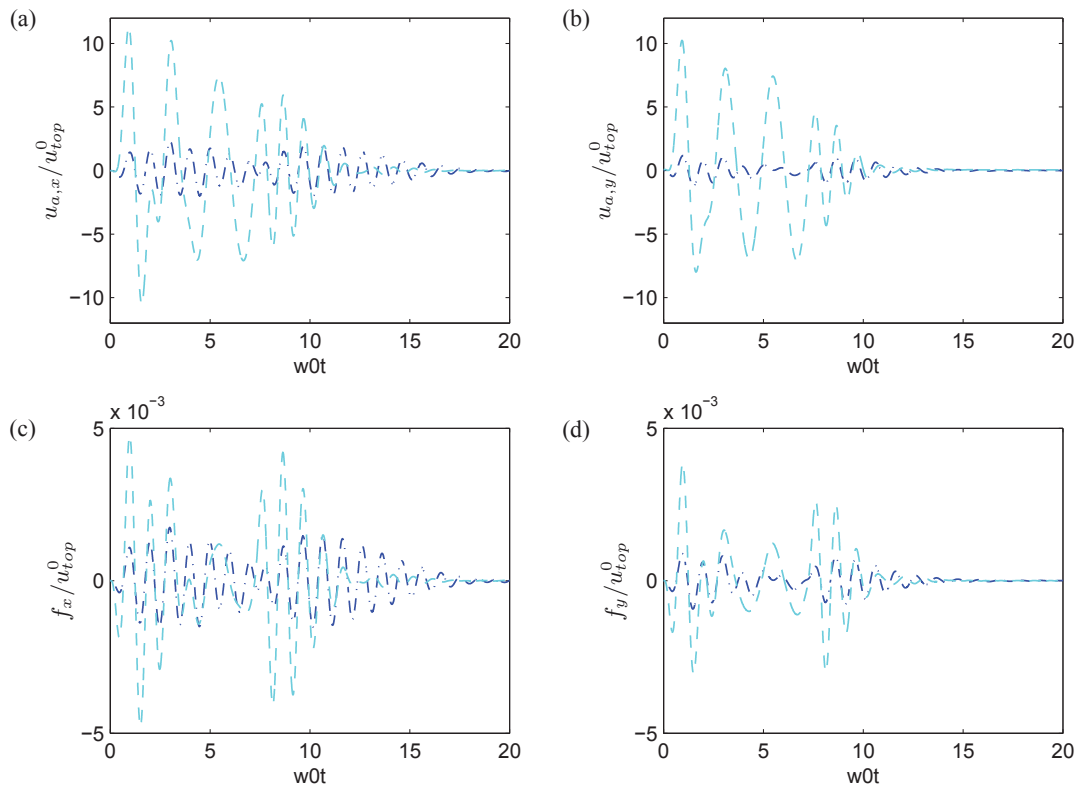


**Figure 8.** Relative displacement of damper mass for (a) sideways damper and (b) rotor direction damper and force exerted by damper for (a) sideways damper and (b) rotor direction damper for  $\mu = 0.01$  and  $A_{max} = 14.17$  ( $g_k = g_c = 0$ ) (---) and  $A_{max} = 6$  (—)

5. Colwell S, Basu B. Tuned liquid column dampers in offshore wind turbines for structural control. *Engineering Structures* 2009; **31**(2):358–368.
6. Stewart GM, Lackner MA. The impact of passive tuned mass dampers and wind–wave misalignment on offshore wind turbine loads. *Engineering Structures* 2014; **73**:54–61.
7. Ricciardelli F, Pizzimenti AD, Mattei M. Passive and active mass damper control of the response of tall buildings to wind gustiness. *Engineering structures* 2003; **25**(9):1199–1209.
8. Ankireddi S, Y Yang HT. Simple atmd control methodology for tall buildings subject to wind loads. *Journal of Structural Engineering* 1996; **122**(1):83–91.
9. Ikeda Y. Active and semi-active vibration control of buildings in japan - practical applications and verification. *Structural Control and Health Monitoring* 2009; **16**(7-8):703–723.
10. Chang JC, Soong TT. Structural control using active tuned mass dampers. *Journal of the Engineering Mechanics Division* 1980; **106**(6):1091–1098.
11. Chang C, Yang HT. Control of buildings using active tuned mass dampers. *Journal of engineering mechanics* 1995; **121**(3):355–366.
12. Nishimura I, Kobori T, Sakamoto M, Koshika N, Sasaki K, Ohru S. Active tuned mass damper. *Smart Materials and Structures* 1992; **1**(4):306.
13. Larsen TJ, Hansen AM. *How 2 HAWC2, the user's manual*. Risø National Laboratory, 2007.
14. Kijewski-Correa T, Kareem A, Kochly M. Experimental verification and full-scale deployment of global positioning systems to monitor the dynamic response of tall buildings. *Journal of Structural Engineering* 2006; **132**(8):1242–1253.
15. Park HS, Sohn HG, Kim IS, Park JH. Application of gps to monitoring of wind-induced responses of high-rise buildings. *Structural Design of Tall and Special Buildings* 2008; **17**(1):117.
16. Boston CH. Mitigation of stay cable vibrations with magnetorheological dampers. PhD Thesis, Diss., Eidgenössische Technische Hochschule ETH Zürich 2010.
17. Bhowmik S. Modelling and control of magnetorheological damper - real-time implementation and experimental verification. PhD Thesis, Technical University of Denmark 2012.

18. Den Hartog J. *Mechanical vibrations* 1956. (Reprinted by Dover, New York, 1985).
19. Krenk S. Frequency analysis of the tuned mass damper. *Journal of applied mechanics* 2005; **72**(6):936–942.
20. Jonkman J, Musial W. Offshore code comparison collaboration (OC3) for IEA task 23 offshore wind technology and deployment. *Technical Report*, National Renewable Energy Laboratory 2010. Technical Report NREL/TP-5000-48191.
21. Jonkman J, Butterfield S, Musial W, Scott G. Definition of a 5-MW reference wind turbine for offshore system development 2009. Technical Report NREL/TP-500-38060.
22. Hansen AM, Larsen TJ. Gear dynamics. *Technical Report*, Risoe National Lab. 2009. Research in Aeroelasticity EFP-2007-II, Risoe-R-1698(EN):134-142.
23. Shirzadeh R, Devriendt C, Bidakhvidi MA, Guillaume P. Experimental and computational damping estimation of an offshore wind turbine on a monopile foundation. *Journal of Wind Engineering and Industrial Aerodynamics* 2013; **120**:96–106.
24. Devriendt C, Jordaens PJ, De Sitter G, Guillaume P. Damping estimation of an offshore wind turbine on a monopile foundation. *IET Renewable Power Generation* 2013; **7**(4):401–412.



# P4

Analysis of hybrid viscous damper by real time hybrid simulations

Mark L. Brodersen, Ge Ou, Jan Høgsberg, Shirley J. Dyke

*Engineering Structures,*  
(submitted)

# Analysis of hybrid viscous damper by real time hybrid simulations

Mark Laier Brodersen<sup>a,b,\*</sup>, Ge Ou<sup>c</sup>, Jan Høgsberg<sup>a</sup>, Shirley Dyke<sup>d</sup>

<sup>a</sup>*Department of Mechanical Engineering, Technical University of Denmark, DK-2800  
Kgs. Lyngby, Denmark*

<sup>b</sup>*National Oilwell Varco Denmark I/S, Priorparken 480, DK-2605 Brøndby, Denmark*

<sup>c</sup>*Lyles School of Civil Engineering, Purdue University, West Lafayette, IN 47906*

<sup>d</sup>*School of Mechanical Engineering, Purdue University, West Lafayette, IN 47906*

---

## Abstract

The present paper compares results from real time hybrid simulations and numerical simulations for a viscous damper concept, consisting of a viscous dash-pot in series with an actuator and a load cell. To emulate a viscous dash-pot, a semi-active MR damper regulated using a bang-bang controller is used in the experimental setup. The comparison demonstrates that using a filtered Integral Force Feedback controller to control the actuator displacement, the hybrid damper concept can be used to increase damping performance compared to the passive case, while instead using a pure Integral Force Feedback the hybrid damper concept can be utilized to increase damper stroke. The results also demonstrate that the performance of the hybrid damper deteriorates because of the limitations of the bang-bang controller, while the offset of the MR damper force leads to drift in the actuator displacement.

*Keywords:* Hybrid control, real time hybrid simulation, Integral Force Feedback, MR damper, bang-bang controller

---

## 1. Introduction

Passive control systems for structural control will not necessarily be optimal for any type of loading [1], and its damping efficiency will also be fully

---

\*Corresponding author at: National Oilwell Varco Denmark I/S, Priorparken 480, DK-2605 Brøndby, Denmark

*Email address:* [MarkLaier.Brodersen@nov.com](mailto:MarkLaier.Brodersen@nov.com), (Mark Laier Brodersen)

dependent on the relative response of the structure at the position of the damper, thereby limiting the effectiveness of a passive system [2]. Contrary to passive systems, active control systems require an external power source, which makes them more costly to operate and prone to power loss [3]. Furthermore, due to the nature of feedback an active control system can become unstable, which again can lead to a loss of structural integrity in the main structure.

To overcome the drawbacks of passive and active control systems so-called hybrid damper concepts have been proposed, where hybrid implies the combined use of active and passive control systems, in which the properties of the two systems are combined in a favorable way [4]. The hybrid viscous damper concept introduced in [5] is a novel damper concept for active control of large structures. The concept consists of a passive viscous dash-pot in series with an active actuator and a load cell unit for measuring the damper force, and with the actuator motion regulated by a decentralized collocated control algorithm based on feedback from the load cell. When the actuator motion is controlled using a filtered Integral Force Feedback (IFF) scheme as in [5], the hybrid damper introduces a phase lead between damper force and damper velocity, which leads to increased attainable damping. When instead the filter time constant is set to zero, as in [6], a pure IFF scheme is recovered [7]. The hybrid damper then performs like a viscous damper with the force fully in phase with velocity, but also with the ability to increase the amplitude of the displacement over the viscous dash-pot. This stroke amplification property may increase the feasibility of installing the hybrid viscous damper in a flexible structure at a location with inherently small deformations. The numerical simulations conducted in [5, 6] demonstrate the large potential and the performance of the hybrid damper concept, which motivates further analysis of the concept. Thus, as the next step the performance of the hybrid damper should be investigated experimentally to prove the concept.

The aim of the present paper is to perform an experimental verification of the performance of the hybrid viscous damper concept. The analysis is performed by comparing numerical results equivalent to the results in [5, 6] with experimental results from real time hybrid simulations (RTHS) performed at the Intelligent Infrastructure Systems Lab at Purdue University. RTHS is a testing technique in which the structural system is divided into an experimental substructure and a numerical substructure, which are tested together as a single system in real time [8, 9]. Since the test is executed in real time it allows for physical testing of the dampers and dissipative devices

in connection with a numerical model of a primary structure.

In this paper an experimental substructure representing a hybrid viscous damper is tested together with a numerical shear frame model in order to validate the results presented in [5], and together with a wind turbine model in order to validate the results presented in [6]. Initially, for completeness the hybrid viscous damper concept is presented in Section 2, which also contains a summary of the two force feedback control strategies. In Section 3 the experimental setup used for the RTHS and the particular partitioning into an experimental substructure and a numerical substructure is explained. The experimental substructure represents a model of the hybrid damper concept, and consist of a magnetorheological (MR) damper in series with a hydraulic actuator and a load cell. An MR damper is used since pure viscous damping by passive means is impossible to achieve in real world applications. The MR damper is controlled by a bang-bang controller to emulate a viscous dash-pot. Furthermore, to avoid instabilities due to the inherent phase lags and time delays in RTHS and the measurement noise, only part of the damper force is measured in the experimental substructure, while the remaining part is represented in the numerical substructure, which also contains the shear frame or wind turbine structure. Numerical results are compared to the results of the RTHS in Section 4, where special attention is paid to the performance of the bang-bang controller and its influence on the resulting damping performance and drift of the actuator displacement. Finally, in Section 5 the results and findings of the present analysis are summarized.

## 2. Hybrid damper concept

The hybrid damper concept is illustrated in figure 1. The hybrid damper consists of a dash-pot with viscous coefficient  $c$  in series with a load cell and an active actuator with controllable piston motion  $q(t)$ . The full displacement across the terminals of the hybrid damper is denoted by  $u(t)$ , whereby the damper force  $f(t)$  is given as

$$f(t) = c(\dot{u}(t) - \dot{q}(t)) \quad (1)$$

The damper force signal  $f(t)$  is measured by the load cell and fed back to control the actuator displacement  $q(t)$  in accordance with a particular control strategy, which consequently governs the overall performance and efficiency of the hybrid viscous damper.

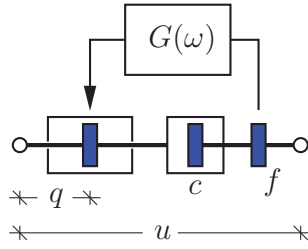


Figure 1: Hybrid viscous damper with integral force feedback.

### 2.1. Filtered integral force feedback

It is demonstrated in [5] that effective structural damping is obtained when the velocity  $\dot{q}(t)$  of the actuator piston motion is controlled by the following filtered Integral Force Feedback (IFF) equation,

$$\tau\ddot{q}(t) + \dot{q}(t) = -gf(t), \quad (2)$$

where  $g$  is the control gain and  $\tau \geq 0$  is the filter time scale. In the case of vanishing control gain ( $g = 0$ ) the pure passive viscous case with  $\dot{q}(t) = 0$  is recovered.

The properties of the hybrid viscous damper are conveniently investigated in the frequency domain, which is obtained by assuming the following complex harmonic solutions

$$u(t) = \bar{u} \exp(i\omega t) \quad , \quad q(t) = \bar{q} \exp(i\omega t) \quad , \quad f(t) = \bar{f} \exp(i\omega t) \quad (3)$$

where  $\omega$  is the angular frequency,  $i = \sqrt{-1}$  is the imaginary unit, while the bar denotes the various harmonic amplitudes. By substitution of (3) the harmonic amplitude of the damper force in (1) can be written as

$$\bar{f} = i\omega c(\bar{u} - \bar{q}) \quad (4)$$

while the feedback equation in (2) is given as

$$(1 + i\omega\tau)i\omega\bar{q} = -g\bar{f} \quad (5)$$

When choosing the piston displacement  $q$  as the control variable of the active actuator the transfer function

$$G(\omega) = \frac{-g}{1 + i\omega(i\omega\tau)} \quad (6)$$

governs the corresponding feedback relation  $\bar{q} = G(\omega)\bar{f}$  shown in figure 1.

Combining (4) and (5) leads to the frequency dependent transfer relation between the damper force and the damper motion,

$$\frac{\bar{f}}{\bar{u}} = i\omega c H(\omega) \quad (7)$$

from where the normalized transfer function  $H(\omega)$  is identified as

$$H(\omega) = \frac{(1 + i\omega\tau)}{1 - \nu + i\omega\tau} \quad , \quad \nu = cg \quad (8)$$

introducing the non-dimensional control gain  $\nu$ . In (7) the frequency dependent function  $H(\omega)$  describes the modification of the damper force transfer relation for the hybrid viscous damper compared to the pure viscous damper associated with  $H(\omega) = 1$ . The real and the imaginary part of  $H(\omega)$  are given as

$$\text{Re}[H(\omega)] = \frac{1 - \nu + (\omega\tau)^2}{(1 - \nu)^2 + (\omega\tau)^2} \quad , \quad \text{Im}[H(\omega)] = \frac{-\nu\omega\tau}{(1 - \nu)^2 + (\omega\tau)^2}, \quad (9)$$

from where it is seen that the condition  $\nu < 1$  ensures energy dissipation defined by  $\text{Im}[\bar{f}/\bar{u}] > 0$ , corresponding to  $\text{Re}[H(\omega)] > 0$ .

## 2.2. Increasing attainable damping

The damper force relation in (7) implies that the amplitude of the transfer function  $|H(\omega)|$  represents the amplification of the damper displacement in the hybrid viscous damper relative to the deformation of the pure viscous damper,

$$\left| \frac{\bar{u} - \bar{q}}{\bar{u}} \right| = |H(\omega)| = \sqrt{\frac{(1 + (\omega\tau)^2)}{(1 - \nu)^2 + (\omega\tau)^2}} \quad (10)$$

Furthermore, the phase angle  $\varphi$  of the transfer function is determined from the relation

$$\tan(\varphi) = \frac{\text{Im}[H(\omega)]}{\text{Re}[H(\omega)]} = \frac{-\nu(\omega\tau)}{1 - \nu + (\omega\tau)^2}, \quad (11)$$

and it describes the phase delay between the damper force  $f$  and the corresponding damper velocity  $\dot{u}$ . Thus,  $\varphi = 0$  represent the passive viscous case without any phase difference.

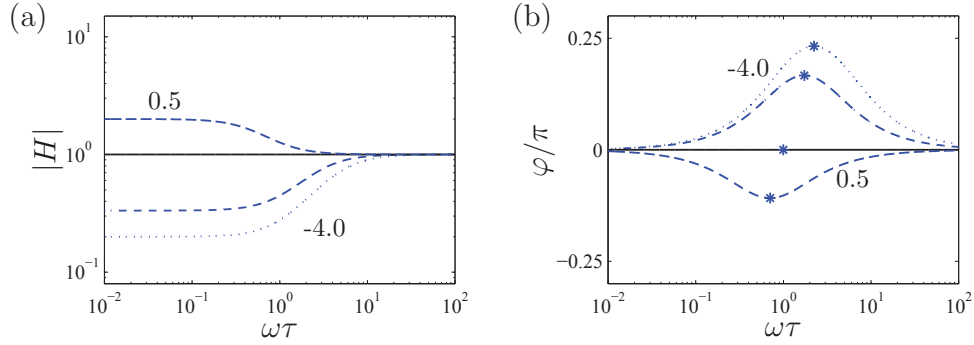


Figure 2: (a) Magnitude and (b) phase of the transfer function  $H(\omega)$  for  $\nu = 0.5$  (---),  $0.0$  (—),  $-2.0$  (-·-·) and  $-4.0$  (· ·).

The amplitude  $|H(\omega)|$  and phase angle  $\varphi$  are plotted in figure 2 for increasing values of the non-dimensional frequency  $\omega\tau$ . The individual curves in the figure represent the various non-dimensional gain values:  $\nu = 0.5$  (---),  $0.0$  (—),  $-2.0$  (-·-·) and  $-4.0$  (· ·). As seen in figure 2a the amplitude decreases for  $\nu < 0$  compared to the passive case with  $\nu = 0$ , while it correspondingly increases in the positive gain interval  $0 < \nu < 1$ . It is seen in figure 2b that the phase angle  $\varphi > 0$  for  $\nu < 0$ , which means that the damper force  $f$  acts ahead of the damper velocity  $\dot{u}$  for negative gain values. Compared to the pure viscous case with  $\nu = 0$ , where the damper force is fully in phase with the damper velocity, this phase lead results in increased attainable damping and thus improved damper performance, [5, 10]. Furthermore, it is found that for  $\nu < 0$  the curves for the phase angle reach a maximum with respect to the non-dimensional frequency  $\omega\tau$ . This maximum is determined by the condition  $d \tan(\varphi)/d(\omega\tau) = 0$ , which leads to

$$\omega\tau = \sqrt{1 - \nu} \quad (12)$$

Thus, to achieve optimal damping of a particular vibration mode of a structure with natural frequency  $\omega_s$  the filter time scale should be chosen as

$$\tau = \frac{\sqrt{1 - \nu}}{\omega_s} \quad (13)$$

Substitution of the expression in (12) into the relation in (11) gives the

corresponding expression for the maximum phase angle

$$\tan(\varphi) = \frac{-\nu}{2\sqrt{1-\nu}} \quad (14)$$

which only depends on  $\nu$  at the targeted natural frequency  $\omega = \omega_s$  of the structure.

For a given gain parameter  $\nu$  the filter time scale  $\tau$  given in (13) will maximize phase lead of the hybrid viscous damper, and therefore maximize the attainable damping for a particular vibration mode with natural frequency  $\omega_s$ . The corresponding maximum phase angle given by (14) is indicated for each of the curves in figure 2b by an asterisk. For  $0 < \nu < 1$  the hybrid viscous damper will instead exhibit a phase lag and the expression in (14) will therefore determine the corresponding minimum of the phase angle.

The integral force feedback equation in (2) governs the velocity  $\dot{q}$  of the actuator piston motion, which implies that the corresponding feedback relation in (6) has a pole at  $s = i\omega = 0$  in the Laplace domain. This pole at the origin may lead to drift in the actuator displacement  $q$  and thereby actuator saturation. To prevent this drift in the actuator motion the original control equation (2) is in the following extended to a full second order differential equation with corner frequency  $\omega_q$ . The final form of the integral force feedback equation is conveniently written in the time domain as

$$\tau\ddot{q}(t) + (1 + \omega_q\tau)\dot{q}(t) + \omega_qq(t) = -gf(t), \quad (15)$$

where the corner frequency  $\omega_q$  should be chosen sufficiently large to prevent drift, without significantly reducing the overall damping performance of the hybrid viscous damper. The influence of  $\omega_q$  with respect to both drift and performance is demonstrated in subsequent sections using real time hybrid simulations.

### 2.3. Increasing damper stroke

The integral force feedback strategy can also be used within the hybrid viscous damper concept to simply amplify the stroke across the viscous damper, see [6]. By setting  $\tau = 0$  in (2) a pure IFF control scheme is recovered, where the actuator displacement  $q(t)$  is governed by the control equation

$$\dot{q}(t) = -gf(t) \quad (16)$$

The frequency domain representation is again obtained by assuming the complex harmonic solutions in (3), whereby the above control relation (16) can be written as

$$i\omega\bar{q} = -g\bar{f} \quad (17)$$

Substitution of this relation into the damper force expression (4) gives the following transfer relation between the damper force and the damper motion,

$$\frac{\bar{f}}{\bar{u}} = i\omega c \frac{1}{1-\nu} = i\omega c H(\omega) \quad (18)$$

Thus, the normalized transfer function  $H(\omega)$  is now given as

$$H(\omega) = \frac{1}{1-\nu} \quad (19)$$

where  $\nu < 1$  again represents the stability condition. It is seen that for  $\nu < 1$  the damper force is fully in phase with velocity and the transfer function  $H(\omega)$  is simply reduced to a real-valued factor, determining the amplification of the damper displacement relative to the passive case with  $\nu = 0$ . As in (10) the amplification of the damper deformation is governed by the amplitude of  $H(\omega)$ , which can be written as

$$\left| \frac{\bar{u} - \bar{q}}{\bar{u}} \right| = \frac{1}{1-\nu} \quad (20)$$

For non-dimensional gain values in the interval  $0 < \nu < 1$  the relative deformation of the viscous dash-pot increases. This demonstrates that the hybrid damper can be used to improve the feasibility of installing viscous dampers at locations in a flexible structure where the deformations are inherently small. As for the filtered IFF scheme in (2) the pure IFF scheme in (16) is prone to drift in the actuator displacement, and a full second order filter with filter frequency  $\omega_f$  and filter time scale  $\tau_f$  has therefore been proposed in [6]. Thus, the modified integral force feedback equation is given as

$$\tau_f \ddot{q}(t) + \dot{q}(t) + \omega_f q(t) = -gf(t), \quad (21)$$

and the corresponding frequency domain representation is obtained by substitution of (3),

$$(\omega_f - \tau_f \omega^2 + i\omega) q = -gf, \quad (22)$$

When combining (22) and (4), the transfer function  $H(\omega)$  associated with the modified control equation (21) becomes

$$H(\omega) = \frac{\omega_f - \tau_f \omega^2 + i\omega}{\omega_f - \tau_f \omega^2 + i\omega(1 - \nu)}, \quad (23)$$

where the magnitude  $|H(\omega)|$  is given as

$$|H(\omega)| = \left| \frac{\bar{u} - \bar{q}}{\bar{u}} \right| = \sqrt{\frac{(\omega_f - \tau_f \omega^2)^2 + \omega^2}{(\omega_f - \tau_f \omega^2)^2 + \omega^2(1 - \nu)^2}} \quad (24)$$

while the phase angle  $\varphi$  is determined from the relation

$$\tan \varphi = \frac{\text{Im}[H(\omega)]}{\text{Re}[H(\omega)]} = \frac{\omega\nu(\omega_f - \tau_f \omega^2)}{\omega^2(1 - \nu) + (\omega_f - \tau_f \omega^2)^2} \quad (25)$$

To maximize the amplification of the damper stroke in (24) the filter frequency should initially be chosen as

$$\omega_f = \tau_f \omega_s^2 \quad (26)$$

where  $\omega_s$  again is the natural frequency of the dominant vibration mode of the flexible structure. Substitution of (26) into both (23) and (25) gives the stroke amplification and phase angle

$$|H(\omega_s)| = \left| \frac{1}{1 - \nu} \right|, \quad \varphi(\omega_s) = 0 \quad (27)$$

at the natural frequency  $\omega = \omega_s$ . Thus, the full filter format in (21) recovers the pure viscous damper with stroke amplification governed by the non-dimensional gain parameter  $\nu$  via the relation in (27a). This demonstrates that by carefully choosing the filter parameters  $\omega_f$  and  $\tau_f$ , the filtered integration format in (21) can be used to reduce drift, without affecting the desired amplification properties of the hybrid viscous damper.

Thus, the performance of the hybrid damper is mainly controlled by the values of the dimensionless gain  $\nu$  and filter time scale  $\tau$ . The difference between the two controllers and the different values for  $\nu$  and  $\tau$  are summarized in table 1.

Table 1: Overview of the two controllers

	$0 < \nu < 1$	$\nu < 0$
$\tau > 0$	FIFF controller with damper force in phase lag	FIFF controller with damper force in phase lead Validation case: 10 story shear frame with top load
$\tau = 0$	IFF controller with hybrid damper stroke amplification Validation case: Offshore wind turbine with wave load	IFF controller with hybrid damper stroke reduction

### 3. Experimental setup

Hybrid simulations constitute a test method that employs the technique of substructuring, in which the entire test structure is divided into two parts: the *experimental substructure* represented by a physical model in the laboratory and the *numerical substructure* represented by a numerical or mathematical model. This division implies that the physical tests conducted on the experimental substructure can be limited to the most critical structural components, which are typically of reduced size and with undefined structural properties.

A (quasi-static) hybrid simulation is performed by initially computing the displacement increment of the numerical substructure based on a suitable load increment. This computed displacement increment from the numerical substructure is then subsequently imposed on the experimental substructure by means of actuators at the interface between the two substructures. In the experimental substructure imposing this displacement generates restoring forces at the interface, which are measured by load cells and used to update the state of the numerical substructure. This sequence of steps is continued in an iterative procedure until the two substructures are in equilibrium with each other, whereafter the system is ready to be advanced by a new load increment.

In real time hybrid simulation (RTHS) the quasi-static process described above is simply conducted in real time, thereby allowing for physical testing of rate dependent components of a structure, such as a damper (the exper-

imental substructure) attached to a large primary structure (the numerical substructure) as described in [11, 12]. In the present investigation RTHS is applied for the analysis of a model of the hybrid viscous damper attached to two types of structures: A 10 story shear frame structure and an offshore wind turbine structure. Hereby, the present results obtained by RTHS are comparable to the numerical results previously obtained in [5] for the shear frame and in [6] for the offshore wind turbine. The hybrid damper model, consisting of a magnetorheological (MR) damper in series with an actuator and a load cell, is considered as the experimental substructure, while the primary structure (shear frame or wind turbine) is represented by the numerical substructure. An overview of the two different experimental setups is provided in table 2.

Table 2: Overview of the two experimental setups

	FIFF	IFF
$\nu$	0, -2, -4	0.5 , 0.75
$\tau$	$(\sqrt{1-\nu})/\omega_1$	0
$\omega_q$	$\omega_1/5, \omega_1/8, \omega_1/20$	Not applicable
$\omega_f = \tau_f \omega_1^2$	Not applicable	$\omega_1/5, \omega_1/8$
Numerical substructure	10 story shear frame, 50 % viscous damper force	Offshore wind turbine, 90 % viscous damper force
Experimental substructure	50 % viscous damper force emulated with MR damper, FIFF controller	10 % viscous damper force emulated with MR damper, IFF controller

### 3.1. Numerical substructure

The structure to be controlled is represented by a finite element (fe) model with mass matrix  $\mathbf{M}$  and stiffness matrix  $\mathbf{K}$ , whereby the equation of motion can be written as

$$\mathbf{M}\ddot{\mathbf{u}}(t) + \mathbf{K}\mathbf{u}(t) = \mathbf{f}(t) - \mathbf{w}f(t) \quad (28)$$

This system of equations is solved with respect to the displacement of the structural degrees of freedom contained in the vector  $\mathbf{u}$ . The matrices  $\mathbf{M}$  and

$\mathbf{K}$  are in the present two cases derived from both a numerical shear frame model and a realistic offshore wind turbine model. The time dependent vector  $\mathbf{f}(t)$  represents the external loading,  $\mathbf{w}$  is the connectivity vector defining the connection of the hybrid viscous damper to the structure, while  $f(t)$  is the force of the hybrid viscous damper. Structural damping is omitted in the numerical model in (28), whereby the resulting damping of the full combined model is entirely due to the performance of the hybrid viscous damper.

### 3.1.1. Damper force partitioning

To avoid instabilities in the RTHS, due to limiting factors as the sampling rate and the inherent phase lags and time delays, the total damper force  $f(t)$  is partitioned into two parts: the force  $f_e(t)$  from the actual hybrid damper representing the *experimental substructure* and  $f_n(t)$  from a numerical hybrid viscous damper model contained in the *numerical substructure*. Thus, the resulting damper force is given by the sum

$$f(t) = f_e(t) + f_n(t) \quad (29)$$

The ratio between the damper force from the experimental substructure and the damper force from the numerical substructure is regulated by an interpolation parameter  $\eta$ , which simply determines the ratio between the viscous parameter  $c_e$  realized by the controllable MR damper in the *experimental substructure* and the remaining viscous parameter  $c_n$  in the *numerical substructure*. Thus, the split in (29) of the total damper force can instead be represented by the following split of the *total* viscous damping parameter  $c_{tot}$ ,

$$c_e = \eta c_{tot} \quad , \quad c_n = (1 - \eta) c_{tot} \quad (30)$$

By changing the value of  $\eta$  between 0 and 1 the ratio between the damper force in the numerical and experimental substructures shifts between the case where the entire damper force is computed numerically ( $\eta = 0$ ) and the situation where the damper force is fully represented in the experimental substructure ( $\eta = 1$ ).

### 3.1.2. Shear frame model

The shear frame model is in the following used for analysis of the filtered IFF scheme described in Section 2.2 and the model is therefore chosen identical to the numerical shear frame model used in the background paper [5]. The model consist of ten stories with the damper connected between the first

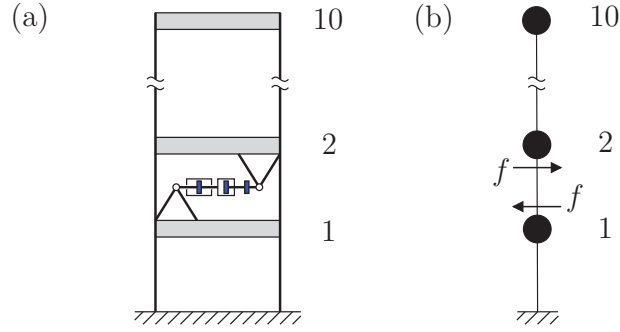


Figure 3: Diagram of (a) the Shear frame with hybrid damper and (b) corresponding FE model with damper force  $f$

and second floor, as illustrated in figure 3(a). The shear frame is modeled by a simple 10 dof FE model with lumped masses, as illustrated in figure 3(b). Hereby, the mass matrix and the stiffness matrix are given as

$$\mathbf{M} = m \begin{bmatrix} 1 & & & & \\ & 1 & & & \\ & & \ddots & & \\ & & & \ddots & \\ & & & & 1 \end{bmatrix}, \quad \mathbf{K} = k \begin{bmatrix} 2 & -1 & & & \\ -1 & 2 & & & \\ & & \ddots & & -1 \\ & & & \ddots & \\ & & & -1 & 1 \end{bmatrix} \quad (31)$$

where the lumped mass  $m$  represents the concentrated floor mass, while  $k$  represents the resulting stiffness of the connecting walls. The model used in the RTHS is assumed to have mass  $m = 1$  kg and stiffness  $k = 1.77$  N/m, which gives a lowest eigenfrequency of  $\omega_1/2\pi = 1$  Hz. The connectivity vector, which describes the connection of the hybrid viscous damper between the first and second floor, is given as

$$\mathbf{w} = [-1, 1, 0, 0, 0, 0, 0, 0, 0, 0]^T$$

Because the hybrid viscous damper is a collocated damping device the deformation of the hybrid viscous damper is consequently given as  $u(t) = \mathbf{w}^T \mathbf{u}(t)$ . When inserting the damper force expression in (29) and the feedback relation in (15) into the structural equation of motion in (28) the governing closed-loop equations for the structural degrees of freedom  $\mathbf{u}(t)$  and the numerical

actuator displacement  $q(t)$  is given as

$$\begin{aligned} \begin{bmatrix} \mathbf{M} & \mathbf{0} \\ \mathbf{0}^T & \tau \end{bmatrix} \begin{bmatrix} \ddot{\mathbf{u}}(t) \\ \ddot{q}(t) \end{bmatrix} + \begin{bmatrix} c_n \mathbf{w} \mathbf{w}^T & -c_n \mathbf{w} \\ \nu \mathbf{w}^T & 1 - \nu + \omega_q \tau \end{bmatrix} \begin{bmatrix} \dot{\mathbf{u}}(t) \\ \dot{q}(t) \end{bmatrix} \\ + \begin{bmatrix} \mathbf{K} & \mathbf{0} \\ \mathbf{0}^T & \omega_q \end{bmatrix} \begin{bmatrix} \mathbf{u}(t) \\ q(t) \end{bmatrix} = \begin{bmatrix} \mathbf{f}(t) - \mathbf{w} f_e^m \\ 0 \end{bmatrix} \end{aligned} \quad (32)$$

The optimum viscous damping parameter is determined for the first vibration mode of the structure by a root locus analysis [5], and the subsequent split of the optimal viscous parameter into an experimental parameter  $c_e$  and a numerical parameter  $c_n$  is then determined by (30) for a given interpolation parameter  $\eta$ . In (32) the superscript  $m$  indicates that  $f_e^m$  represents the damper force actually measured by the load cell, as discussed in further detail in Section 3.2

The shear frame model is assumed to be loaded locally at the top floor in the numerical substructure by a linearly increasing force, which is then removed after time  $t = 2T_1$ , where  $T_1 = 2\pi/\omega_1$  is the vibration period of the first mode shape of the structure. The external load vector  $\mathbf{f}(t)$  is therefore given as

$$\mathbf{f}(t) = p(t)[0, 0, \dots, 0, 1]^T \quad (33)$$

where the load intensity  $p(t)$  is described as

$$\frac{p(t)}{p_0} = \begin{cases} t/(2T_1) & , \quad t \leq 2 T_1 \\ 0 & , \quad t > 2 T_1 \end{cases} \quad (34)$$

with  $p_0$  representing the maximum value of the load intensity.

### 3.1.3. Wind turbine model

The stroke amplifying IFF control scheme described in Section 2.3 is used to impose pure viscous damping with an amplified deformation of the viscous damper. In [6] the hybrid viscous damper with the stroke amplifying IFF control is proposed for damping of offshore wind turbines, and the wind turbine model in the Offshore Code Comparison Collaboration (OC3) [13] is therefore also considered in the present paper. The wind turbine illustrated in figure 4(a) has a tower approximately 78 m tall, which is positioned on a monopile at 10 m above Mean Sea Level (MSL) located at 20 m water depth. The nacelle of the turbine is positioned at the top of the tower and

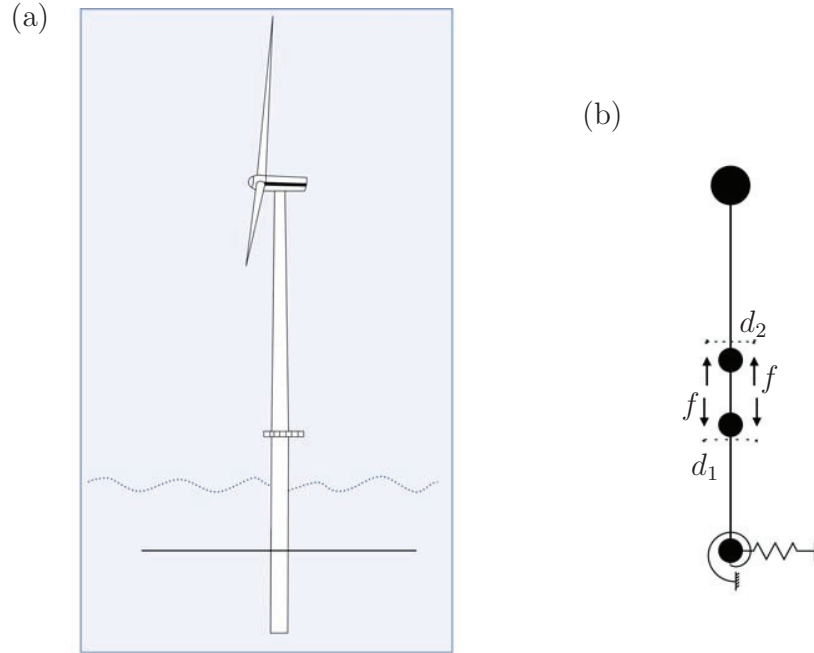


Figure 4: Diagram of (a) the Wind turbine with hybrid damper and (b) corresponding fe model with damper force  $f$

connected to the blades through the hub. The wind turbine is assumed to standstill, whereby the mass of the nacelle, the hub and the blades can be lumped at the top of the tower, and the combined mass is assumed to be 350 ton. The wind turbine structure is modeled by beam elements. Because only planar vibrations in the side-side direction of the turbine are considered the transverse displacement and the associated cross section rotation represent the two nodal degrees of freedom. Thus, the numerical model in the present RTHS study only contains 8 degrees of freedom, as illustrated in figure 4(b). This is significantly less than in the original numerical model of the OC3 reference wind turbine in [6]. However, the dominant dynamics are captured with this model, and the reduced size of the numerical model in the present study is required to limit the computation time during each time step in the RTHS to within a feasible level. The stiffness matrix  $\mathbf{K}$  of the wind turbine model is derived from a complementary energy approach, which allows for shear flexibility and varying cross section properties of the

wind turbine tower. Furthermore, the flexible foundation of the soil is modeled by a coupled spring foundation model with both lateral and rotational springs at the seabed, which are tuned so that the natural frequency of the first tower mode corresponds to the value used in the reference OC3 study [13]. The mass matrix  $\mathbf{M}$  is established by simply lumping the mass of each element and similarly lumping the mass and inertia of the nacelle, rotor and blades at the top node of the tower. Finally, the damper is connected to the tower wall at the bottom of the wind turbine tower and to the tower wall four meters above the bottom of the tower. Hereby, the connectivity vector is given as

$$\mathbf{w} = [0, 0, 0, -d_1/2, 0, d_2/2, 0, 0]^T$$

The non-zero values in  $\mathbf{w}$  are located at the rotational degrees of freedom of the two nodes connected by the hybrid viscous damper.

By inserting the expression for the damper force in (29) and the feedback relation in (21) into the equation of motion in (28) the combined closed-loop equation for the structural degrees of freedom  $\mathbf{u}(t)$  and the actuator displacement  $q(t)$  can be written in a form slightly different from that in (32) for the filtered IFF strategy,

$$\begin{aligned} \begin{bmatrix} \mathbf{M} & \mathbf{0} \\ \mathbf{0}^T & \tau_q \end{bmatrix} \begin{bmatrix} \ddot{\mathbf{u}} \\ \ddot{q} \end{bmatrix} + \begin{bmatrix} c_n \mathbf{w} \mathbf{w}^T & -c_n \mathbf{w} \\ \nu \mathbf{w}^T & 1 - \nu \end{bmatrix} \begin{bmatrix} \dot{\mathbf{u}} \\ \dot{q} \end{bmatrix} \\ + \begin{bmatrix} \mathbf{K} & \mathbf{0} \\ \mathbf{0}^T & \omega_q \end{bmatrix} \begin{bmatrix} \mathbf{u} \\ q \end{bmatrix} = \begin{bmatrix} \mathbf{f} - \mathbf{w} f_e^m \\ 0 \end{bmatrix} \end{aligned} \quad (35)$$

As explained in [6] the optimum viscous damping parameter for a given gain level  $\nu$  can be estimated from the expression

$$c_{opt} = \frac{2\Delta\omega_\infty}{\gamma^2}(1 - \nu) \quad (36)$$

In this expression  $\gamma = \sqrt{(\mathbf{w}^T \mathbf{u}_1)^2}$  represents the modal amplitude across the damper, where  $\mathbf{u}_1$  is the undamped mode shape vector scaled to unit modal mass. Furthermore,  $\Delta\omega_\infty = \omega_1 - \omega_{1,\infty}$  is the difference between the undamped natural frequency  $\omega_1$  of the side-side mode without damper and the natural frequency  $\omega_{1,\infty}$  obtained when the damper acts as a rigid link, see [14]. Finally, the viscous parameters  $c_e$  and  $c_n$  are again determined from the interpolation formula (30).

In the present tests the load consist of a wave train of three regular sine waves with wave period  $T_w = 10$  s, whereafter the external loading is removed abruptly. The wave train acts at MSL and the load vector is therefore given as

$$\mathbf{f}(t) = p(t) [0, 0, 1, 0, \dots]^T,$$

where the time dependent load intensity  $p(t)$  is now given as

$$\frac{p(t)}{p_0} = \begin{cases} \sin(2\pi t/T_w) & , t \leq 3T_w \\ 0 & , t > 3T_w \end{cases}, \quad (37)$$

with  $p_0$  representing the amplitude of the sinusoidal load.

### 3.2. Experimental substructure

The experimental substructure consist of a physical model of the hybrid viscous damper. As explained in the introduction the idealized viscous dash-pot is in the experimental substructure replaced by a semi-active MR damper, which is regulated to emulate the velocity proportional damper force of the ideal viscous dash-pot. The MR damper is placed in series with a hydraulic actuator and a load cell, as shown in figure 5. The load cell measures the damper force  $f_e^m(t)$  produced by the MR damper in the experimental substructure, and the interface between the experimental substructure and

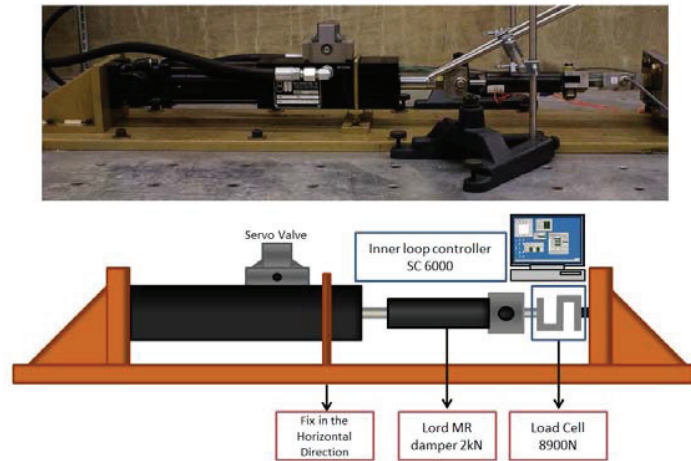


Figure 5: Experimental setup

the numerical substructure is realized by a high performance Speedgoat/xPC real-time kernel.

The actuator is equipped with an internal Linear Variable Differential Transformer (LVDT), which measures the actuator displacement and thereby the deformation of the MR damper. The measured actuator displacement is controlled in an inner loop by a SC6000 controller and in an outer loop by a robust integrated actuator control strategy. The inner loop stabilizes the actuator, while the outer loop guarantees that the desired damper deformation derived from the numerical substructure and the control equation is implemented appropriately, see [15]. Figure 6 shows the MR damper, which is a RD-8041-1 model produced by LORD company, with a specified peak to peak damper force of approximately 2.4 kN when subjected to a velocity of 0.05 m/s at 1 A current input. To reproduce the performance of the hybrid viscous damper the MR damper is controlled using a bang-bang feedback control algorithm. This bang-bang control emulates the behavior of the idealized viscous dash-pot by tracking the desired force  $f_e^d$  of the ideal viscous damper contained in the experimental substructure. The bang-bang controller compares the measured damper force  $f_e^m$  from the load cell with the desired force  $f_e^d$  obtained by the control equation, and determines the command current  $I$  that allows the actual force in the MR damper  $f_e^m$  to track the corresponding desired force  $f_e^d$ . The bang-bang control is an on-off strategy, where maximum current  $I = I_{max}$  is applied when  $f_e^m < f_e^d$ , while  $I = 0$  in the opposite case when  $f_e^m > f_e^d$ . Furthermore, in order to account for the large variation in the desired damper force  $f_e^d$  the force tracking also involves a nonlinear force mapping from the numerical model of the MR damper applied to the experimental substructure. The force measured in the experimental setup is multiplied with an appropriate factor before it is sent to the numerical substructure, and the computed displacement from the numerical substructure is subsequently divided by the same factor before it is sent to the actuator in the experimental setup. Further details on this nonlinear mapping can be found in the accompanying paper [16].

A schematic overview of the RTHS setup is provided in the block diagram in figure 7. The *Finite Element model* in the block diagram represents the governing equations of motion, i.e. (32) for the shear frame structure with the filtered IFF control of the hybrid viscous damper and (35) for the wind turbine model with the pure IFF and stroke amplification. The input to this numerical model is the external load  $\mathbf{f}$  and the measured damper force  $f_e^m$  from the load cell. The output of this block is the computed displace-

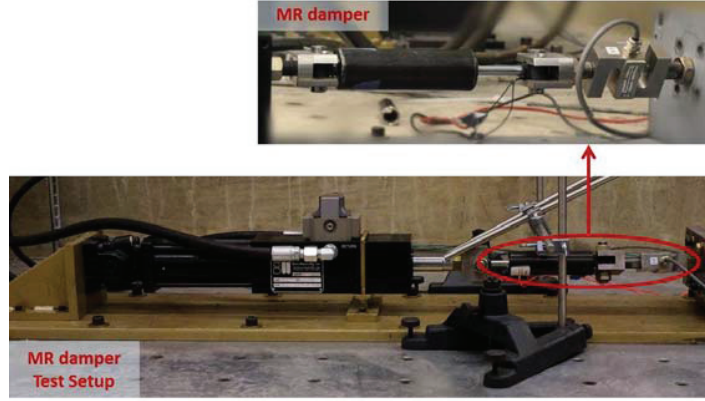


Figure 6: MR damper test setup

ments and velocities, and in particular the deformation of the hybrid viscous damper  $u = \mathbf{w}^T \mathbf{u}$  and its velocity component  $\dot{u} = \mathbf{w}^T \dot{\mathbf{u}}$ . The displacement of the actuator is determined by the *force feedback controller* block, which receives the measured damper force  $f_e^m$  as input. The output of this block is the desired actuator displacement  $q_d$  and its velocity  $\dot{q}_d$ , determined by solving (15) for the shear frame with filtered IFF control and by (21) for the wind turbine with the stroke amplifying IFF. Note that in both (15) and (21) the input is only the experimentally measured damper force  $f_e^m$ , due to the partitioning in (29). The desired viscous damper force  $f_e^d = c_e (\dot{u} - \dot{q}_d)$  is then input to the *Bang-bang controller*, which is used to control the MR damper via the damper current  $I$ . The damper deformation  $u - q_d$  is passed on to the hydraulic actuator. In the present experiment the hydraulic actuator acts both as the active element in the hybrid damper and as interface actuator transferring the displacement of the numerical substructure to the experimental substructure. The displacement of the actuator is therefore given as the combined sum of the command displacement  $-q_d$  from the *force feedback controller* and the hybrid damper displacement  $u = \mathbf{w}^T \mathbf{u}$  computed by the *Finite Element model* in the numerical substructure. The output of the *hybrid damper model* is the damper force in the experimental substructure measured by the load cell.

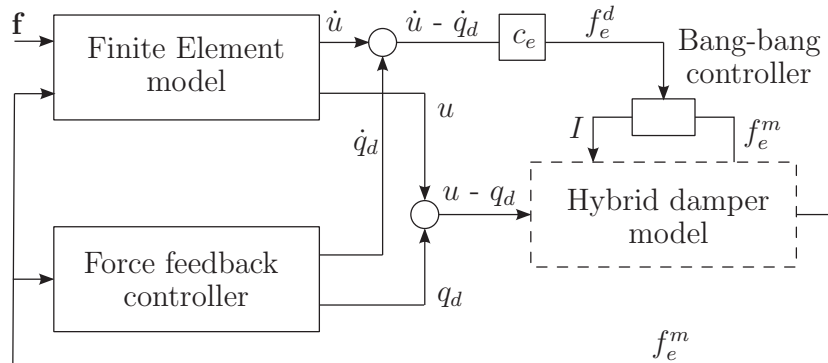


Figure 7: Schematic overview of the RTHS setup in block diagrams

#### 4. Results of Real Time Hybrid Simulations

This section presents results from the Real time hybrid simulations (rths) with the hybrid viscous damper concept using the experimental setup with the bang-bang control of the MR damper described in Section 3.2. The experimental results are compared to the results from the equivalent numerical simulations associated with the interpolation parameter  $\eta = 0$ . Initially, the performance of the hybrid damper with the filtered IFF controller is considered, and subsequently the performance of the pure IFF controller for damper stroke amplification is assessed. Finally, the performance of the bang-bang controller used to track the desired viscous damper force is discussed separately. It should be mentioned that the specific performance of the SC6000 controller is not evaluated, as it is considered as a standard component of the corresponding actuator, while the performance of the Speedgoat/xPC kernel is discussed in the accompanying paper [16].

##### 4.1. Hybrid damper with filtered IFF controller

As explained in Section 3.1.2 the analysis of the filtered IFF controller is conducted for a hybrid viscous damper positioned between the first and second floor in a shear frame structure, which is loaded by the ramp load described in (34). To be able to assess both the performance of the hybrid viscous damper and the influence of the corner frequency  $\omega_q$  in (15) the hybrid simulations are performed with gain values of  $\nu = -2.0$  and  $\nu = -4.0$ , and with corner frequencies  $\omega_q = \omega_1/20$ ,  $\omega_1/8$  and  $\omega_1/5$ . Furthermore, a simulation with  $\nu = 0$  has been conducted in order to specifically address the performance of the bang-bang controller without any influence of the

filtered IFF controller. For all RTHS's an interpolation parameter of  $\eta = 0.5$  in (30) has been used.

#### 4.1.1. Actuator drift and corner frequency

Initially, the performance of the filtered integration in (15) and the corresponding corner frequency  $\omega_q$  is emphasized. Figure 8 compares both the desired damper force  $f_e^d$  (black solid curves) with the measured damper force  $f_e^m$  (blue dots) produced by the MR damper (a,c,e) and the desired damper displacement  $u - q_d$  (blue dots) sent to the *experimental substructure* with the corresponding displacement  $u - q$  (black solid curves) obtained by a direct time integration of the equations of motion in (32) with  $\eta = 0$ , and thereby  $f_e^m = 0$  (b,d,f). The difference between the desired and measured damper force represents the error in the force tracking, while the difference between the damper displacement from RTHS and that from numerical simulations represents the drift of the actuator displacement. The primary goal of this section is to investigate how an error in the force tracking influences the drift in the damper displacement. The results are presented for  $\nu = -2.0$  and with corner frequencies  $\omega_q = \omega_1/20$  (a,b),  $\omega_1/8$  (c,d) and  $\omega_1/5$  (e,f).

It follows from figure 8(a,c,e) that the force tracking is in fact quite accurate, as the measured force  $f_e^m$  (blue dots) in general seems to track the desired force  $f_e^d$  (black solid curves) quite well. However, the force tracking curves show some fluctuations around the local peaks because the bang-bang controller tends to slightly overshoot the desired damper force. Furthermore, a deviation is also observed in figure 8(b,d,f) between the desired displacement over the MR damper  $u - q_d$  (blue dots) and the numerically determined displacement  $u - q$  over the equivalent viscous damper (black solid curves). However, this error appears to be quite smooth because of the filtered integration in the feedback relation (15), which acts as a low pass filter.

The red solid curves in figure 8 represent the relative error in the force tracking  $\varepsilon_f = (f_e^m - f_e^d)/f_{e,max}^d$  (a,c,e) and the corresponding error in the damper displacement  $\varepsilon_{uq} = (u - q_d - (u - q))/(u - q)_{max}$  (b,d,e), with the scaling indicated on the right abscissae. To specifically show the low frequency content, leading to the drift in actuator displacement, both error signals  $\varepsilon_f$  and  $\varepsilon_{uq}$  have been filtered twice by the `Matlab` function `conv` with a rectangular window function of length  $T_1 = 2\pi/\omega_1$ , corresponding to a single vibration period of the first mode shape. Furthermore, to quantify the errors the mean values of both the force error  $\bar{\varepsilon}_f$  and the displacement error  $\bar{\varepsilon}_{uq}$  are given in figure 8 for each simulation.

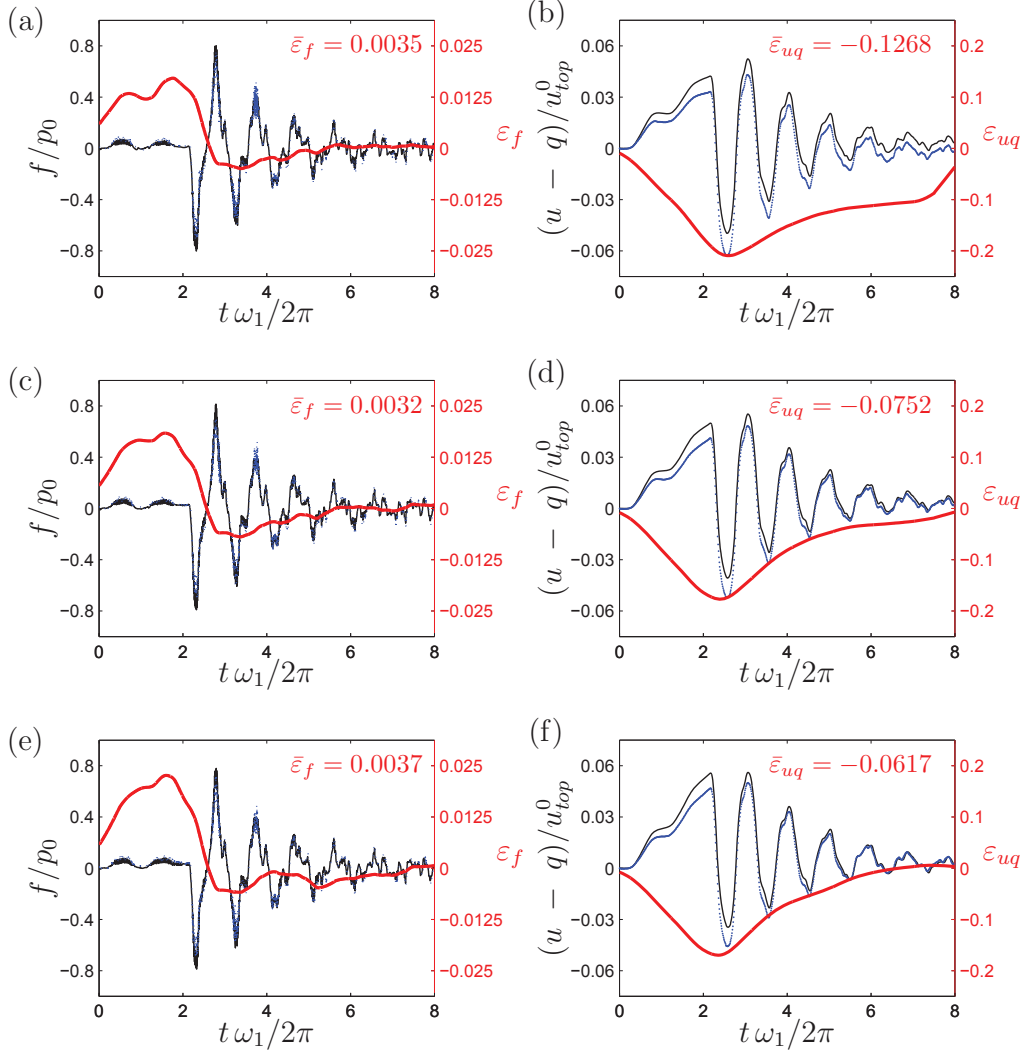


Figure 8: Measured damper force  $f_e^m$  ( $\cdot \cdot$ ) compared with desired damper force  $f_e^d$  ( $-$ ) and desired damper displacement  $u - q_d$  ( $\cdot \cdot$ ) compared with numerical damper displacement ( $-$ ) for filtered IFF controller with  $\nu = -2.0$  and  $\omega_q = \omega_1/20$  (a,b),  $\omega_1/8$  (c,d) and  $\omega_1/5$  (e,f), respectively. Error measure for damper force  $\varepsilon_f$  and damper displacement  $\varepsilon_{uq}$  given by ( $-$ ).

When comparing the two error signals during the first two vibration periods where the load is ramped ( $t < 4\pi/\omega_1$ ) there appears to be a tendency that a positive force error  $\varepsilon_f > 0$  coincides with a negative slope in the displacement error  $d\varepsilon_{uq}/dt < 0$ . After the two initial periods the external load is removed and the error in the damper force in general becomes smaller ( $\varepsilon_f \rightarrow 0$ ), which agrees with the magnitude of the displacement error also becoming smaller ( $\varepsilon_{uq} \rightarrow 0$ ). Furthermore, it is observed that for increasing values of the corner frequency  $\omega_q = \omega_1/20$ (b)  $< \omega_1/8$ (d)  $< \omega_1/5$ (f), the magnitude of the displacement error  $\varepsilon_{uq}$  descends to zero at a faster rate, whereby the accumulated drift in the damper displacement is reduced. Finally, because the three curves for the force error  $\varepsilon_f$  in figure 8(a,c,e) seems to be also identical, the observed reduction in drift of the damper displacement in figure 8(b,d,f) is most likely due to the increase in corner frequency  $\omega_q$ . Thus, it is important to choose  $\omega_q$  sufficiently large to avoid damper drift without deteriorating the performance of the hybrid damper concept.

Figure 9 shows the same results as in figure 8, but now for  $\nu = -4.0$ . Again there is a tendency that a positive force error  $\varepsilon_f$  coincides with a negative slope in  $\varepsilon_{uq}$  and vice versa. Thus, it can again be argued that the error  $\varepsilon_{uq}$  is seemingly proportional to the accumulated error in the damper force  $\varepsilon_f$ . However, the three curves for  $\varepsilon_f$  in figure 9 are in the present case not similar, which means that the corresponding magnitudes of the displacement errors  $\varepsilon_{uq}$  are difficult to compare. Instead the individual mean values in the force signal  $\bar{\varepsilon}_f$  may be compared to the associated mean values  $\bar{\varepsilon}_{uq}$  of the displacement errors. For  $\omega_q = \omega_1/20$  the error ratio is  $|\bar{\varepsilon}_{uq}/\bar{\varepsilon}_f| = |0.0424/0.0004| = 106$ , while for  $\omega_q = \omega_1/8$  it reduces to  $|\bar{\varepsilon}_{uq}/\bar{\varepsilon}_f| = |0.0254/0.0005| = 51$ , while it for the largest corner frequency  $\omega_q = \omega_1/5$  the ratio is further reduced to  $|\bar{\varepsilon}_{uq}/\bar{\varepsilon}_f| = |0.1375/0.0058| = 23$ . Thus, the comparison of the mean error ratios indicates that the drift in the actuator signal is in fact reduced for increasing values of the corner frequency  $\omega_q$ .

#### 4.1.2. Damping performance

Figure 10 shows the displacement response  $u_{top}$  of the shear frame top floor. As for the damper displacement results in figures 8 and 9 the response computed by the RTHS is in the figure compared to the response obtained by a direct time integration of the equations of motion (32) with  $\eta = 0$ . The three pair of curves in figure 10 represent the three non-dimensional gain values  $\nu = 0.0, -2.0$  and  $-4.0$ , while the corner frequency is  $\omega_q = \omega_1/8$  for all curves in figure 10.

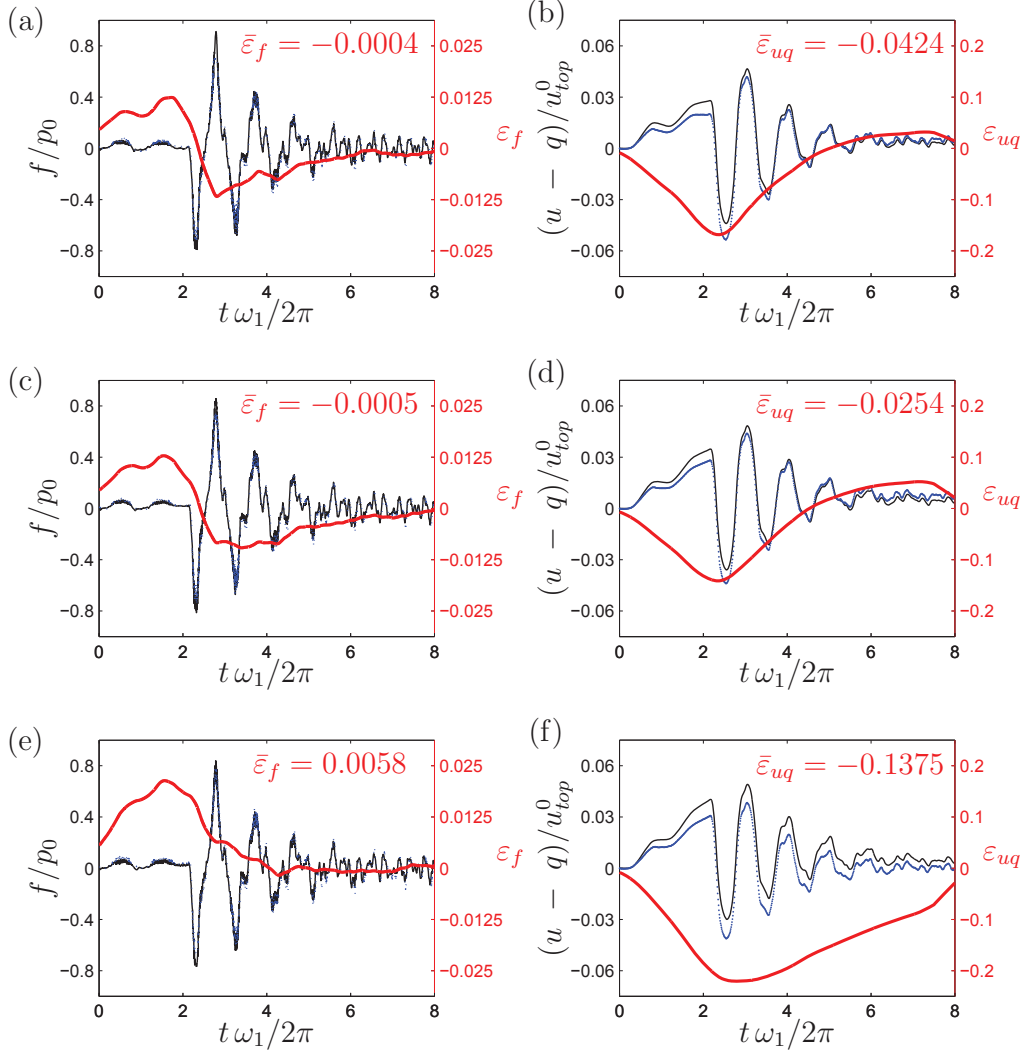


Figure 9: Measured damper force  $f_e^m$  ( $\cdot \cdot$ ) compared with desired damper force  $f_e^d$  ( $-$ ) and desired damper displacement  $u - q_d$  ( $\cdot \cdot$ ) compared with numerical damper displacement ( $-$ ) for filtered IFF controller with  $\nu = -4.0$  and  $\omega_q = \omega_1/20$  (a,b),  $\omega_1/8$  (c,d) and  $\omega_1/5$  (e,f), respectively. Error measure for damper force  $\varepsilon_f$  and damper displacement  $\varepsilon_{uq}$  given by ( $-$ ).

Although there are small discrepancies between the hybrid simulation results and the full numerical results, the agreement between the results is in general very good. As illustrated by the dashed exponential decaying curves the experimental results verify that for  $\nu < 0$  the apparent damping increases when the magnitude of the negative non-dimensional gain increases  $\nu \rightarrow -\infty$ . The damping ratio is estimated by the logarithmic decrement evaluated between both the first and fourth maximum and minimum in the free vibration response. For the direct time integration this procedure gives the average damping ratios  $\zeta = 0.053, 0.086$  and  $0.108$  for  $\nu = 0.0, -2.0$  and  $-4.0$ , respectively. The corresponding damping ratios obtained in [5] by direct time integration with  $\omega_q = 0$  are  $\zeta = 0.053, 0.093$  and  $0.124$ . This shows that the presence of the corner frequency  $\omega_q = \omega_1/8$  slightly reduces the damping performance of the hybrid viscous damper. Specifically, the reduction in damping ratio due to the presence of the corner frequency in the filter equation is 8% for  $\nu = -2.0$ , while it is 13% for the larger gain  $\nu = -4.0$ . This shows that the deterioration in damping performance due to a non-vanishing  $\omega_q$  becomes more pronounced for increasing magnitude of negative  $\nu$ .

For the response obtained by the RTHS the damping ratios are estimated by the logarithmic decrement procedure to be  $\zeta = 0.051, 0.082$  and  $0.106$ , which are slightly smaller than the damping ratios obtained by the direct time integration. Specifically, the reduction in damping ratio compared to the results obtained by the pure time integration is approximately 4% for  $\nu = 0.0$ , 5% for  $\nu = -2.0$  and 2% for the largest negative gain value  $\nu = -4.0$ . Thus,

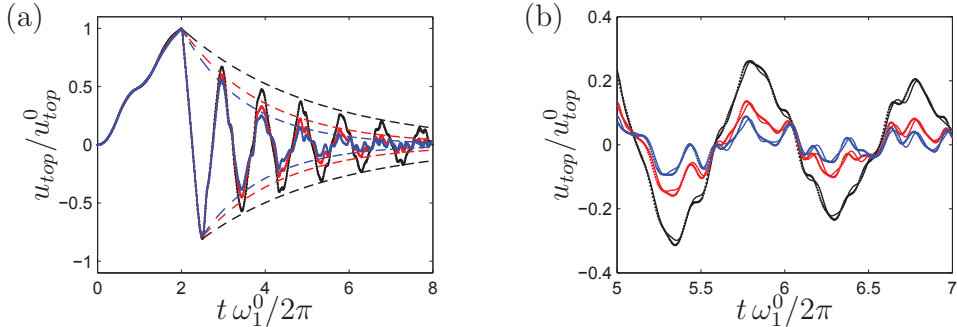


Figure 10: Top-floor response by numerical simulation for  $\nu = 0.0$  (—),  $-2$  (—) and  $-4$  (—) and by RTHS for  $\nu = 0.0$  (· ·),  $-2$  (· ·) and  $-4$  (· ·) and with  $\omega_q = \omega_1/8$

the deviations between the curves in figure 10, representing the RTHS and the direct time integration, are apparently independent of the magnitude of the gain value  $\nu$  and may instead be attributed to the performance of the bang-bang controller. The rather small deviations between the results obtained by the direct time integration and by the hybrid simulation show that the performance of the hybrid viscous damper is quite robust with respect to errors in the force tracking. It should be noted that the interpolation factor  $\eta = 0.5$ , whereby half the damper force is computed in the experimental substructure. Even though half of the damper force is represented in the RTHS, the experimental results still match the numerical results.

#### 4.2. Hybrid damper with stroke amplifying IFF controller

This section investigates the hybrid viscous damper with stroke amplifying IFF control, as presented in Section 2.3. The hybrid damper is installed at the bottom of the tower of an offshore wind turbine model and loaded by three sinusoidal waves, as explained in Section 3.1.3. The control gain values in the RTHS are chosen as  $\nu = 0.5$  or  $\nu = 0.75$ , while the filter frequencies of the control equation in (21) are either  $\omega_f = \tau_f \omega_1^2 = \omega_1/8$  or  $\omega_1/5$ . These parameter combinations assess both the performance of the hybrid viscous damper and the filtered integration with  $\omega_f = \tau_f \omega_1^2 > 0$ . An interpolation parameter of  $\eta = 0.1$  has been used in all the hybrid simulations associated with the stroke amplifying IFF control.

##### 4.2.1. Actuator drift and filter parameters

The performance of the filtered version of the pure IFF control in (21) is investigated by comparing the measured damper force  $f_e^m$  of the MR damper with the desired damper force  $f_e^d$ , and furthermore by comparing the desired damper displacement  $(u - q_d)$  sent to the experimental substructure with the corresponding displacement  $(u - q)$  obtained by direct time integration of (35) with  $\eta = 0$ . The results of the simulations are presented for  $\nu = 0.5$  in figure 11 and for  $\nu = 0.75$  in figure 12. The curves in figure 11(a,b) are obtained with filter frequency  $\omega_f = \tau_f \omega_1^2 = \omega_1/8$ , while in (c,d) the frequency is  $\omega_f = \tau_f \omega_1^2 = \omega_1/5$ . The small deviation between the desired and measured damper force, which mainly occur around the maxima and minima, is again attributed to the limited force tracking capabilities of the bang-bang control. The associated difference in damper displacement is seen to be somewhat larger than for the force tracking error, but with less irregularities. The latter can be ascribed to the integration in (21), which acts as a low pass

filter. The error in damper displacement represents the actuator drift in the hybrid viscous damper, which may cause actuator saturation if it becomes too large. When comparing the desired damper displacement  $(u - q_d)$  for  $\nu = 0.5$  in figure 11 and for  $\nu = 0.75$  in figure 12 it is found that the damper amplitude is approximately doubled, which agrees with the theoretical result in (27).

The red solid curves in figures 11 and 12 show the relative force tracking error  $\varepsilon_f = (f_e^m - f_e^d)/f_{e,max}^d$  and the relative error in the damper displacement  $\varepsilon_{uq} = ((u - q_d) - (u - q))/((u - q)max)$ , with the scaling shown on the right abscissae. The comparison of the mean force tracking errors  $\bar{\varepsilon}_f$  and  $\bar{\varepsilon}_{uq}$  gives an indication of the influence of the choice of filter frequency  $\omega_f$ . For  $\nu = 0.5$  the error ratios are  $\bar{\varepsilon}_{uq}/\bar{\varepsilon}_f \simeq 5$  and 2.7 for  $\omega_f = \tau_f \omega_1^2 = \omega_1/8$  and

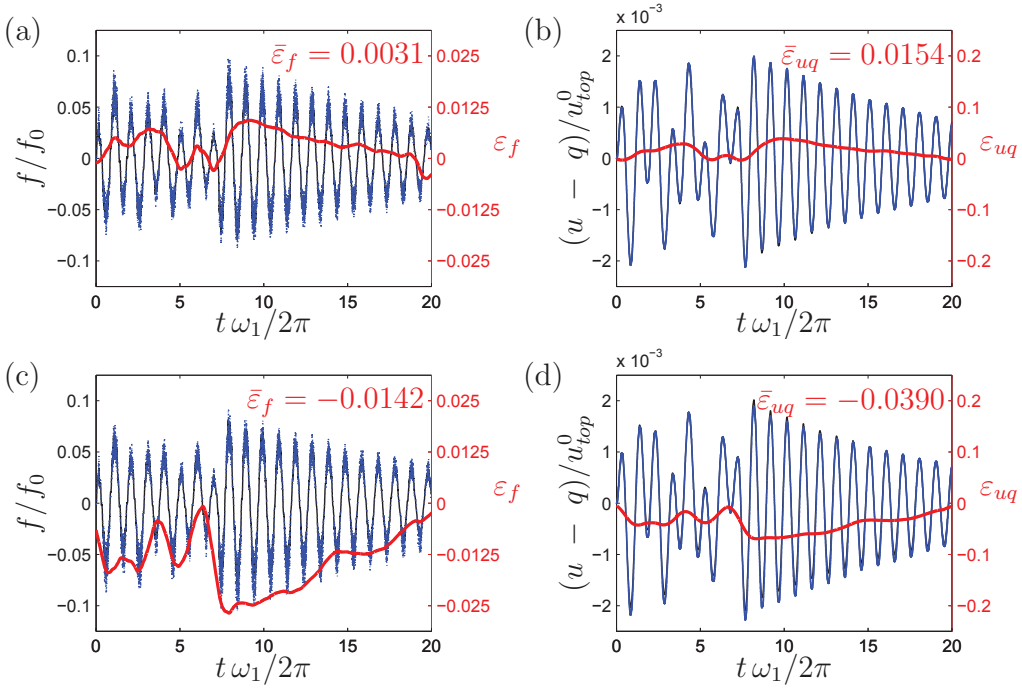


Figure 11: Measured damper force  $f_e^m$  ( $\cdot \cdot$ ) compared with desired damper force  $f_e^d$  ( $-$ ) and desired damper displacement  $u - q_d$  ( $\cdot \cdot$ ) compared with numerical damper displacement ( $-$ ) for  $\nu = 0.5$  and  $\omega_f = \tau_f \omega_1^2 = \omega_1/8$  (a)-(b) and  $\omega_1/5$  (c)-(d). Error measure for damper force  $\varepsilon_f$  and damper displacement  $\varepsilon_{uq}$  given by ( $-$ ).

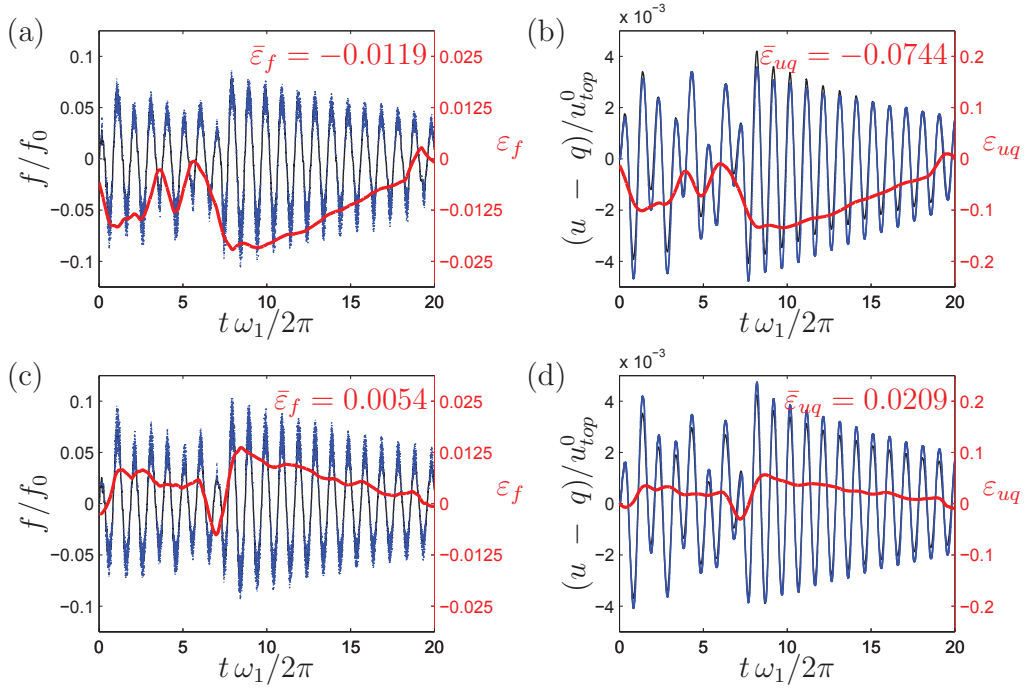


Figure 12: Measured damper force  $f_e^m$  ( $\cdot \cdot$ ) compared with desired damper force  $f_e^d$  ( $-$ ) and desired damper displacement  $u - q_d$  ( $\cdot \cdot$ ) compared with numerical damper displacement ( $-$ ) for  $\nu = 0.75$  and  $\omega_f = \tau_f \omega_1^2 = \omega_1/8$  (a)-(b) and  $\omega_1/5$  (c)-(d). Error measure for damper force  $\varepsilon_f$  and damper displacement  $\varepsilon_{uq}$  given by ( $-$ ).

$\omega_1/5$ , respectively, while for  $\nu = 0.75$  they are  $\bar{\varepsilon}_{uq}/\bar{\varepsilon}_f \simeq 6.3$  and  $3.9$ . The apparent inverse proportionality between the error ratio and the corresponding magnitude of the filter frequency  $\omega_f$  indicates that the drift can be effectively reduced by increasing the value of  $\omega_f = \tau_f \omega_1^2$ , while the drift of the actuator seems to increase with the gain parameter  $\nu$ .

#### 4.2.2. Damping performance

The damping performance of the hybrid damper with the IFF controller is investigated by comparing the hybrid simulation results ( $\cdot \cdot$ ) of the tower top displacement with the corresponding numerical results ( $-$ ). The results are shown in figure 13. The free decay is estimated from the exponentially decaying curves in the figure, which are seen to almost exactly match the cor-

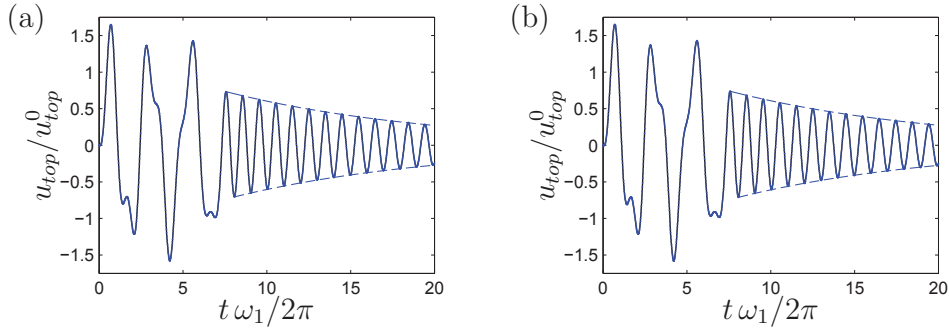


Figure 13: Top tower displacement as computed in the numerical substructure ( $\cdot \cdot$ ), and as computed by a numerical simulation ( $-$ ) for (a)  $\nu = 0.5$  and (b)  $\nu = 0.75$  for  $\omega_f = \tau_f \omega_1^2 = \omega_1/5$

responding decay in vibration amplitude. The results in the figure are shown for gain values (a)  $\nu = 0.5$  and (b)  $\nu = 0.75$ , while the corner frequency of the integration filter in (21) is chosen as  $\omega_f = \tau_f \omega_1^2 = \omega_1/5$ . The experimental and numerical results are seen to match very well, and the damping performance appears to be almost identical for the RTHS and the corresponding numerical simulation. The damping ratio is again estimated by the logarithmic decrement evaluated between the first and fourth maximum and minimum of the free decay. The average damping ratio is  $\zeta = 0.0128$  for the numerical simulation, while  $\zeta = 0.0127$  is obtained from the RTHS results. Thus, the deviation between the two results is less than 1%. The small reduction in damping ratio observed in the RTHS may as before be due to the bang-bang controller and the non-viscous behavior of the MR damper. Since a fairly small interpolation parameter  $\eta = 0.1$  has been used in the present study, the performance of the RTHS may be influenced by the larger experimental substructure in the case of a full scale test with different partitioning in the RTHS.

#### 4.3. Force tracking

As the performance of the hybrid damper in the experimental substructure is found to depend on the performance of the associated Bang-Bang control of the MR damper a specific analysis of the force tracking capabilities are now conducted. The performance of the Bang-Bang controller is illustrated in figure 14, which shows force-velocity curves of the MR damper ( $\cdot \cdot$ ) together with the corresponding desired curves ( $- -$ ) for both the (a)

filtered and (b) pure IFF controller. Furthermore, the figure indicates the idealized linear curve (–) related to a pure viscous dashpot. In general, the MR damper together with the bang-bang control is able to track the desired force response quit well. However, due to the abrupt on/off nature of the bang-bang controller the damper force response inherently introduces a certain amount of high-frequency fluctuations. The IFF controller in figure 14(b) results in a very jagged response, while the filtered IFF controller in figure 14(a) produces a less noisy force-velocity relation. This difference could be due to the controller as well as the difference in the numerical model and loading. The damper force fluctuations lead to discrepancies between the desired force (– –) and the ideal viscous dashpot curve (–), which of course in turn also influences the overall damping performance of the hybrid damper, as already discussed in connection with the free decay curves in figures 10 and 13. As shown in figures 8-9 and 11-12 the force tracking error also contains a low-frequency component, which leads to drift in the actuator displacement. The low-frequency error is caused by a force offset in the MR damper force, most likely due to clamping of the damper. The low-frequency error is amplified by the IFF controller, introducing drift of the actuator displacement, which may result in saturation of the actuator command signal. The non-zero force offset could also be an issue in a real-world implementation of the hybrid damper concept. As also seen in figures 8-9 and 11-12 this undesirable drift is in fact reduced effectively by introduction of a filtered integration with suitably chosen corner frequency  $\omega_q$  or filter parameters  $\omega_f$  and  $\tau_f$ , respectively.

## 5. Discussion and outlook

Overall, the results from the RTHS and the results from the numerical simulations seem to match fairly well. The results from the hybrid simulations with the filtered IFF controller verify that for a negative gain  $\nu < 0$ , damping can be increased compared to the passive viscous case, while the results from the RTHS with the pure IFF controller demonstrate that for  $0 < \nu < 1$  the displacement over the damper is increased. These results validate the numerical results presented in [5] and [6], and show that the hybrid viscous damper concept can be used for damping of flexible structures. Discrepancies between the experimental and numerical results are most pronounced in the results for the displacement over the damper, which are seen to be caused by an error in the damper force tracking capabilities. This

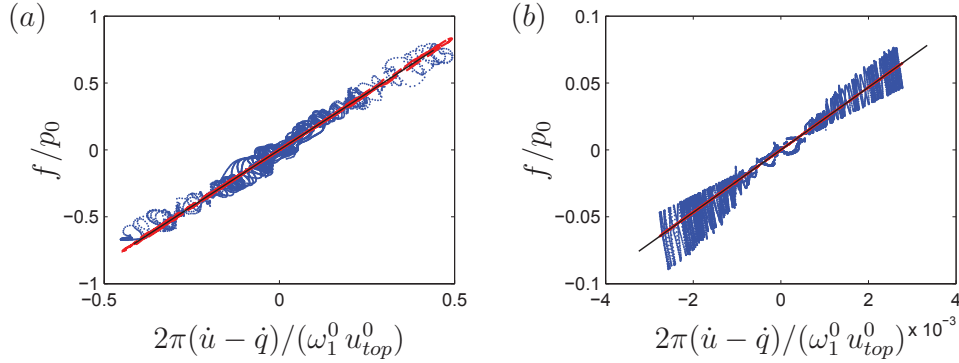


Figure 14: Comparison between typically plots of damper force versus velocity response for the MR damper ( $\cdot \cdot$ ) and the desired damper response ( $- -$ ) together with the linear response of the ideal viscous dash-pot ( $-$ ) for (a) the filtered IFF controller and (b) the IFF controller

tracking error has both a high-frequency part due to the fluctuations in the Bang-Bang controller, and a low-frequency part caused by the force offset in the MR damper. The high-frequency part causes deterioration in the damping efficiency of the hybrid damper. For the hybrid damper with filtered IFF control and  $\eta = 0.5$  the reduction in damping ratio is approximately 4%, while for the hybrid damper with pure IFF control and interpolation parameter  $\eta = 0.1$  the decrease is found to be around 1%.

The present paper provides an initial experimental verification of the realization and performance of the hybrid viscous damper with filtered force feedback. Future work on the analysis of the hybrid viscous damper should focus on increasing the damper force ratio in the experimental substructure of the RTHS to make the simulations more realistic. For the present hybrid damper model the MR damper dictates the stability limit. Applying a more advanced controller for the MR damper would decrease the force tracking error and thereby increase the overall damping performance. Furthermore, the low-frequency part of the tracking error leads to drift of the actuator command signal. This drift could be decreased by applying a MR damper with a different design that does not exhibit an offset in the force.

## Acknowledgments

This work has been supported by the Danish Energy Agency and Vestas Wind Systems A/S under the EUDP project 'Monopile cost reduction and

demonstration by joint applied research’, and the stay abroad at Purdue University has been supported by ”Augustinus Fonden” and the ”Oticon” Foundation. Purdue University co-authors were supported in part by the National Science Foundation grant CCF-1136075. The support is greatly appreciated.

- [1] B. Spencer Jr, S. Nagarajaiah, State of the art of structural control, *Journal of structural engineering* 129 (7) (2003) 845–856.
- [2] T. E. Saeed, G. Nikolakopoulos, J.-E. Jonasson, H. Hedlund, A state-of-the-art review of structural control systems, *Journal of Vibration and Control*.
- [3] G. Housner, L. Bergman, T. Caughey, A. Chassiakos, R. Claus, S. Masri, R. Skelton, T. Soong, B. Spencer, J. Yao, Structural control: Past, present, and future, *Journal of Engineering Mechanics* 123 (9) (1997) 897–971.
- [4] B. Spencer Jr, M. K. Sain, Controlling buildings: a new frontier in feedback, *Control Systems, IEEE* 17 (6) (1997) 19–35.
- [5] J. Høgsberg, M. L. Brodersen, Hybrid viscous damper with filtered integral force feedback control, *Journal of Vibration and Control*, Published online in 2014.
- [6] M. L. Brodersen, J. Høgsberg, Hybrid damper concept for damping of offshore wind turbine tower vibrations through damper stroke amplification, *Wind Energy*.
- [7] A. Preumont, *Vibration control of active structures: an introduction*, Vol. 179, Springer, 2011.
- [8] M. Nakashima, N. Masaoka, Real-time on-line test for mdof systems, *Earthquake engineering & structural dynamics* 28 (4) (1999) 393–420.
- [9] A. Blakeborough, M. Williams, A. Darby, D. Williams, The development of real-time substructure testing, *Philosophical Transactions of the Royal Society of London. Series A: Mathematical, Physical and Engineering Sciences* 359 (1786) (2001) 1869–1891.

- [10] J. Høgsberg, S. Krenk, Linear control strategies for damping of flexible structures, *Journal of Sound and Vibration* 293 (1) (2006) 59–77.
- [11] R. Christenson, Y. Z. Lin, A. Emmons, B. Bass, Large-scale experimental verification of semiactive control through real-time hybrid simulation 1, *Journal of Structural Engineering* 134 (4) (2008) 522–534.
- [12] Y.-J. Cha, J. Zhang, A. K. Agrawal, B. Dong, A. Friedman, S. J. Dyke, J. Ricles, Comparative studies of semiactive control strategies for mr dampers: pure simulation and real-time hybrid tests, *Journal of Structural Engineering* 139 (7) (2013) 1237–1248.
- [13] J. Jonkman, W. Musial, Offshore code comparison collaboration (OC3) for IEA task 23 offshore wind technology and deployment, Tech. rep., National Renewable Energy Laboratory, nREL/TP-500-48191 (2010).
- [14] J. Main, S. Krenk, Efficiency and tuning of viscous dampers on discrete systems, *Journal of Sound and Vibration* 286 (1-2) (2005) 97–122.
- [15] G. Ou, A. I. Ozdagli, S. J. Dyke, B. Wu, Robust integrated actuator control: experimental verification and real-time hybrid-simulation implementation, *Earthquake Engineering & Structural Dynamics* 44 (3) (2015) 441–460.
- [16] G. Ou, M. L. Brodersen, S. Dyke, Real time hybrid simulations case study: Vibration reduction of offshore wind turbine using hybrid controlled damper.





**DTU Mechanical Engineering**  
**Section of Solid Mechanics**  
Technical University of Denmark

Nils Koppels Allé, Bld. 404  
DK-2800 Kgs. Lyngby  
Denmark  
Phone (+45) 4525 4250  
Fax (+45) 4593 1475  
[www.mek.dtu.dk](http://www.mek.dtu.dk)  
ISBN: 978-87-7475-455-8

**DCAMM**  
**Danish Center for Applied Mathematics and Mechanics**

Nils Koppels Allé, Bld. 404  
DK-2800 Kgs. Lyngby  
Denmark  
Phone (+45) 4525 4250  
Fax (+45) 4593 1475  
[www.dcam.dk](http://www.dcam.dk)  
ISSN: 0903-1685